Institut für Informatik
Technische Universität München

Development of a Birth Prediction Model Using Virtual Delivery Simulation

Manuel Schröder

Vollständiger Abdruck der von der Fakultät für Informatik der Technischen Universität München zur Erlangung des akademischen Grades eines

Doktors der Naturwissenschaften (Dr. rer. nat.)

genehmigten Dissertation.

Vorsitzender:	Univ.-Prof. Dr. Dr. h. c. Javier Esparza
Prüfer der Dissertation:	1. Univ.-Prof. Dr. Rüdiger Westermann
	2. Priv.-Doz. Dr. Rainer H. H. Burgkart

Die Dissertation wurde am 08.10.2015 bei der Technischen Universität München eingereicht und durch die Fakultät für Informatik am 21.11.2015 angenommen.

Abstract

In this thesis, I will present a novel, sophisticated birth simulation which is based on a large set of clinical data and which shows how this clinical data can be processed in an efficient and effective way. In particular I am going to present a whole tool-chain that generates the required 3D data automatically and in a reliable and reproducible way. The generated high quality meshes are organized and managed in a new 3D bone database, which is the fundamental data source for the newly developed software tools. Along with the new delivery simulation I present a novel approach of a CAD[1] system which is especially designed for medical evaluations to enable geometrical measurements on large amount of clinical samples. Together with the simulation results the measurements can be statistically examined and were used by myself to derive a mathematical prediction model to forecast possible complications during a natural vaginal birth.

First I am going to present a new software pipeline developed to create the bone database by processing the original medical raw data to generate high quality triangulated 3D meshes in an efficient way. The generated meshes will be processed by various algorithms automatically and deterministically.

Second, I present a new CAD System which uses the bone database along with point correspondence information which I once created for a given template bone and all the available sample specimens in the created database. With that novel approach significant speed-ups are possible and a lot of sources of errors can be avoided as the measurements need to be defined only once and can then be evaluated automatically on all samples.

Third, I will present a new geometrically based delivery simulation in 3D, reproducing the birth mechanics, which is the first time to my knowledge that it will be possible to calculate the baby's trajectory through the mother's inner pelvis - the parturient canal. Starting with engagement, descent, the head's flexion, inner

[1] CAD - Computer Aided Design

rotation to complete extension of the fetal head the whole trajectory is simulated in an objective and non-constrained way limited only by the mother's anatomical structure. To efficiently calculate the 6 DOF[2] optimization problem in discrete time steps along the trajectory, an efficient GPU[3] based algorithm is presented. Furthermore I am going to present an efficient collision detection algorithm which determines the collisions between the baby and the pelvic bone.

Fourth, I will present methods which helped medical experts to analyze the intra- and inter-patient shape's variances of the pelvic bone. The point correspondences are used to generate new mean shapes and I am going to present a novel use case of Point Distribution Models (PDMs) in obstetrics: The shape variance analysis of anatomical structures like the mother's pelvis. It is the first time to my knowledge that such an approach has been used in the field of obstetrics. With these techniques of visualization and shape analysis medical experts can now investigate specimens even further to find regions of potential interest on the pelvis' surface.

Fifth, I am going to demonstrate how the highly predictive measurements and the results of the new delivery simulation can be combined to create new prediction models for a better risk analysis of a natural vaginal delivery.

[2] DOF - Degree of Freedom
[3] GPU - Graphics Processing Unit

Zusammenfassung

In dieser Arbeit stelle ich eine neuartige, hochentwickelte Geburtssimulation vor, die auf einer großen Anzahl von klinischen Daten beruht, und wie diese klinischen Daten effizient verarbeitet werden können. Im Besonderen präsentiere ich eine Software-Pipline, mit deren Hilfe es möglich ist, die erforderlichen 3D-Daten automatisch und reproduziert zu erstellen. Die generierten qualitativ hochwertigen Dreiecksmodelle werden in einer neuartigen 3D-Knochendatenbank verwaltet. Sie stellt die grundlegende Datenquelle für die neu entwickelten Algorithmen dar. Neben der neuen Geburtssimulation stelle ich einen neuartigen Ansatz für ein CAD-Systems vor, das speziell für medizinische Auswertungen entwickelt wurde, um geometrische Messungen an einer großen Anzahl von klinischen Datensätzen zu ermöglichen. Zusammen mit den Simulationsergebnissen können die gewonnenen Messwerte statistisch untersucht werden und bilden die Grundlage für ein mathematisches Modell, um möglicherweise während einer natürlichen vaginalen Geburt auftretenden Komplikationen vorherzusagen.

Zunächst stelle ich die neue Software-Pipeline vor, die entwickelt wurde um die Knochendatenbank zu erstellen. Mit ihrer Hilfe werden qualitativ hochwertige Dreiecksmodelle aus den klinischen Rohdaten mittels verschiedener Algorithmen automatisch und deterministisch erzeugt.

Zweitens, präsentiere ich ein neuartiges CAD[4] -System, welches die Knochendatenbank zusammen mit Punktkorrespondenzen, die einmalig für ein bestimmtes Knochentemplate und allen vorhandenen Proben aus der Datenbank vorberechnet wurden, nutzt. Mit diesem neuen Ansatz sind signifikante Zeitersparnisse möglich und eine erhebliche Anzahl von Fehlerquellen kann vermieden werden, da die Messungen nur einmalig definiert werden müssen um anschließend automatisch auf allen Proben aus der Datenbank ausgewertet werden können.

Als Drittens zeige ich eine neue Geometry-basierte Geburtssimulation in 3D,

[4] Computer Aided Design

um die menschliche Geburt nachzubilden. Dadurch wird es möglich, eine Trajektorie des Kindes durch das Becken der Mutter - dem Geburtskanal - zu berechnen. Ausgehend vom Eintritt des kindlichen Schädels in die Beckenhöhle, dem Absinken und der Flexion, inneren Rotation bis hin zum vollständigen Austritt des fetalen Kopfes wird die Trajektorie in einer objektiven Weise, nur durch die anatomischen Strukturen der Mutter begrenzt, berechnet. Um das 6-dimensionale Optimierungsproblem für die diskreten Zeitschritte der Trajektorie effizient zu lösen, wird ein GPU[5]-basierter Algorithmus vorgestellt. Desweiteren präsentiere ich einen effizienten Algorithmus zur Kollisionserkennung zwischem dem Neugeborenen und dem Beckenknochen.

Viertens zeige ich Methoden, die es medizinischen Experten erlauben die intra- und interindividuellen Variationen der Beckenform von Patienten zu analysieren. Mit Hilfe der Punktkorrespondenzen wurden neue Durchschnitts-Becken generiert. Die Formvarianzanalyse des mütterlichen Beckens stellt ein neues Anwendungsgebiet für Point Distribution Modellen (PDMs) dar. Es ist meines Wissens das erste Mal dass solch ein Ansatz im Gebiet der Geburtshilfe angewendet wurde. Mittels dieser Techniken der Visualisierung und der Formanalyse können nun Mediziner die klinischen Daten grundlegend untersuchen und potentiell interessante Oberflächenstrukturen identifizieren.

Zuletzt zeige ich auf, wie die hochprädiktiven Messungen und die Simulationsergebnisse der neuen Geburtssimulation kombiniert werden können, um neue Vorhersagemodelle zur Risikoanalyse einer natürlichen vaginalen Geburt zu erstellen.

[5] Graphics Processing Unit

Acknowledgements

I want to thank all people who have helped to make this work possible.

First and foremost, I want to thank my advisors, Prof. Dr. Rüdiger Westermann and Priv.-Doz. Dr. Rainer Burgkart.

Prof. Dr. Rüdiger Westermann for giving me the chance and support to make this thesis at his chair of computer graphics and visualization.

Priv.-Doz. Dr. Rainer Burgkart for introducing me to the basics of medicine and gynaecology and his interdisciplinary advice and support were essential for the success of this work. His experience as a paediatric orthopaedic and his interdisciplinary knowledge was always an enriching experience.

I want to thank Dr. Heiko Gottschling for having fruitful discussion at our white-board. His former work and results from his thesis were the basis for our BioCAD Software Framework and our software tools we have developed together in the last couple of years.

Special thanks go to Stryker Corp. for their permission to use their collected datasets for this thesis.

The results presented in this thesis have been originally published in a number of research papers that I have co-authored with Heiko Gottschling and Rainer Burgkart. I want to thank my co-authors for helping me to obtain these results by contributing their ideas and suggestions.

I also want to thank my colleagues from the biomechanics lab at Klinikum Rechts der Isar, Orthopädie. Namely Peter Foehr and Constantin von Deimling for their support for special adaptation of hardware tools like the tracking device's tripod which can be used in a delivery room and for obstetric surveys.

I particularly want to thank my parents for always supporting me during my years of study.

Contents

List of Figures

List of Tables

List of Algorithms

Chapter 1

Introduction

Every birth is a complex interaction of many different factors which refer to the mother on the one hand and to the baby itself on the other hand. The mother with her passive anatomical structures such as her pelvic bone, which differs widely in shape and size and her active parts like her uterus, which moves the fetal body through the mother's pelvis by contractions of her uterus.

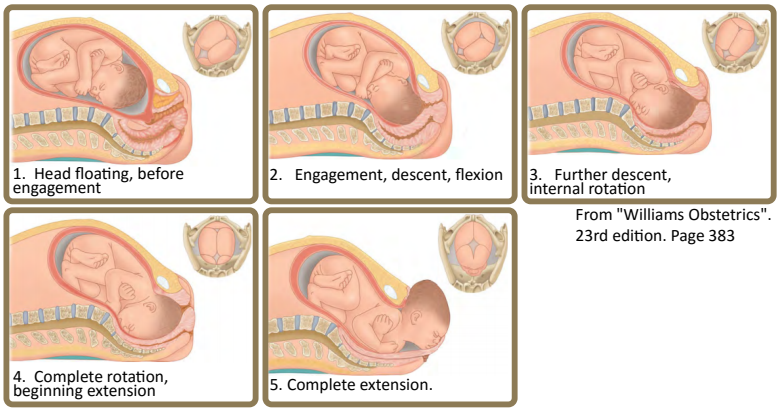

Figure 1.1: Sequence of phases during a natural vaginal delivery.

Illustration 1.1 shows a schematic overview of a vaginal delivery and birth mechanics in different phases. The baby is lying within the uterus in a normal position: The fetal body is oriented longitudinal and is in a vertex presentation - meaning that the baby's head is above the mother's pelvis leading the baby's body through the parturient canal. The baby head enters the mother's pelvis (Engagement - in phase 1 and 2) and rotates within the inner pelvis to max out the overall space and volume which is limited by the bone structures. See phase 3 and 4 for that. On leaving the mother's pelvic bone the baby rotates back and completes the Extension in phase 5. The newborn's body follows the head.

As a natural delivery is a complex process it is common that complications

are possible and occur during the labor work. A study "Complicating Conditions of Pregnancy and Childbirth, 2008"[1] from the Healthcare Cost and Utilization Project (HCUP) from the Agency for Healthcare Research and Quality in the US lists 3.950.300 delivery stays in American hospitals in 2008. Among that 16.5% are related to the so called obstructed labor, meaning that complications during the delivery occurs as the baby could not move further in the inner pelvis and finally stuck. This can happen due to abnormal forces of labor (11.1% in the mentioned study) and a Fetal Pelvic Disproportion (5.4%). In contrast to abnormal forces of labor which could be treated with hormones such as Oxytocyn for amplifying labor forces a Fetal Pelvic Disproportion can lead to a secondary section as an emergency surgery. In case of a Fetal Pelvic Disproportion the baby could not move any further as there are disproportions between the baby's head or body and the mother's pelvic bone. The baby's head can be too big for the mother's anatomical structures or the mother's pelvis can be deformed in some way.

As already mentioned the pelvic bone of the mother as part of the human skeleton plays an important role. The soft-tissue such as muscles (uterus, pelvic floor muscles), filament and urinary bladder are pushed aside - to a certain degree - and are compressed during a natural delivery to increase the available volume. Because of that the bony structures limit the available space for the most part.

1.1 Medical Background

In the following a short overview of the medical background is given relating birth mechanics, the pelvic bone and the fetal head.

1.1.1 Birth Mechanics

The birth mechanics is shown in figure 1.1 on page 1. The baby enters the pelvis of the mother in the first two phases. In phase 3 to 4 the fetal head rotates within the pelvic cavity to max out the available space and volume and exits the inner pelvic cavity in phase 5 showing backward. The current position of the baby's head is given by a metric scale called "Fetal Station", which describes the relative position of the baby's head to the Interspinal Plane (shown in in figure 1.2). The given range of this value usually is $[-4; +4]$ cm where 0 cm is located on the imaginary Interspinal Plane (ISP) - defined by the line between the two spinal

[1] Agency for Healthcare Research and Quality in the US, 2015-05-25, *www.hcup-us.ahrq.gov/reports/statbriefs/sb113.pdf*

points - A and B - and parallel to the pelvic floor - having negative values above and positive values below that plane.

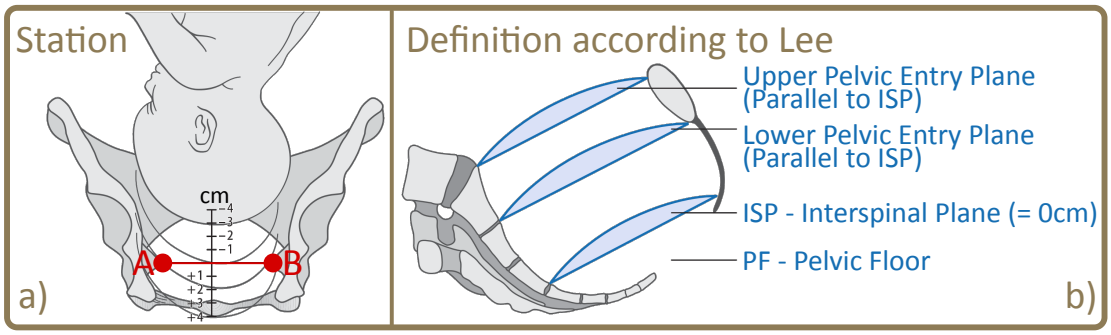

From "Die Geburtshilfe" - 4th edition. Page 692.

Figure 1.2: The station's definition during a vaginal delivery.

A more elaborate introduction of the pelvic bone is given in the following section.

1.1.2 Pelvic Bone

The pelvis is a complex bone which consists of multiple bones. A schematic overview is given in figure 1.3a from [PBM01]. The previously mentioned sacrum is the triangle-shaped bony structure on the back side where the vertebral column ends. The lowest part of the sacrum is the Coccyx. The sacrum is enclosed on both sides by the Os Ilium. The frontal part is made of the Os Ischii and Os Pubis.

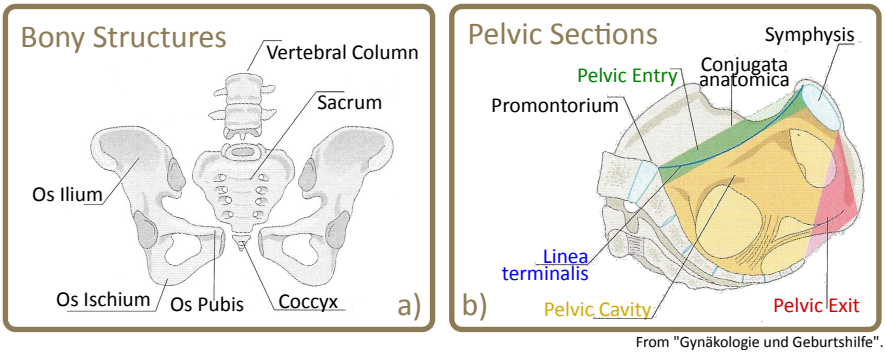

From "Gynäkologie und Geburtshilfe".
4th edition. Page 378.

Figure 1.3: The bony structures of a pelvis (a) and the pelvic sections which are relevant in obstetrics(b).

This single parts are bound by joints which are made of cartilage and grow together during the puberty. Such kind of cartilage can also be found at the Pubic Symphysis on the front side of the pelvis.

The pelvis can be subdivided into three different sections (see figure 1.3b from [PBM01]) such as the entry section which represents the upper part above the Pelvic Brim. The upper section is limited by the sacrum (below the Promontorium) and the Symphysis. The Conjugata anatomical defines the most narrow region of the pelvic cavity. The pelvic cavity is located in the middle part of the pelvic bone enclosed by the Brim Area and the Pelvic Floor. The Pelvic Floor represents the lower section of the pelvic bone.

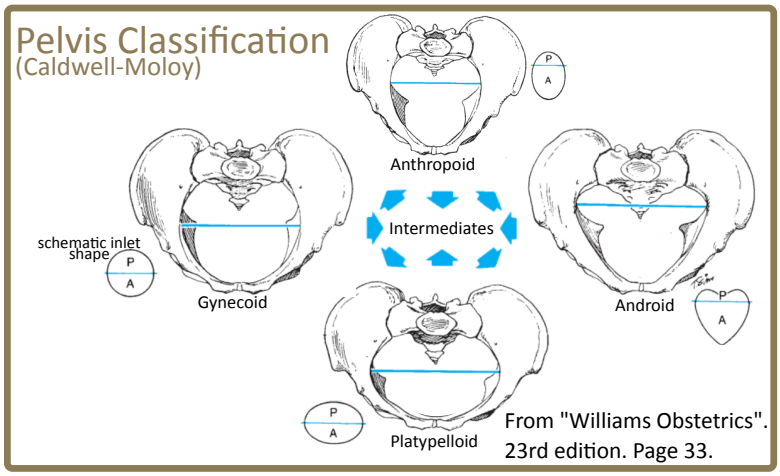

Figure 1.4: The four pelvic types of the Caldwell-Moloy classification. A line passing through the widest transverse diameter divides the inlets into posterior (P) and anterior (A) segments.

The pelvis varies widely from patient to patient in its shape and size. In medical literature there exists a pelvic classification which is presented in fig. 1.4 and was introduced by Caldwell and Moloy (see [CLB+09]). The presented types classify the female pelvises according to their shapes.

- **Gynecoid** A "gynecoid pelvis" represents the so called normal female pelvis. Its respective inlet shape, which is drawn beside the schematic pelvis, is slightly oval (with greater transverse diameter), or is round. Compared to the other types, such a female pelvis is more spacious and is described as being well proportioned. In Caldwells's study about 50% of the examined specimens are classified this way.

- **Anthropoid** The second type out of the four is "Anthropoid" and describes female pelvises having straight walls, a small pubic arch and large sacrosciatic notches. Also the sacrum is usually straight and the spines are placed widely apart. Such pelvises typically tend to non-obstructed labor. About 25% of the tested female specimens belong to that category.

- **Android** Android female pelvises show more masculine features. This can

be seen at the inlet, which looks more heart shaped. This is caused by a more prominent sacrum resulting in a more reduced space within the inner pelvis. About 33% of the examined samples showed such features and were classified into that category by Caldwell.

- **Platypelloid** A "platypelloid pelvis" represents female pelvic bones which are transversally wide, having a flattened shape. Also pelvises of that type have greater sciatic notches, similar to male ones. Their sacrum is rather short and curved inward reducing the available space within their inner pelvic cavity. Due to this, such female pelvises are associated with delivery problems. Caldwell identified less than 3% of his samples having that type.

1.1.3 Fetal Head

The baby's head is the largest part of the newborn's body and leads in most cases the way through the parturient canal during a vaginal delivery. Once it has reached the pelvis exit, the remaining body will follow the head's trajectory. Along the head's trajectory the fetal head rotates within the inner pelvis to max out the available space.

In addition, the fetal skull consists of multiple plate-like bones which are not entirely connected, having small spaces between them: the fontanels and sutures. With the help of the fontanels and sutures - which are described as membranous gaps between the bones of the baby's skull - the fetal head can be transformed and compressed by the labor forces to reduce its volume. The bony plates not only allow to compress the membranous gaps, but they can also overlap to a certain degree each other. After the compression the skull relaxes and the bony plates will return to their original places and restore the original head's volume.

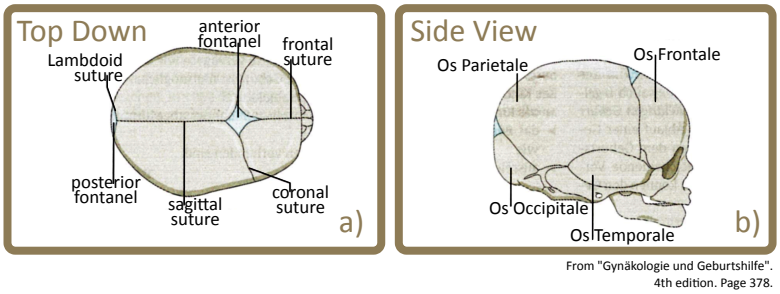

From "Gynäkologie und Geburtshilfe". 4th edition. Page 378.

Figure 1.5: Schematic view of the fetal head from top (a) and side (b). The fontanels, sutures and the bony structures of the fetal skull are shown.

Figure 1.5 shows 2 different views of a schematic fetal skull which is made of multiple bony structures. Between the bony structures the fontanels (anterior, posterior fontanel) are visible in illustration 1.5a. Beside others the bony plates

like the Os Parietale, Os Frontale, Os Occipitale and Os Temporale are visible in the side view (fig. 1.5b).

Using such a flexible anatomy the fetal pelvis can be adapted to mother's anatomy given by her pelvic bone.

1.2 Pelvimetric Measurements

To overcome the risk of obstructed labor, gynaecologists, in case of uncertain size mismatches, often opt for a caesarean section to bear the child in contrast to giving birth in a natural vaginal way. If obstetricians had a more reliable tool to analyze the anatomical interaction during the vaginal delivery, they could have a better data foundation for their risk analysis and their resulting decision.

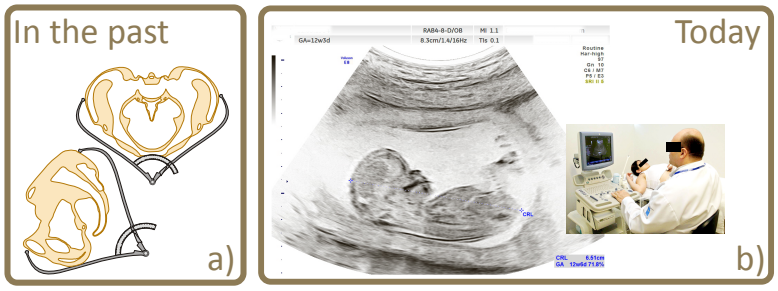

Figure 1.6: Pelvimetric measurements using pelvimeter after palpation of the bony structures of the female patient (a) and ultrasound images (b). The ultrasound image in (b) has been inverted.

To gain insight in the birth mechanics, gynaecologists defined some measurements for distances and angles on the pelvis to examine their relations and calculate the available space and volume of the pelvic cavity.

In the early days before gynaecologists used ultrasound imaging for their examinations they more often used devices which are called "Pelvimeters". Such a pelvimeter is presented in fig. 1.6a.

Nowadays gynaecologists use ultrasound imaging during their pregnancy examinations, which are done routinely during the time of pregnancy. A typical scenario during such an examination is shown in figure 1.6b where ultrasound is used for image acquisition.

Based on that, measured and recorded data are obtained. But which measurements are currently proposed in literature and used in examinations? What are the criteria which are currently used for a risk analysis? In the following a few examples of such indices are given.

1.2.1 Pelvic Narrowing

The pelvis is subdivided into 3 different sections: The entry, middle and exit part. During a vaginal delivery the baby has to travel along the inner pelvis passing through all three sections. If the pelvic sections are very narrow the baby does not have enough volume and space. Then there is a given risk for obstructed labor.

There are some definitions (see [SHS10]) which describe some key values for identifying narrowings in the three different sections:

- **Entry** A patient's pelvis has two diameters in the entry sections. They are called "Diameter Transversalis" and the "Conjugata Vera Obstetrica". Both measurements are displayed in figure 1.7. The entry section is classified as narrow if the following criterion is fulfilled:

$$\text{Diameter Transversalis} + \text{Conjugata Vera Obstetrica} < 220 \text{ mm} \tag{1.1}$$

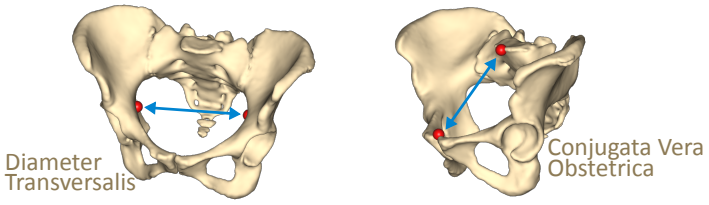

Figure 1.7: Diameter Transversalis and Conjugata Vera Obstetrica as indicators for a pelvic narrowing in the entry section.

- **Middle** To test for a narrowing in the middle part, two measurements are defined. They are called "Straight diameter of pelvis tightness" and the "Intertuberal Distance". These measurements are presented in figure 1.8. Using these measurement values, a pelvic middle section can be classified as narrow if:

$$\begin{aligned} &\text{Straight Diameter of Pelvis' Tightness} < 100 \text{ mm} \quad \wedge \\ &\qquad\qquad \text{Intertuberal Distance} < 110 \text{ mm} \end{aligned} \tag{1.2}$$

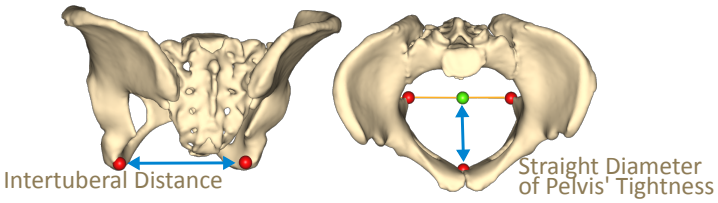

Figure 1.8: Measurements for the middle section.

- **Exit** The measurements' definitions for the exit section are presented in rendering 1.9. A pelvis has a narrowing in the exit section if the following is fulfilled:

$$\begin{aligned} &\text{Intertuberal distance} < 100 \text{ mm} \quad \vee \quad sum < 300 \text{ mm} \\ &sum = \text{Straight Diameter Pelvis Exit} + \\ &\qquad \text{Intertuberal Distance} + \text{Interspinal Distance} \end{aligned} \tag{1.3}$$

Figure 1.9: Measurements for the exit section.

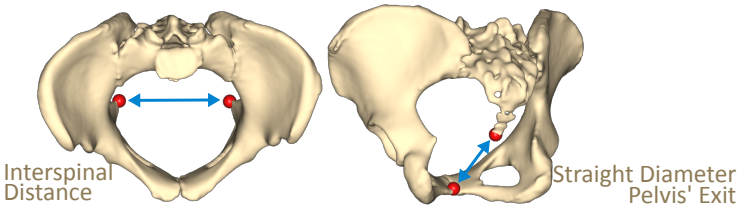

1.2.2 Fetal Pelvic Index

Gynaecologists have promoted some key features such as the Fetal Pelvic Index (FPI) as a key measure to decide whether a Fetal Pelvic Disproportion exits for a mother and her unborn child or not. Such a Fetal Pelvic Index is calculated with the help of measurements obtained from medical examinations during the time of pregnancy. The measurements are performed via ultrasound to derive some values like the "Conjugata Transversalis" representing the widest diameter within the Brim Area.

Figure 1.10 shows the relevant distances on the pelvis' surface and the respective measurements on the baby's body like the baby's head circumference to calculate the Fetal Pelvic Index according to [SHS10]. The circumferences of the ellipses are approximated using a factor of $1.57 \approx \frac{\pi}{2}$.

In clinical examination the given standard form (see fig. 1.10) is used to determine the Fetal Pelvic Index (FPI).

A Fetal Pelvic Disproportion exists if the sign of the Fetal Pelvic Index is positive ($FPI \geq 0$).

More information about the accuracy of the pelvimetrical measurements using Magnetic Resonance Imaging (MRI) regarding the FPI is given in [KSL+10].

The presented indices which are currently used for risk analysis have been examined in various studies and are often discussed controversially. For example there are studies which show that the Fetal Pelvic Index alone does not have a predictive value for the Fetal Pelvic Disproportion [FND+98, BV04].

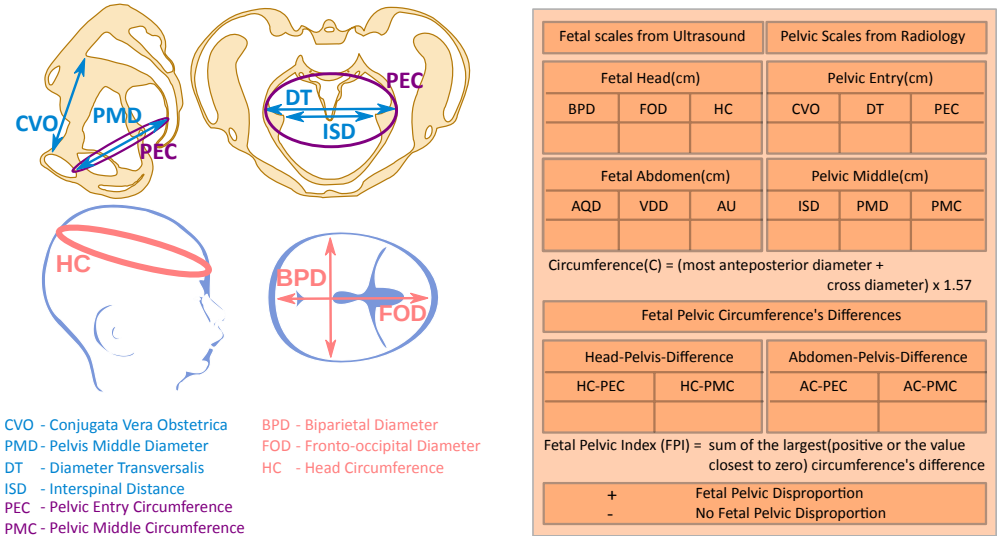

Figure 1.10: Pelvimetric measurements and fetal head measurements for determining the Fetal Pelvic Index [SHS10].

More related work regarding the pelvimetric measurements and cephalopelvic disproportions are given in [KTH13, LJW+10].

1.3 Anapelvis

In [MWW02] a prototypical computer program called "Anapelvis" was introduced in 1998, which uses 2D measurements to calculate a predictive value for a risk analysis. The value is based on pelvimetric measurements which have to be done via ultrasound and entered via manual input. The list of the measurements used has not been published and was derived from the software's Graphical User Interface (GUI).

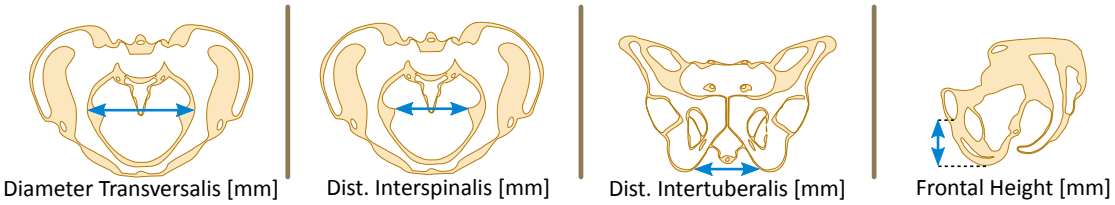

Figure 1.11: Pelvimetric measurements used in Anapelvis.

Figure 1.11 shows some examples of the measurements and their schematic definitions on the pelvis. A complete list can be found in appendix A on page 125.

Based on these measurements, Anapelvis offered a geometrically based delivery

simulation in 2D in later versions. Via geometrical calculations the fetal head was represented by an ellipse which had to travel through the inner pelvic structures in 2D.

To generate the underlying simulation model, no clinical data were used. The authors used results available from medical literature instead but, to our knowledge, did not perform a clinical survey.

1.4 Related Research

Further research was conducted to simulate a human delivery and its influence on post-delivery diseases like Pelvic Floor Dysfunction (PFD) or Pelvic Organ Prolapse (POP).

Pelvic Floor Dysfunction (PFD) describes a wide range of issues regarding weak muscles - Leviator ani and Coccygeus muscle - in the pelvic floor. Symptoms can be e.g. sexual dysfunction, chronic pains and urine/fecal incontinence. Another symptom is the Pelvic Organ Prolapse (POP), which describes the issue of pelvic organs such as the uterus is protruding through the vagina: Prolapsus uteri.

Possible causes for such dysfunctions are childbirth-related damage of the levator muscle and nerves as well as connectivity tissue within the pelvis.

In [HD07] a magnetic resonance tomography (MRT) scan of a 21-year-old woman was used to label the relevant muscle parts of the pelvic floor. These relevant muscle parts are required for a childbirth-related injury simulation. In the following year the same author published a study (see [HDW+08]) measuring a stretch level of the levator muscle during a simulated birth. The birth simulation was done using the segmented pelvic muscles and bone structures from a MRT scan. The parts representing the muscles were modelled using a Finite Element Mesh. The baby was represented as a sphere with a diameter of 9 cm. The deformation of the linear muscle model caused by the baby head was measured at four given different positions. No interpolation between the positions was done. Due to lack of model data for the living female pelvic floor structures, standard values for human muscles were used as material parameters. The study showed a maximum stretch ratio of 3.5 to 1 of such muscles.

A similar delivery simulation was presented in [PNJM+10]. The authors used a Finite Element Model of the pelvic floor muscles and a rigid pelvic bone to simulate the influence of a fetal head flexion on the stress ratio of the pelvic floor.

The bony structures of the pelvis were modelled to be static. The child follows a given trajectory, represented by reference points. The baby head was rigid as well. To simulate the influence of different values of head flexion the simulation was performed multiple times.

The geometrical model used, was presented in [JvdHdB03] and is based on a cadaver scan using a MRT and a 3D palpator device. The muscles' model parameters were measured in a biomechanical lab from that scanned cadaver.

The same dataset from [JvdHdB03] was used in [MPP+07], where the authors utilized the geometrical data and material parameters for another Finite Element Model. Their models are based on special triangular thin shell elements or special brick elements. They also used different muscle models than the ones used in [PNJM+10].

In all these delivery simulations, no clinical data have been used in a larger scale as they use only a single MRT scan from a 21-year-old female or a cadaver scan from an embalmed 72-year-old woman. The model representing the baby is either a single sphere or a tetrahedral mesh representing the fetal body with stiff parameters. No trajectories were calculated but the deformation of the pelvic floor muscles were measured using different stational positions within the inner pelvis.

1.5 Contribution

Until now, no final answer has been given to the question of which measurements and key features have a reliable predictive power for the Fetal Pelvic Disproportion and lead to a higher risk of obstructed labor.

To overcome that, this thesis presents a system which allows a systematic analysis of clinical data to get insight into the 3D anatomy of the human pelvis. This is necessary to determine the intra-individual variance of the pelvis. In the medical overview, a wide range of bone variation and classification has been presented. To do that on a large scale and for a large patient count this has to be done automatically via a computer in a reliable and deterministic way.

Figure 1.12 shows a systematic overview of the different aspects of this thesis. It illustrates how the medical data are processed using segmentation and mesh processing algorithms to collect the generated triangular mesh models along with other patient specific data into a single bone database.

The medical datasets were provided by Klinikum Rechts der Isar and by

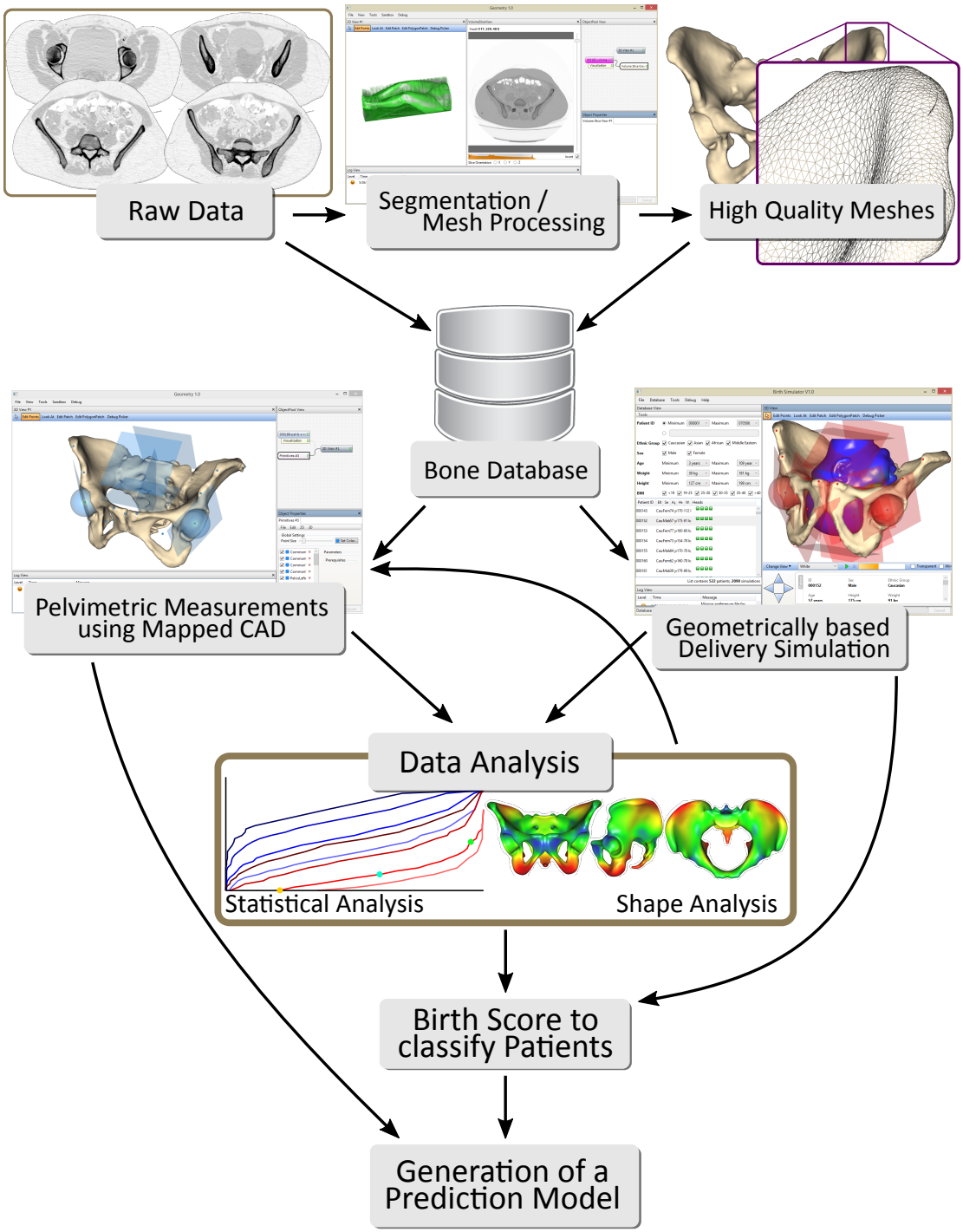

Figure 1.12: A schematic overview of this thesis.

Stryker Corp.[2] and were collected with the patients' consent. The datasets were made anonymous before they were used for a third-party funded project to improve orthopaedic plates. The pelvic datasets along with other bone types were integrated into a bone database which consists of more than 10,000 bones. In addition to the pelvis, bones of the lower and upper extremities are integrated as well as the ribs and the sternum. The use of the pelvis models for the thesis was granted by Stryker.

Medical data are typically generated by medical imaging acquisition devices. Such devices are for example CT- and MRT-Scanners or ultrasound devices. They store their image data in a format described by the DICOM[3] standard. The amount of data not only increases with the patient count but also in the development of the imaging devices. With the help of newer sensors the resolution of the images increases and a better image quality can be achieved. A dataset with more than 1,500 slices by a resolution at 512×512 pixels which has 12-16 bit resolution requires 1.5 GB.

To overcome the drawbacks of available standard CAD software like CATIA[4] or Pro/ENGINEER[5], which cannot handle medical datasets as they are designed for mechanical engineering, a new CAD System for medical research, called BioCAD, has been developed since 2003 at Klinikum Rechts der Isar, Virtual Medicine Group, Orthopedic research. I joined the group in 2003 as a student assistant and have been one of the initial developers of BioCAD since then.

The BioCAD Framework was designed from scratch providing CAD functionality and also handles datasets from medical scanners. Furthermore, features like simple statistical analysis, image and video output were added as well. Data exchange has been provided via the support of standard file formats and direct data exchange to standard software packages such as Microsoft Office[6] and R Project[7].

Medical experts labelled the image data and generated raw mesh models from the medical datasets. The mesh processing pipeline, therefor developed, is pre-

[2] Stryker Osteosynthesis, Prof.- Kuentscher-Str. 1-5, 24232 Schoenkirchen / Kiel, Germany
[3] DICOM: Digital Imaging and Communications in Medicine, 2014-10-16, *http://dicom.nema.org*
[4] CATIA, Dassault Systems, 2014-10-16, *http://www.3ds.com/products-services/catia*
[5] Pro/ENGINEER, PTC, 2014-10-16, *http://www.ptc.com/creo/proengineer*
[6] Microsoft Office, Microsoft GmbH, 2014-10-16, *http://office.microsoft.com/de-de*
[7] The R Project, 2014-10-16, *http://www.r-project.org/*

sented in detail in the following chapter 2 “Bone Database”. The pipeline was integrated in the BioCAD framework to process the large amount of meshes automatically and in a deterministic way. This was necessary because medical studies require a very large number of patients to get a high statistical significance. So for the 500 pelvises which have been used for this thesis, an amount of 750 GB of DICOM data was processed. The meshes were cleaned from artifacts, smoothed, simplified and remeshed to generate the high quality meshes, finally stored in the bone database.

The bone database can further be used to perform the pelvimetric measurements presented in the previous sections. As the workload of the measurements increases with the number of available patients the BioCAD CAD functionality was enhanced to provide a mapping from a template bone to all the available sample bones from the database. With the help of the new Mapped CAD System, which uses correspondence information, it is possible to define a pelvimetric measurement once on a template pelvis and map this measurement to all other sample pelvises from the database, and thus perform the measurement directly on the samples. So medical experts as the users of such a Mapped CAD System can perform the pelvimetric measurements on a large population within seconds instead of evaluating the measurements for every instance of a pelvis sample individually. They are free to define various constructions they are interested in. The constructions can be saved and reproduced along with new ideas. This helps a lot as the time consuming and error-prone individual measurements which have been done manually have become obsolete and are now done automatically in an efficient and deterministic way. It is the first time to our knowledge that such an approach has been realized. In chapter 3 “Mapped CAD System”” the dynamic geometry is presented and the mapping information is described in detail in section 3.2.1 “Correspondence Generation”.

I have published the mapping functionality and its accuracy evaluation combined with the measurements as the leading author in “Automated Morphometric Analysis of the Femur on Large Anatomical Databases with Highly Accurate Correspondence Detection” (see [SGR+14]).

But which are the relevant and predictive pelvimetric measurements? What are the relevant structures which limit the available space and volume for the fetal head? To answer questions like those a statistical analysis of the measurements and the shapes have been performed. The measurements were analyzed according to their predictive power. For example, a single measurement might correlate to

others and is possibly redundant whereas others, are statistically significant and should not be disregarded. The analysis of the bone's shape shows the variance between the different patients. By the shape analysis, the surface regions, with a low or high shape variance, can be identified. That leads to information about potential pelvimetric measurements that are necessary and which are obsolete as they are defined in regions of low inter-patient variance. Chapter 6 "Shape Analysis" describes how different mean pelvises were generated, and a statistical shape model of a pelvis was derived to analyze the shape variance using Point Distribution Models (PDMs).

Moreover, an improved delivery simulation was developed in the presented work. It uses the bones from the database and different baby head models. The simulation is done using geometrical calculations to derive a birth trajectory and the baby head's deformation along that trajectory. Compared to the delivery simulations presented in section 1.4 "Related Research" this simulation uses clinical data. Instead of using only one patient we used more than 500 patients' pelvises and 8 baby head models of different sizes to simulate the influence of the baby's size on the birth outcome. The simulation furthermore uses a geometrical approach to calculate the baby's trajectory and head rotation in such a way that the trajectory is determined by the maximal available space and volume and therefore the minimal head deformation. Previously mentioned delivery simulations use a given trajectory, which has been predefined manually by reference points, for the baby instead. It is the first time to our knowledge that the trajectory and the resulting head deformation is being calculated in an objective way and for such a large sample count. The baby's head was chosen as it is the largest part of the baby and it leads the way in 95% of all vaginal deliveries [PBM01]. The delivery simulation can be seen as an improved version of Anapelvis in 3D, using a large set of clinical data. The algorithm used to calculate the trajectory and the head deformation is presented in detail in chapter 4 "Delivery Simulation".

Along with the pelvimetric measurements, the virtual delivery simulation is done for every patient from the database and generates fundamental data which are necessary for deriving a model potentially capable of predicting obstructed labor.

The statistical analysis of the measurements and the head deformations from the delivery simulation were the basic ingredients which helped to derive an objective prediction index, which will be presented in chapter 5 "Pelvimetric Survey". The prediction index is based on the maximal head deformation along the patient

and baby head's individual trajectory and has been called "Birth Score". It allows a classification of the patients' samples from the bone database. We compared this proposed index to indices from medical literature. The comparison clearly showed a correlation between the birth score and the different indices.

Using the classification based on the birth score it is possible to investigate and analyze the statistical data even further and find out which measurements have a predictive power concerning female patients with no complications compared to female patients with problematic indications. Such an analysis along with the classification enabled us to generate the necessary training data from the highly predictive pelvimetric measurements and the classification which is based on the birth score to derive a prediction model using established algorithms from machine learning. With such a prediction model, a risk analysis for obstructed labor is possible. A detailed description of the model generation and verification is given in chapter 7 "Prediction Model".

1.6 Summary

Having highly predictive internal measurements - which are determined via medical imaging - it could be possible to find further external measurements which correlate to the internal ones. External measurements can be measured while palpation or more modern pelvimeters during normal medical examinations as the acquisition of CT data is not possible for pregnant women. These external measurements replace or at least strengthen the internal ones for generating predicting models which might be more suitable for early and reliable diagnosing Fetal Pelvic Disproportion. That is the point where medical experts like gynaecologists have to take over and might use the basic data and the new developed tools from this thesis in order to continue this research.

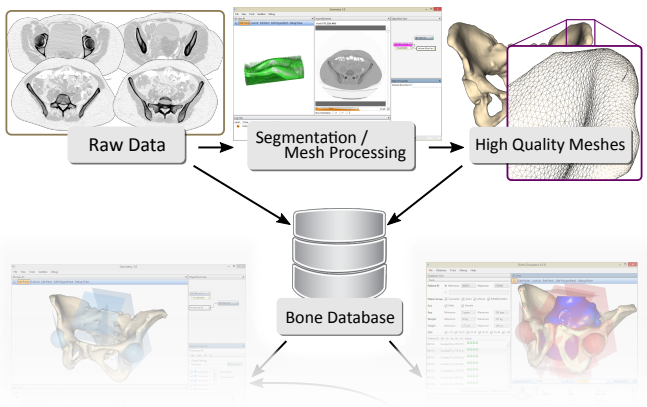

Chapter 2

Bone Database

To generate a prediction model for a risk analysis of a vaginal delivery it is necessary to perform pelvimetric measurements. The measurements can then be used for the machine learning algorithms to derive a prediction model.

To enable such virtual measurements on a large set of data it is necessary to collect and manage the whole data in a convenient and standardized way.

The patients' pelvises, which have been evaluated for this work, were anonymous data from Klinikum Rechts der Isar and from Stryker Corp. and were collected with patients' consent. They are held and managed in a data repository called "Bone Database". The bone database was designed to be similar to a typical database management system.

The following types of data are available in the bone database:

- **Metadata** Besides other data the database holds meta information for the patient. Such meta information are for example values like age, height, weight etc. These values are provided alongside with the mesh data during the import process.

- **Mesh Data** The mesh data represents the actual 3D representation of a pelvis. Such a discretization of the bone's surface is derived from volumetric CT-Scans. Originally these 3D scans are available and encoded in the DICOM format. From this the mesh representation has to be generated via labeling (segmentation). The resulting raw shapes are then imported as raw data into the database. As raw data, they have to be processed further to improve their respective mesh quality.

- **Poses** Poses are another examples of additional data which are stored in the database. Registration poses which align pelvic bones, originating from

	Africa	Asia	Caucasian	Middle Eastern	Total
Male	65	69	132	57	323
Female	41	43	97	33	214
Total	106	112	229	90	537

Table 2.1: Overview of available patients' pelvises within the bone database.

separate datasets, to a common coordinate system are such a type of pose data.

- **Correspondence Information** Correspondence information is another type of bone related data the bone database provides. For every patient's pelvis point correspondences are computed and stored along with the surface data. A more detailed description regarding the point correspondences will be given in section 2.7 "Correspondence Generation" (see page 30).

Technically the meta data is stored in a standard Relational Database Management System (RDBMS) and the larger 3D datasets are held and managed directly via the file system on a server. The poses and point correspondences are stored in separate files beside the mesh data.

BioCAD can connect the database directly to load the required values - for example the meta data for grouping, filtering and classification or the meshes for measurements - from the bone database using the defined API[1]. With such tools the pelvimetric measurements are possible and can be evaluated for all pelvises which are available in the database.

Up to the current date the database consists of 537 pelvises. Table 2.1 shows the available sample pelvis count in detail. The bone database has been extended to support various other bone types like femora, tibia from the lower extremities as well as bone types from upper extremities like humerus, radius, ulna or clavicle and have been used for various medical studies and third-party funded projects to improve orthopaedic plates.

To integrate a new patient in the bone database several steps have to be performed to ensure a consistent and reliable quality of the stored data. The required steps were combined into the so called "Processing Pipeline" which is shown schematically in figure 2.1. The pipeline and all the required algorithms have been implemented within the BioCAD Framework. The single steps of the pipeline will be presented in the following sections in detail.

[1] API - Application Programming Interface

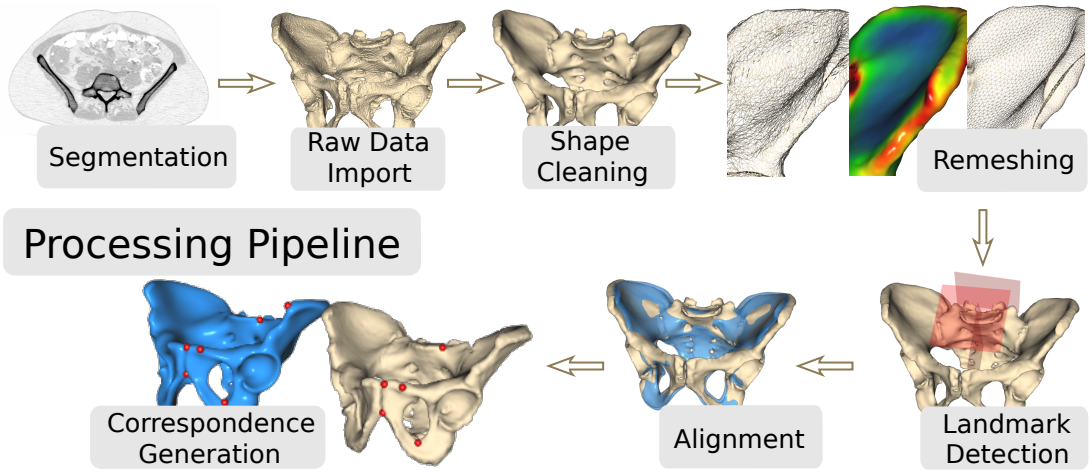

Figure 2.1: The processing pipeline showing the required steps to integrate a pelvis sample into the pelvic database.

2.1 Segmentation

The segmentation process is the initial step for integrating new pelvises into the bone database. It is necessary to generate a 3D mesh model from a volume dataset by labeling the interesting regions in the basic image data. Bone's surface - the cortical bone - is the relevant part in the case of labeling these pelvises. A volumetric dataset consists of a set of ordered image slices. The single image slice has a unique Z position and an extent depending on the sensor's resolution. The 2D-images can be loaded consecutively into memory forming a 3D array. The pixels of an image represent the volume's voxel at a given Z position. Now using the slice distance the pixels are augmented with an extension in Z direction and forming a voxel cube within a regular grid 3D space. The voxels have to be labelled whether they belong to the bone's surface or not while segmenting bones.

Using an algorithms like "Marching Cubes" or "Marching Tetrahedra" one can use a threshold value to extract an iso-surface. But this is not very accurate and useful for the actual labeling process because it is sophisticated to find the optimal threshold value for the algorithm. Such a threshold value depends on every single dataset directly from the CT scanner used and the scanner's settings the medical staff have chosen during image acquisition. Newer scanners have a better image quality than older ones because they reduce the sensor's noise. Also the resolution of the images differs widely from scanner to scanner.

So it would be necessary to perform a histogram analysis for finding a proper

threshold value but it various from bone region to region and so no optimal value exits for the whole image. Therefore a single threshold could not be identified for a single image and especially for an entire 3D scan.

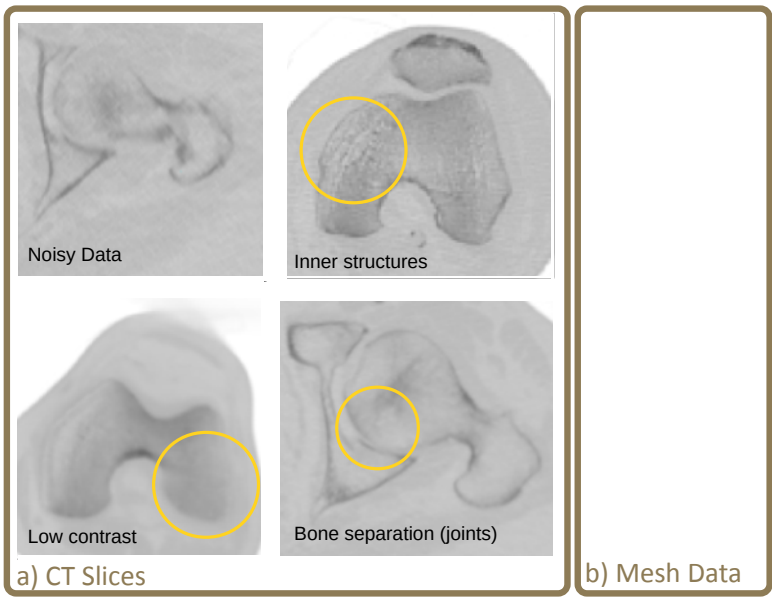

Figure 2.2: Segmentation artifacts and problems due to bad image quality. The images have been inverted.

Figure 2.2 shows an overview of different scans and the varying image quality. It is problematic to correctly locate the bone's surface, being an iso-surface, within the images because of the sensor's noise. Some images for example are of low contrast. Using image filters results in low contrast or amplifying the noise level of the inner structures too. Sharp contours for inner structures on the outer side makes it very hard to distinguish and select the correct bone's surface. Even harder is it in images showing multiple bones which are connected by joints. In the given example regarding joints (see 2.2a) it is very difficult to distinguish between the pelvis' surface and the surface of the femur. Using a threshold value that is too high holes occur in the resulting meshes. If it is too low pelvis and femur will be combined.

To overcome this the labeling have to be done manually by medical experts to ensure the required accuracy. With the help of semi-automatic software tools the segmentation process can be simplified to support medical experts doing the labeling manually.

The resulting meshes and their triangulation depends directly to the volume's grid resolution. A detailed overview of the segmentation process for the femur is given by Timm Surup in [SHH+13].

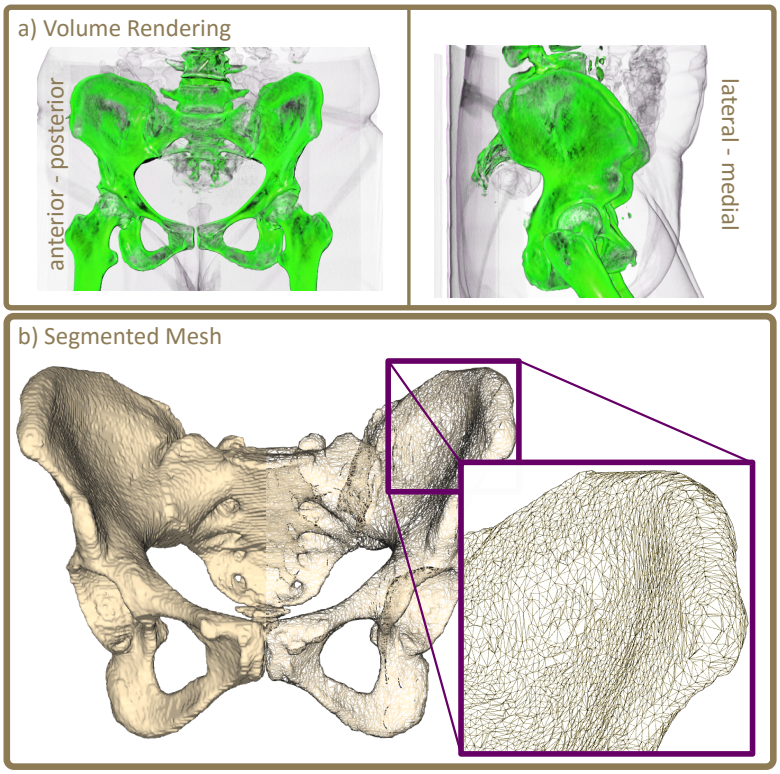

Figure 2.3: Segmentation of a patient's pelvis. (a) Volume Rendering with a special transfer function to highlight the bony structure in green. (b) The generated triangular mesh from that labelled patient.

After the segmentation process bone meshes are available in single STL[2] files and can be imported into the bone database as raw data.

2.2 Raw Data

The raw data models which have been segmented can be characterized by their resolution which directly results in large file sizes due to the very large numbers of triangles used. Another aspect regarding the raw data is the rough surface. This roughness is given by small spikes which are artifacts from the previous segmentation process and the underlying noisy data. The roughness and especially the spikes have to be removed in further processing stages. Figure 2.4 shows a segmented patient's pelvis with a rough surface and small spikes.

Beside the actual 3D data the patient's meta data has to be parsed and imported too. To do that automatically the files have to be named following a specific data code, which can be parsed using regular expressions.

Once the raw data have been imported the files can be cleaned.

[2] Stereo Lithography (STL) files are a standard file format commonly used for 3D mesh data interchange between different CAD software.

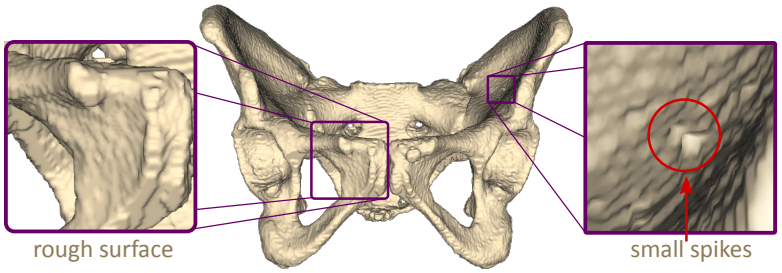

Figure 2.4: Raw data of a segmented patient's pelvis with its rough surface and small spikes.

2.3 Shape Cleaning

After importing the raw 3D data which can be characterized as being rough and stored with a high resolution. Such a 3D mesh has a large file size due to the huge amount of vertex and face information. To overcome this some basic mesh transformation algorithms have to be used for initial mesh processing.

Manifoldness To use meshes as a discrete method for approximating a continuous surface the triangulation of such a mesh has to be "well defined". A mesh algorithm requires that the meshes are manifold. So it is necessary that the bone representation in the database fulfills this requirement.

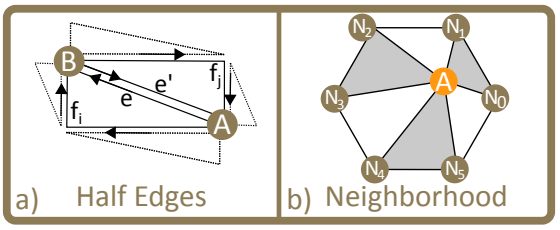

Figure 2.5: Illustration of meshes. Half edges e and e' for AB (a) and neighborhood of vertex A (b).

As a mesh $M := (V, F)$ consists of a list of vertices $V := \{V_i\} \in \mathbb{R}^3$ and the face list $F := \{f_i\} \in \mathbb{N}^3$ the property of being "manifold" is dependent on the face's edges. For a closed mesh being manifold means that every edge AB has exactly two neighboring faces (f_i and f_j) each defining 1 of the 2 half edges of AB: e and e'. Every half edge e of AB has a dual e' - an edge, directing in the opposite direction. This is illustrated in fig. 2.5a. The local disc-like neighborhood - consisting of 6 vertices N_i with $0 \leq i \leq 5$ - of a vertex A is shown in fig. 2.5b.

In figure 2.6 examples of meshes are given to illustrate non-manifold examples in fig. 2.6a and manifold ones in fig. 2.6b.

If a mesh is not manifold something went wrong during the segmentation process and the mesh is rejected and has to be resegmented.

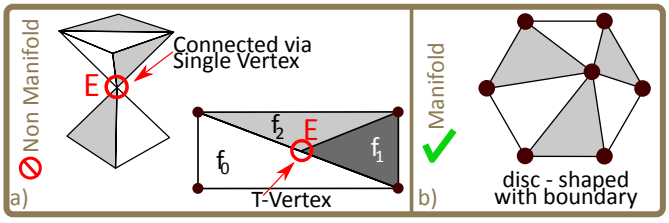

Figure 2.6: Examples of non-manifold (a) and manifold (b) meshes.

Component Analysis After ensuring the manifoldness property the meshes can be further analyzed and processed with more advanced algorithms. As previously mentioned a mesh consists of multiple components and therefore a component analysis has to be used. That is important because small artifacts which have been segmented beside the actual bone surface are stored in a single mesh file as well. These small objects have no connection between them and their set of intersection is empty.

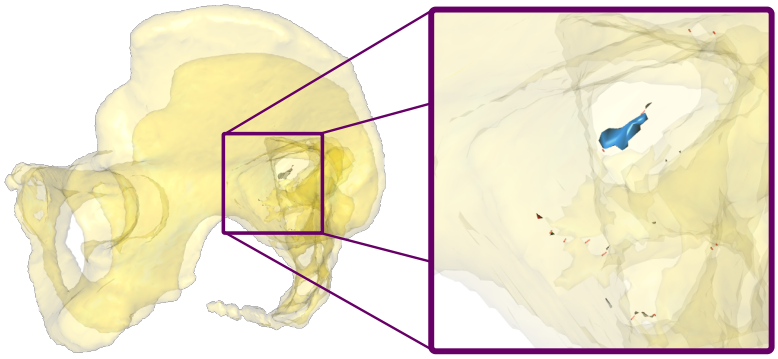

Figure 2.7: Small satellite components resulting from noisy data have to be identified and removed.

So it is important to do a component analysis and filter all small artifacts which do not belong to the actual bone surface ensuring that a specimen consists of exactly one object per file.

The component analysis can be done by a breadth-first search algorithm. Initially all edges of the faces are stored in a heap H. Then, from an arbitrary starting edge s from the heap the algorithm tracks the neighboring edges and faces while they will be individually removed from heap H. If all adjacent elements of a component have been processed, the component has been completely removed from the stack and can be stored as a separate object. The starting edge s is registered in a list C holding all components' start edges.

If the heap H in this state is not empty further non-connected components are available and the process of tracking from an arbitrary edge location starts again. The algorithm terminates when the heap H is empty and all edges have been completely removed.

Algorithm 1 Component Analysis Algorithm

H Heap of all edges
W Working Heap of edges
C List of components' start edges
Find Components:

```
while (H ≠ ∅):
    s ← RemoveFirst(H)
    W ← {s}
    Add(C, s)
    while (W ≠ ∅):
        e ← Dequeue(W)
        for each (n ∈ Neighbors(e)):
            Remove(H, n)
            Add(W, n)
```

To identify such tiny artifacts and determine the relevant parts the found components (in set C) can now be sorted according to key features like for example their bounding box volume, extent or triangle count. Using the bounding box volume and sorting the components in descending order the main component representing the bone data is always the greatest component and the smaller ones can be ignored.

Smoothing To remove spikes on the component's surface which are another aspect as a consequence of noisy data some sort of filtering has to be used. With the help of filtering their bone's surface can be smoothed. Implicit fairing was used to accomplish this task [DMSB99].

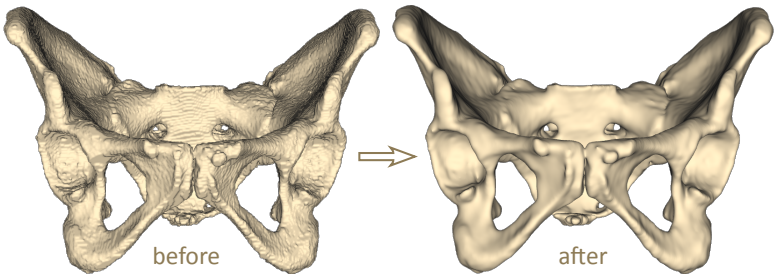

Figure 2.8: Two versions of a segmented patient's pelvis. Before and after smoothing using implicit fairing.

The two renderings in figure 2.8 shows a segmented patient's pelvis before and after the smoothing process.

Simplification The smoothed meshes have the original resolution such as the raw shapes have. Their triangle count is very high and ranges from about $250,000$

up to $1,500,000$. Such a high number is not necessary and a mean triangle area of 2 mm^2 is sufficient enough for an accurate approximation of the bone surface. Pelvises are stored in the database having an average triangle count of $90,000$.

To reduce the triangle count of a smoothed mesh the mesh's edges are classified according to their respective lengths. Another important property of an edge is how planar its neighboring area is. Small edges in a flat planar region can easily removed without altering the approximation of the surface of the bone too much. Along with the edge length the property of having a "planar" neighborhood can be expressed mathematically by a quadric metric presented in [GH97] and [Hop99].

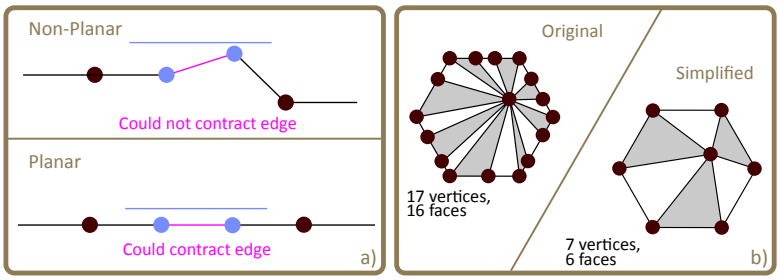

Figure 2.9: Two simple meshes in 2D representing a hexagon. The original structure with 16 faces and the simplified one with 6 faces.

Once such edges have been found the mesh topology will be changed by contracting every candidate edge.

The mesh simplification is illustrated in figure 2.9 showing two meshes representing a hexagon in 2D. The first one - having 16 faces and 17 vertices - will be simplified to become the second one with only 7 vertices and resulting 6 faces.

2.4 Remeshing

As the shape is analyzed of being manifold, smoothed and simplified the triangular structure of the mesh is still related to the initial one from the segmentation algorithm. The triangles can be either small or large with different angles and different faces' areas. A vertex can have only a few adjacent vertices as others tend to have more. These results also in different angles which are defined between a pair of adjacent edges. The angle values range from being acute to obtuse. The broad spectrum of properties are not eligible for mesh algorithms. An overview of different triangle types and the effect they have on a mesh is shown in fig. 2.10a.

To improve mesh's triangle configuration it has to be remeshed to have a more consistent mesh structure like the recommended one which is presented in fig. 2.10b.

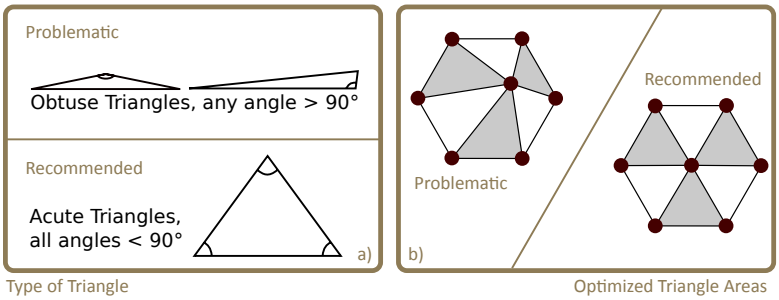

Figure 2.10: Type of triangles (a) and mesh a mesh with optimized areas of the triangles (b).

The range of available angle values becomes smaller and the triangular areas are adjusted accordingly. Such a remeshed version will be stored as another instance within the database and is used as a basis for further algorithmic processing.

In addition a curvature analysis of the pelvis' surface has to be performed to identify regions of high geometrical variations and regions with low variations (see [GHL04] for an introduction to curvature analysis and [Rus04] for the implementation). Figure 2.11 shows a curvature rendering with a heat map. Red regions represent higher curvature values than blue ones.

A higher count of smaller triangles is required in the red regions to retain the accuracy in approximating the bone's surface. In contrast to that, blue regions only need a lower count of larger triangles as there are low geometrical variations in such regions. The remeshing algorithm presented in [SG02] has been used.

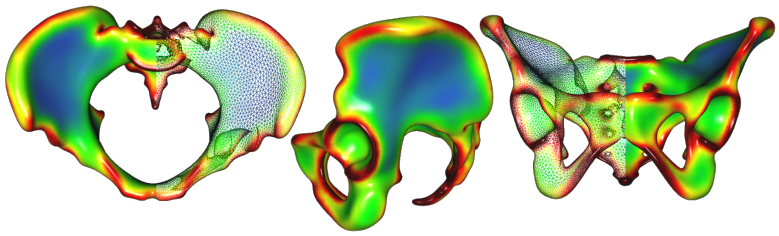

Figure 2.11:

Rendering of a pelvis from 3 different poses using curvature information in a heat map.

The vertices can be move along the bone's surface to alter the mesh structure. Local approximations of the surface is done via PN Triangles [VPBM01] using a Bézier Patch depending on the vertex's normals to interpolate the bone's surface in a smooth and continuous way. See figure 2.12 for an illustration.

The remeshing and simplification can be done iteratively to provide an optimal mesh triangulation for every bone specimen which is finally stored within the bone database.

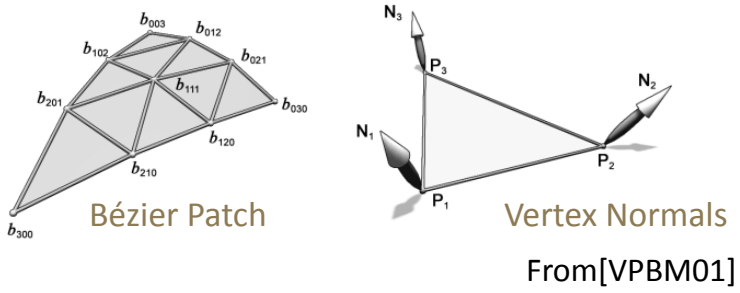

Figure 2.12:

Illustration of a bézier patch and vertex normals to for interpolation of the mesh's surface.

2.5 Landmark Detection

In medical and especially in anatomical literature there have been several landmarks defined which mark and name important features and regions on the bone surface of a pelvis. Some are defined to determine the orientation of the bone and describe in some sense a coordinate system. Such features are the planes such as "Coronal Plane", "Sagittal Plane" and the "Transversal Plane" forming the anatomical coordinate system. A more detailed overview over these medical definitions and terms is given in figure 2.15 on page 29.

Other features are special points of interest such as the "Tuberculum Pubicum", "Symphysis Pubica" or the "Spinae Ischiadica". There are many more landmarks defined. Figure 2.13 shows an overview of the pelvis landmarks which are available in the database.

The aim was to detect these features automatically and store them as geometrical entities within the database so they are available for the evaluations within the CAD system. A detailed description of the Mapped CAD System is provided in chapter 3 "Mapped CAD System" (see page 33). The feature detection was done using various techniques and algorithms.

The common bone related coordinate system, given by the first three planes - namely Sagittal Plane (drawn in blue in figure 2.13), "Transversal Plane" (in red) and the "Frontal Plane" (in green) - were found by detecting the shape's oriented bounding box to get the primary axis as the initial direction hints. Such an oriented bounding box is computed via a principal component analysis (PCA) on the covariance matrix of the mesh vertex's locations. The actual planes are derived via a plane fitting algorithm so that the planes have a stable contact of three points using the direction hints from the bounding box.

Several features are found by fitting spheres and planes from a point set as for example the "Acetabular Rim Sphere" and "Acetabular Rim Plane". The points

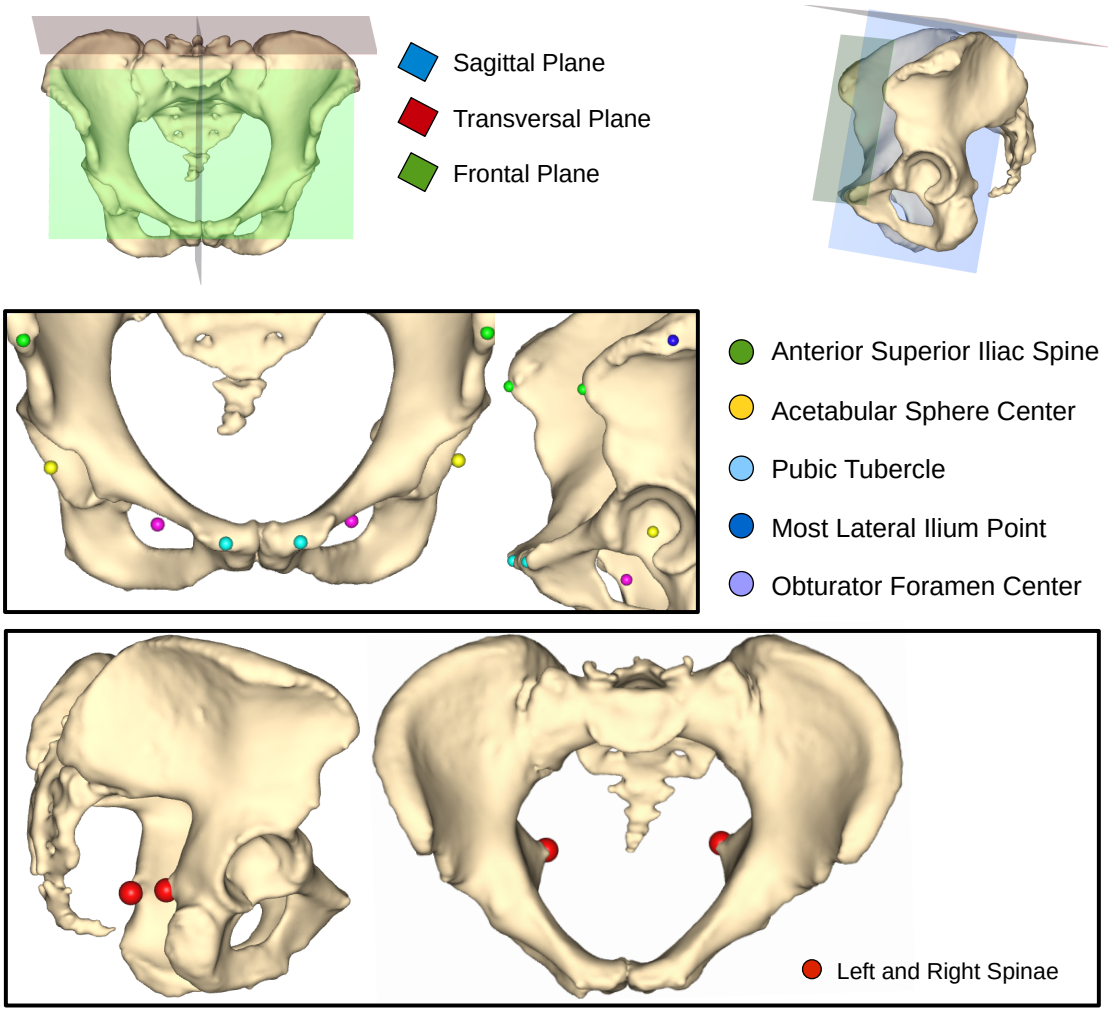

Figure 2.13: Overview of automatically detected landmarks for the pelvic bone.

will be generated via the point correspondence information from the database. That's the reason why such landmarks have to be generated in a second iteration if the point correspondences are available. These landmarks are presented in fig. 2.14.

Once the patient specific landmarks have been detected they are stored within the database and are available for further processing for example the pelvimetric measurements.

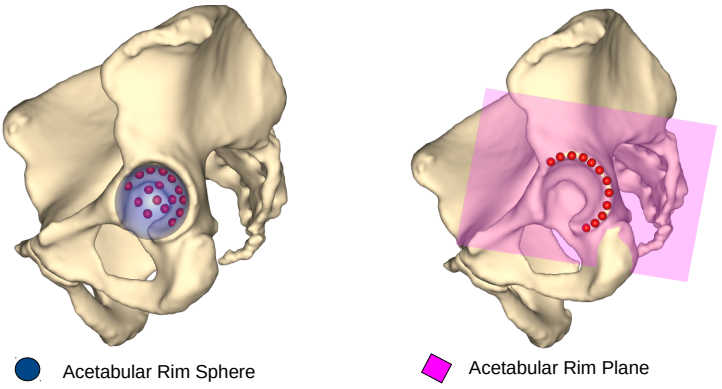

Figure 2.14: Landmarks which are determined using points to derive a best fit sphere ("Acetabular Rim Sphere") or best fit plane ("Acetabular Rim Plane").

2.6 Shape Registration

The single specimens have to be aligned in some common coordinate system so a registration matrix (encoding translation, rotation and scaling) have to be found for every single pelvis. As the bone meshes have been generated via segmentation from the 3D scans the vertex information is given using the scanner's reference system. As the meshes originate from different scans they all have different coordinate systems in which the vertices are defined. To compare the meshes during evaluations they have to be transformed into a common coordinate system A.

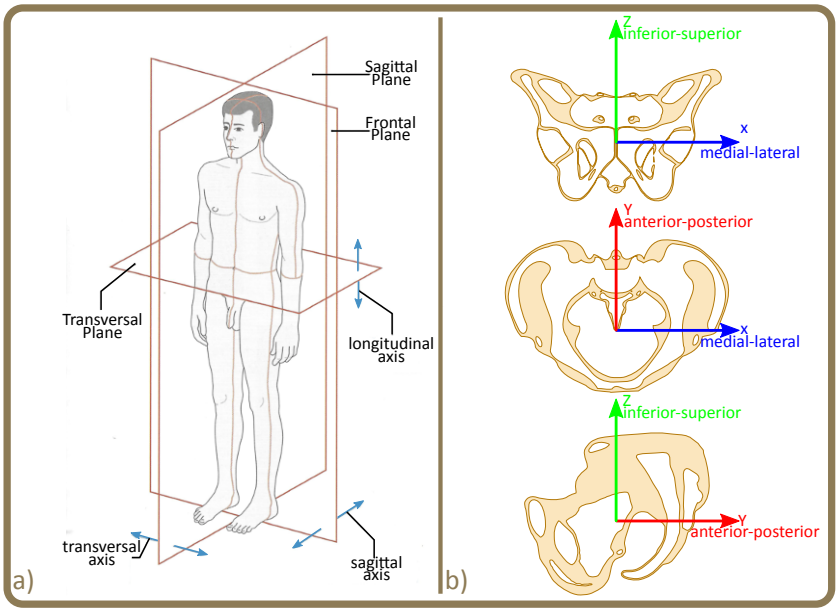

Figure 2.15: (a) Anatomical coordinate system from [SSS09]. (b) Anatomical coordinate system how it is defined for the pelvis shape models within the bone database.

The anatomical system A is defined to be the standard coordinate system of a template pelvis. It is unique for all pelvic samples and has been chosen in a way such that the X direction represents the medial-lateral direction. The anterior-

posterior direction is expressed with the Y axis and Z points inferior-superior. See figure 2.15(a,b) for an overview over the medical terms and definitions.

To find such a registration matrix the shape has to be transformed to a reference shape defining the target system. The resulting matrix ${}^{A}T_{R}$ transforms a mesh from its CT-based raw coordinate system R to an anatomical system A. By applying such a transformation R for all vertices the whole mesh will be transformed accordingly.

$$p_A = {}^{A}T_{R} \cdot p_R \in \mathbb{R}^3$$

The registration matrix ${}^{A}T_{R}$ consists of a rotational and a translational part. These both parts can be found through a standard Iterative Closest Point (ICP) method. The previously detected landmark can be used as the initial values for the ICP procedure. The remaining scaling part of ${}^{A}T_{R}$ is found with the help of Procrustes Analysis.

After the registration process a matrix ${}^{A}T_{R}$ is found and available for every patient's specimen. Using that transformation the samples can be loaded and handled in a common coordinate system.

2.7 Correspondence Generation

After the successful integration and import of a new bone, a high quality mesh is available in the database. It has been generated with the help of the described methods and algorithms from the previous sections.

Similar to the alignment pose which aligns every imported specimen into a common anatomical coordinate system - defined by a template bone - the point correspondence information describes a relation between the sample bone and the template.

Once the samples are in the anatomical coordinate system point to point references can be determined such that an arbitrary point on the template bone can be transferred and encoded in bone surface's local coordinate system. More on that correspondence information and the mapping functionality will be presented in detail in section 3.2 "Mapping" on page 39.

Such point correspondences are generated by using a B-Spline Lattice Θ_{ijk} for a non-rigid registration and deformation together with the alignment pose. More on that is described in the respective section 3.2.1 "Correspondence Generation" on page 42.

This enables the Mapped CAD System (see chapter 3 “Mapped CAD System”) to transfer complete geometrical constructions and measurements which have been defined on the template bone to all sample bones automatically.

Another use case for the point correspondences is the mean bone generation in chapter 6 “Shape Analysis” on page 89.

2.8 Conclusion

A bone database has been presented in this chapter which stores and handles the bone shapes and the patients’ meta data. Beside that registration poses and landmarks are stored in that database. Organizing this anatomical data within a database makes the handling of the data and further processing, evaluation and visualization easier. The database is the basic data source for the evaluations and pelvimetric measurements and for the delivery simulation to gain numerical data which can later be used to define a “Birth Score” the prediction model for a risk analysis of a natural delivery.

The database creation, the import process and the algorithms for the bone shapes have been presented. With that pipeline, the segmented raw meshes can be processed automatically to produce high quality meshes in a reliable and deterministic way. This does not only reduce the amount of work but more importantly ensures a constant data quality which is needed for the evaluation of pelvimetric measurements and the delivery simulation. The rendering in figure 2.16 shows the resulting high quality mesh for the same patient’s pelvis as in figure 2.3 on page 21.

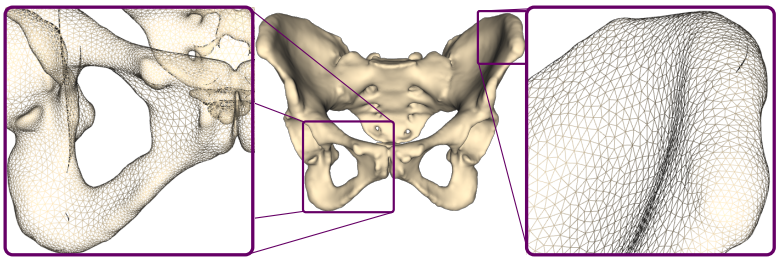

Figure 2.16: Resulting high quality mesh for segmented pelvis of patient 000182.

The greatest challenge of implementing the pipeline and the required algorithms was to ensure that the pipeline is working in a reliable way to process the large amount of data. Not only the 538 pelvises which have been used for this thesis have been processed. So far 1931 patients’ datasets are available in the database and a total count of 10636 single specimens have been processed and the

respective high quality meshes have been generated automatically to get a bone database with currently 26 bone types.

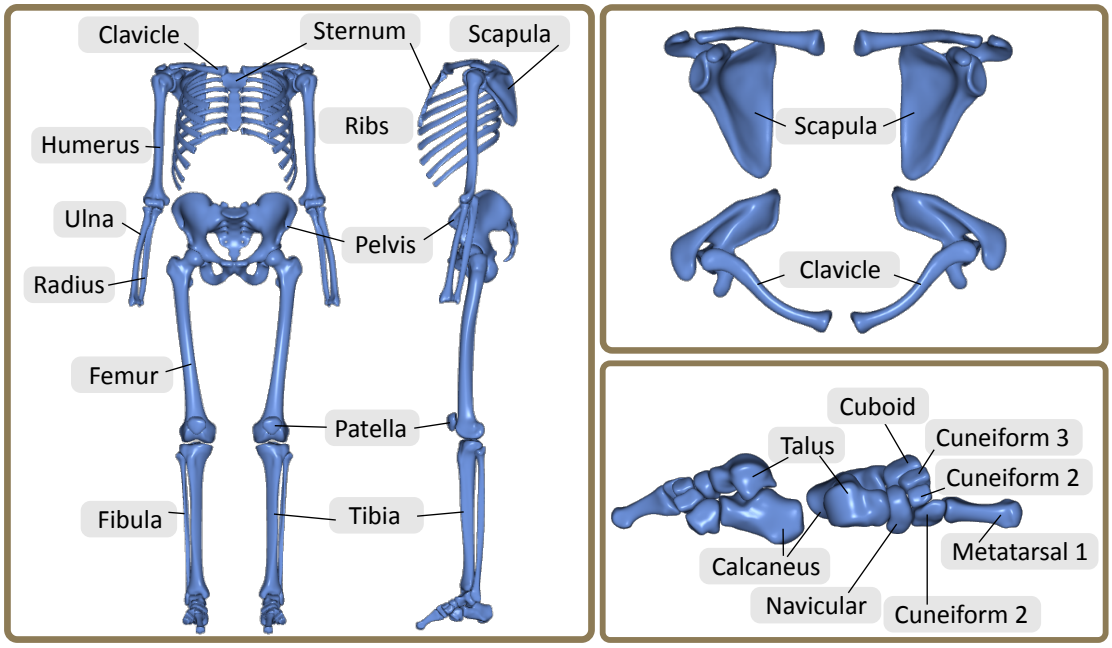

Figure 2.17: Available bone types within the bone database.

Figure 2.17 shows an overview of the available bone types. They have been used for a wide range of medical surveys and third-party funded projects.

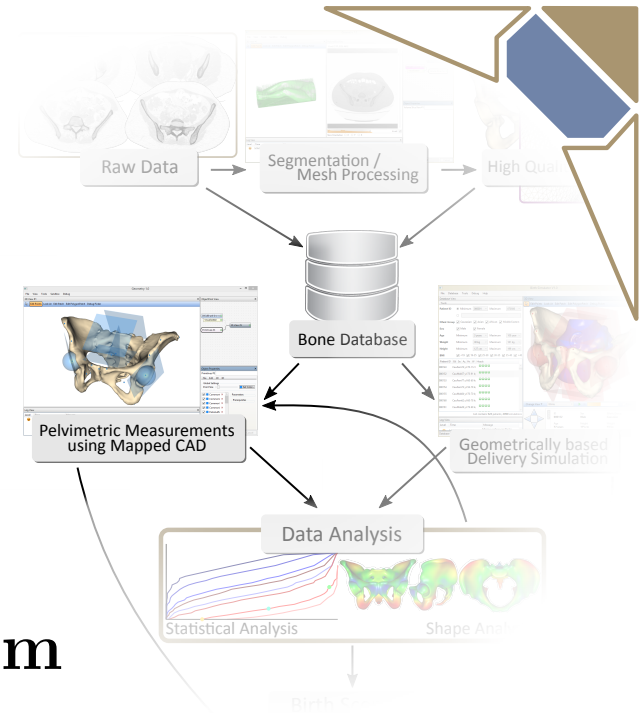

Chapter 3

Mapped CAD System

Geometrical constructions and measurements as they are used in pelvimetry are the basic ingredients for a gynaecological survey. The pelvic samples from the bone database are the subjects of investigation and are measured accordingly. The bone database has been presented the previous chapter and holds the required pelvises for the actual measurements to find indications of possible obstructed labor like Fetal Pelvic Index (FPI) and pelvic narrowings. Such indices rely on simple distance measurements which reveal values which can later be used for statistical evaluations. Statistical evaluations require a large sample count to get a high level of significance. To determine all values the required measurements have to be defined and evaluated for each sample on their own. This is not possible using typical and standard CAD software tools. Neither they can handle medical data directly nor can they connect to the bone database. As a workaround the single generated high quality meshes (see chapter 2 "Bone Database") which represent the pelvises have to be loaded separately and measured for their own by constructing the measurements for each sample individually. The results have to be collected manually via copy&paste in a spread sheet. This is a very time consuming and error prone task. Trained medical experts or biomechanical engineers produced 3-5 samples per hour using the workaround. Once the measurements' definition changes the samples have to be evaluated accordingly by repeating the process for every sample again. For a medical study it is important that the measurements have to be done in a reliable, comparable and reproducible way to ensure the integrity and quality of the measured data.

This chapter is based on material that has been originally published in M. Schröder, H. Gottschling, N. Reimers, M. Hauschild, and R. Burgkart, *Automated Morphometric Analysis of the Femur on Large Anatomical Databases with Highly Accurate Correspondence Detection*, Open Medicine Journal 1 (2014), no. 1, 15-22 [SGR+14].

The aim was to develop a Mapped CAD System which provides the required geometrical constructions and measurements via a dynamic geometry framework and such a system should connect to the bone database directly. Furthermore the measurements should be easily definable via an user friendly GUI so that the measurements can be done by medical experts directly.

The created constructions and measurements are defined once and are encoded using a graph representation. This graph can be seen as a formal geometrical description which can be evaluated on each sample automatically. With such a system the measurements are performed automatically in a determined and reproducible way and ensure a consistent and reliable data quality which is required for medical surveys. The measurements' results are exported automatically as well to be analyzed later. Besides that a set of more than 500 patients have been processed within minutes compared to 3-5 samples per hour doing it manually with a standard CAD system.

3.1 Geometry Framework

A measurement can be described in an abstract way as a geometric construction consisting of geometric entities and their relations. For example a distance has to be calculated between 2 points, A and B. B is defined as lying on a plane P which itself is defined by three other points P_0, P_1, P_2 somewhere on a pelvis' surface. Furthermore B is the projection of the point A onto that plane. Point A itself represents a landmark point called "Left Anterior Iliac Spine" and is patient specifically stored within the bone database.

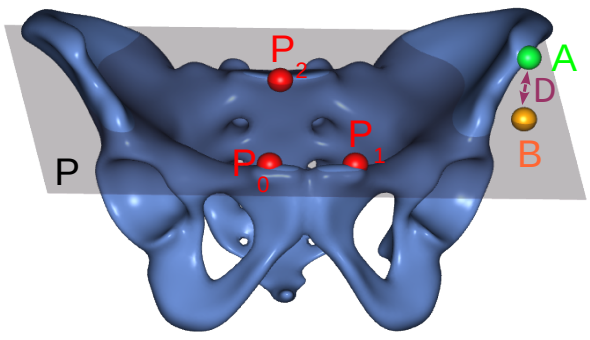

Figure 3.1: Distance measurement between 2 points A and B. B is the projection of A onto a plane P given by 3 points: P_0, P_1 and P_2. The measurement has been defined on a template pelvis.

The geometrical entities in that example are first of all points: P_0, P_1, P_2 and A, B. Then the plane P and the projection operation which projects the point A onto that plane P to get B. This described example is illustrated in fig. 3.1.

In a more general case more geometrical entities are possible and are given in the following overview:

- **Points** As points can be seen as geometrical primitives without any dimension they are the fundamental entities for a geometrical framework.

- **Lines** Other geometrical entities as for example lines can be defined by two given points. Or defining a parallel line L_Q of a line L which is located on a point Q.

- **Planes** A plane can be for example defined by three points. Another possibility is using a point Q and a line L to define a plane.

- **Other Primitives** Similar definitions exist for other geometric entities like circles, ellipses, spheres and so on which can be seen as other geometrical entities which depend on points.

- **Meshes** Beside that, the mesh data itself, which defines the bone surface, can be seen as a geometrical primitive as well which can also be used for evaluations.

- **Intersections** As these geometrical entities can be defined as point sets, it is also possible to define intersections. For example it is possible to calculate the intersection point of two lines, or between a line and plane. The line of intersection between two planes is another example as well of the more complex intersection contour between a plane and a bone mesh.

- **Projections** Projections of points onto lines or planes are possible as well as projections of lines and circles onto planes.

- **Best Fit** In addition circles, planes and spheres can be defined via a fitting algorithm to get for example a best fit plane from a given set of points. For example a least squares approach can be used to get a best fit plane from a set of points which has the minimal distances to all the points.

The landmarks from the database are precomputed geometrical entities and are available in the database to be used within the geometrical framework.

3.1.1 Primitive Graph

A construction can be described and encoded formally via a directed acyclic graph (DAG) G whose nodes are the defined primitives and the graph's edges describe the relations between the primitives.

In figure 3.2 a graph G is shown encoding the given example from the beginning of this section which has been presented in fig. 3.1.

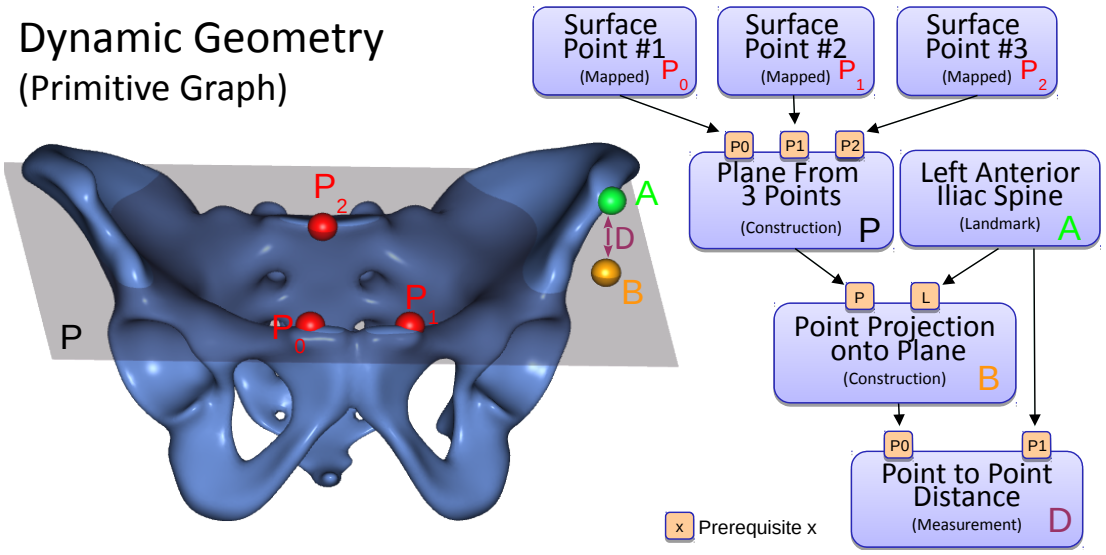

Figure 3.2: Dynamic Geometry using a measurement graph for governing the evaluations. The measurement from fig. 3.1 has been encoded using a graph G.

Because of graph's edges represent the dependencies between the geometrical primitives and entities it is possible to find all primitives which depend on a single point or other basic primitives. Changing that point, e.g. by user interaction or other reasons, only requires the dependent primitives to be updated. That dependency property is given formally as the transitive hull H_p for that primitive p. With this an efficient way of updating the construction is possible because only the affected items have to be updated accordingly.

The primitives a specific primitive depends on are called "Prerequisites". In the example of point distance measurement D, given above, the 2 points A and B are the direct prerequisites of the measurement's primitive. Whereas the plane P has P_0, P_1, P_2 as its direct prerequisites. P, P_0, P_1 and P_2 and the other points A and B form the transitive hull H_D of prerequisites for the measurement D. A more detailed presentation of how to calculate such a transitive hull H_D is given in section 3.1.3 "Dynamic Geometry".

Measurements As a last feature of the geometrical framework measurements can be formally defined within the geometrical framework. A measurement can be characterized by its output value and is a computational primitive which has a numerical output value. For example the distance between two points (Measurement D) can be defined as the Euclidean distance between 2 points: $\|A - B\|$.

Encoded in a graph G the measurement D depends on two point primitives, namely A and B.

3.1.2 Primitives

As mentioned primitives are the basic elements of the geometrical framework. For example points, lines, circles, ellipses, planes and spheres are primitives. Also more advanced primitives such like a triangle mesh can be seen as a mesh primitive. The directed acyclic graph (DAG) G, which encodes the geometrical construction, consists of primitives. As every graph $G := (N, E)$ can be defined as a tuple of a set of nodes N and a set of edges E the primitives are the nodes of the graph. The edges are the dependencies between the primitives and an edge E is defined to be a tuple of two primitives: $E \subset N \times N$.

The graph G is restricted to be acyclic, that means it is not possible to have cycles, which is an important property for encoding constructions, because otherwise it would be possible for a construction to be dependent on its own result.

For example the graph G governing the measurements of two points A and B from the initial example is given in definition 3.1. The point B is part of plane P which itself can be described by 3 points - its predecessors P_0, P_1 and P_2. P is a computational primitive having prerequisites. The same is true for B which is defined to be A's projection onto plane P. As being a computational primitive B has prerequisites itself which are the point A and the plane P in the given example. The distance measurement is done using a measurement primitive D.

$$\begin{aligned} G &:= (N, E) \subset N \times E \\ N &:= \{P_0, P_1, P_2, P, A, B, D\} \\ E &:= \{\{P_0, P\}, \{P_1, P\}, \{P_2, P\}, \{P, B\}, \{A, B\}, \{A, D\}, \{B, D\}\} \end{aligned} \tag{3.1}$$

3.1.3 Dynamic Geometry

In the previous example the point A was a landmark point but it can also be an user defined point which has been defined by the user via the GUI lying on the pelvis' surface. By defining the measurement D's setup similar to the given

example, the whole measurement has to be recalculated every time the user moves the point A on the bone's surface using mouse input.

As the point A's coordinates change as it is moved, the prerequisite for the projection operation B changes and has to be updated as well. This changes the output of B and therefore the measurement D's result.

On value changes of a primitive p's prerequisites, the state of p has to be updated and affects all the primitives which are dependent on that primitive p. The affected primitives are not only the direct successors, but the whole transitive hull H_p which is given by the successor(G, p) operation for the graph G and the primitive p. The graph G encodes the actual construction describing the geometrical entities and their relations. This can happen because an user changes a point's position and the dependent line has to be recalculated.

So it is important for evaluating the whole measurement that the primitives have to be processed and updated in the right order. Because a primitive's new state and value depends on the values of its prerequisites. The non directly adjacent prerequisites are the overall predecessors which can be computed via the graph G using their predecessor(G, p) operation which gives the transitive hull H_p of all prerequisites for a given primitive p.

To evaluate the construction and measurement in the right order the primitives must be sorted according to their dependency information and then evaluated in the resulting order. The ordering depends on the primitive dependencies which are given by the graph's edges. To sort a directed acyclic graph G that way, an algorithm called "Topological Sorting" has to be used.

The topological sorting orders the graph G's nodes in a sequence. The start of that sequence is given by nodes that have no prerequisites. Formally such nodes without any prerequisites can be classified using predecessor$(G, p) = \emptyset$.

This leads to a set of of candidate nodes C which is defined:

$$C := \{c \in N | \text{predecessor}(G, c) = \emptyset\} \tag{3.2}$$

If $C = \emptyset$ the graph is either to be defined as the empty graph $G_\epsilon := (\emptyset, \emptyset)$ without any nodes or edges or the graph G has cycles which violates its definition to be acyclic.

If more than one of such candidates exists - $|C| > 1$ - an arbitrary candidate $c \in C$ can be chosen. The chosen candidate c can be removed from the graph and all edges that start from c will be removed from the set of edges E as well to define a new graph G' which has a subset of nodes and edges of G. Having this

in mind graph G' is defined as sub-graph of G:

$$\begin{aligned} G' &:= (N', E') \\ N' &:= N \setminus c \\ E' &:= E \setminus \{(q, c) \in E | q \in \text{predecessor}(G, c)\} \end{aligned} \tag{3.3}$$

The described algorithm will be now used for the new graph G' to find another set of candidates C' without any prerequisites in G'. The node c' and all edges starting from c' will be removed as well, to get a sub-graph from G'. The sub-graphs will become smaller with every iteration and the whole algorithm terminates when the graph degenerates to be the empty graph G_ϵ.

If the algorithm terminates, it has calculated the required ordering of primitives. According to this ordering the primitives can be updated in a reliable and secure way maintaining primitives' dependencies.

As the ordering does not change until the graph's definition changes - e.g. new primitives were added or old ones are removed - the ordering of the primitives' will stay the same. Once the graph G's definition changes the sorting has to be redone.

3.2 Mapping

In the bone database correspondence information for every single specimen exists beside the actual 3D meshes and meta data. This correspondence information is a mapping from a point X_T on a common template bone to a specific patient's sample point X_S lying on the sample bone's surface. That means for every bone this information is precomputed and held within the database. So it will be usable by special software tools like BioCAD which has been developed to evaluate measurements and connects to the bone database directly. The correspondence information for a given sample pelvis continuously maps points from one common template bone to the sample bone.

To do that, a mapping function has to be defined which consists of several parts to enable the mapping process. The mapping procedure consists of a function $\text{map}(X_T)$ which reveals the mapped point X_S. See equation 3.4 for its mathematical definition:

$$\text{map}(X_T) := \text{surf} \circ \text{deform} \circ \text{affine}(X_T) = X_S \tag{3.4}$$

So it is possible to morph the common template bone applying the correspondence information for the whole surface to the appropriate sample bone. Such a morphing is presented in fig. 3.3 using the different parts of the mapping function separately and successively to morph from the original template to a given patient's sample.

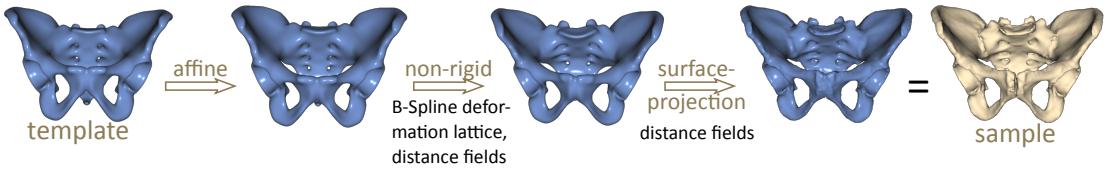

Figure 3.3: Transformations which have to be applied on the template to map its shape to the patient's sample.

First an affine transformation for the given template point X_T has to be applied which translates, rotates and scales the point accordingly. It is is available in the database and was presented in section 2.6 "Shape Registration" on page 29.

In addition a non-rigid transformation is necessary. It is done in the second step which is based on a cubic B-Spline lattice Θ. Points will be transformed by the lattice using the deform(Θ, X_T) function. Following the approach from [HPM06, RSH+99] the non-rigid registration was implemented. The template shape is embedded into a 3D deformation lattice Θ, which is a regular grid whose vertices are control points that can be displaced, thereby controlling the deformation. The displacement of points inside the grid is interpolated using cubic B-Splines, thus guaranteeing a continuous and smooth deformation of the entire shape. The mapping transformation is encoded in the displacement vectors of the grid vertices. Where $\Theta_{ijk} \in \mathbb{R}^3$ is a displacement vector of a grid vertex and the B-Spline lattice Θ is defined to be a set of displacement vectors: $\Theta := \{\Theta_{ijk}\}$. Such a set represents a finite regular grid of L elements in x direction, M elements in y direction and N elements in z direction, respectively. X, Y and Z are the spatial dimensions of the interpolation domain. Hence the deformation can be formulated:

$$\begin{aligned} \text{deform}(\Theta, x) &:= x + \sum_{l=0}^{3}\sum_{m=0}^{3}\sum_{n=0}^{3} B_l(u)B_m(v)B_n(w)\Theta_{i+l,j+m,k+n} \\ \text{with } i &= \left\lfloor \frac{x}{L} \right\rfloor - 1,\ j = \left\lfloor \frac{y}{M} \right\rfloor - 1,\ k = \left\lfloor \frac{z}{N} \right\rfloor - 1 \\ u &= \frac{x}{L} - \left\lfloor \frac{x}{L} \right\rfloor,\ v = \frac{y}{M} - \left\lfloor \frac{y}{M} \right\rfloor,\ w = \frac{z}{N} - \left\lfloor \frac{z}{N} \right\rfloor \end{aligned} \tag{3.5}$$

To deform a point the containing cell and its indices (i, j and k) have to

be detected as well as the interpolation coefficients u, v and w which define the position of x within the cell relative to the enclosing grid vertices. Such a cell is given by 8 grid vertices which describe a box within the lattice. The final position of the non-rigid transformation is calculated by cubic interpolation using the 64 nodes (4 nodes in every one of the three spatial directions) and their respective displacement vectors in its neighborhood. The $B_{l,m.n}$ are the Bernstein polynomials used for the B-Spline interpolation:

$$B_0(u) = (1-u)^3/6\ , B_1(u) = (3u^3 - 6u^2 + 4)/6$$
$$B_2(u) = (-3u^3 + 3u^2 + 3u + 1)/6,\ B_3(u) = u^3/6$$

In section 3.2.1 "Correspondence Generation" the fitting process for the B-Spline lattice will be presented. Figure 3.4 shows an example in 2D how such a lattice deforms a femur's head shape.

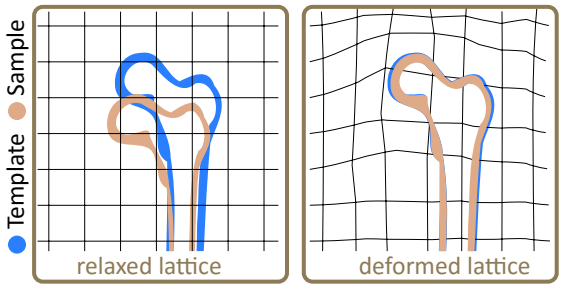

Figure 3.4: Non-rigid transformation of a femur template shape (blue) in 2D using a regular grid as a deformation lattice to align it to a sample (beige).

The final part of the mapping function is surface projection. To increase the accuracy of the mapping process, the point will be projected on the samples surface. This step is necessary to model the individual patient specific rough surface which is not available in the smooth template. The surface projection maps the point X_T to the closest surface point on the sample. Given the distance transform of the sample $\Delta_S(x)$, the function $\text{surf}(x)$ can be expressed as owing to the fact that the gradient of the distance transform has unit length and points in direction of the surface normal of the closest point.

$$\text{surf}(x) := x - \Delta_S(x)\nabla\Delta_S(x) \tag{3.6}$$

Applied in composition, the single parts of the mapping function ($\text{affine}(x)$, $\text{deform}(\Theta, x)$ and $\text{surf}(x)$) transform a point from the template bone to a selected sample with increasing fidelity. $\text{affine}(x)$ accounts for the coarse alignment, $\text{deform}(\Theta, x)$ for the local deformation using a non-rigid method and $\text{surf}(x)$ for the remaining mismatch not captured by $\text{deform}(\Theta, x)$.

3.2.1 Correspondence Generation

The correspondence generation relies on the local deformation which is done by the deform(Θ, x) function. As it uses a lattice $\Theta := \{\Theta_{ijk}\}$ as the respective non-rigid transformation it has to be generated for every patient specific specimen first.

The optimal transformation is found following the approach from [HPM06] and [RSH+99]. By an optimization process which minimizes the distances between the template and a single sample bone a lattice is fitted. The minimization is calculated using the following energy term:

$$E_{data}(\Theta) = \int_{\Omega} (\Delta_T(x) - \Delta_S(\text{deform}(\Theta, x)))^2 dx \tag{3.7}$$

$$\text{with } \Delta := \mathbb{R}^3 \mapsto \mathbb{R}$$
$$\Delta(p) = \begin{cases} > 0 & \text{outside} \\ = 0 & \text{on surface} \\ < 0 & \text{inside} \end{cases} \tag{3.8}$$

In which Ω is the domain over which the expression is evaluated (the combined volume of the two bones with some additional padding), Θ is the parameter set encoding the displacement of the grid nodes, deform is the non-rigid transformation using the B-Spline lattice parameterized by Θ, and Δ_T and Δ_S are the distance transforms of sample and template, respectively. For a given point x, the distance transform of a surface yields the distance of x to the closest point on the surface. See definition 3.8 for this.

Such a distance function Δ was implemented using a regular grid structure to provide a volumetric signed distance field Δ for an embedded mesh. The described approach from [SGGM06] was used to get the distances and techniques from [BA02] contribute the required sign information.

By measuring the distance from a mapped point X_S to its nearest neighbor X'_S on the sample bone's surface an error term can be formulated. The error metric therefore penalizes deviations between the surfaces of the two shapes (and more generally, the iso-contours of the distance transform, as the sum ranges over the entire volume).

Using the distance function $\Delta_{S,T}(x)$ the error term is calculated on the GPU via a shader implementation of the error term for performance reasons, whereas

the lattice Θ and the distance functions $\Delta_{S,T}(x)$ are provided in the GPU memory as volumetric textures. It was necessary to provide the required performance, as the error evaluation has to be done iteratively within an optimization loop using the Conjugate Gradient Method (CG) to fit the lattice accordingly. Such an optimization algorithm requires the definition of a Jacobian to provide a direction hint which is commonly used in a gradient descent scheme. The analytical derivatives used are:

$$\begin{aligned}
\frac{\partial \Theta_{ijk}}{\partial x} &= \begin{cases} \begin{bmatrix} B_{l-i}(u)B_{m-j}(v)B_{n-k}(w) \\ 0 \\ 0 \end{bmatrix}, & 0 \leq l-i, m-j, n-k \leq 3 \\ 0 \in \mathbb{R}^3, & otherwise \end{cases} \\
\frac{\partial \Theta_{ijk}}{\partial y} &= \begin{cases} \begin{bmatrix} 0 \\ B_{l-i}(u)B_{m-j}(v)B_{n-k}(w) \\ 0 \end{bmatrix}, & 0 \leq l-i, m-j, n-k \leq 3 \\ 0 \in \mathbb{R}^3, & otherwise \end{cases} \\
\frac{\partial \Theta_{ijk}}{\partial z} &= \begin{cases} \begin{bmatrix} 0 \\ 0 \\ B_{l-i}(u)B_{m-j}(v)B_{n-k}(w) \end{bmatrix}, & 0 \leq l-i, m-j, n-k \leq 3 \\ 0 \in \mathbb{R}^3, & otherwise \end{cases}
\end{aligned} \tag{3.9}$$

Using the non-rigid transformation with the lattice Θ it is possible to get a continuous mapping for the whole bone surface.

3.2.2 Verification

For every single pelvis the correspondence information is stored within the database and is usable by the specifically developed software tools. This is also true for other bone types like femora. Such a mapping can be used to map points from a template bone to every other available patient specific pelvic bone. It is done via the mapping function map(x) (see equation 3.4). This mapping can be done automatically and will be used for the measurement evaluations. As it is an integral part of the data analysis it is important to know how accurate the point mapping is.

Validating the quality of a correspondent mapping is difficult, since no ground-

truth information is available (there is no verifiable "correct" mapping of a point location from the template to a sample). For this reason, manually determined point correspondences are regarded as gold standard [SRN+03]. The quality of the correspondent mapping achieved by the proposed system was validated through a study in which it was compared with correspondence points labelled manually by medically trained people.

For the preparation of the study, 10 salient reference points were marked on the femur template by a medical expert (see the red points on the blue template bone in figure 3.5). Then 10 femora were randomly chosen from the database (rendered in beige in fig. 3.5). However, samples with obvious pathological deformations were excluded.

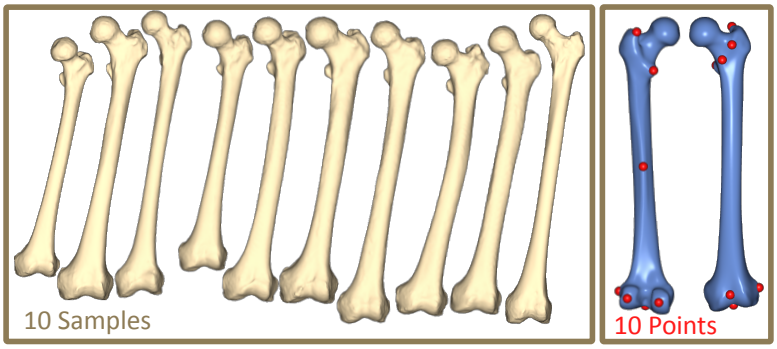

Figure 3.5: Test setup for the correspondence evaluation study.

For the actual study 12 medically trained subjects were given the image of the bone template with the previously marked points on it and then asked to identify the corresponding points on all 10 bone samples. To compensate for intra-subject variance, every participant performed the experiment a total of three times on a weekly schedule. Intra-subject variance turned out to be 2.4mm measured as the average over all root mean square errors calculated for each specific point triple.

Figure 3.6 displays the results of this study. The top row shows the points that were marked on the bone template and given as reference to the participants. The rows below display the distribution of the points marked by the subjects on the sample bones. In these the point to which the reference point was mapped by my algorithm is drawn in red, and the mean point of all manually marked points is drawn in blue. The smaller black dots indicate the individual points marked by the participants.

Table 3.1 shows the actual measured distances in mm for every sample point and patient's sample. Highlighted are points 2 and 10 whereas scaled up images are given in figure 3.6 for the 2 prominent points either on the left and right side.

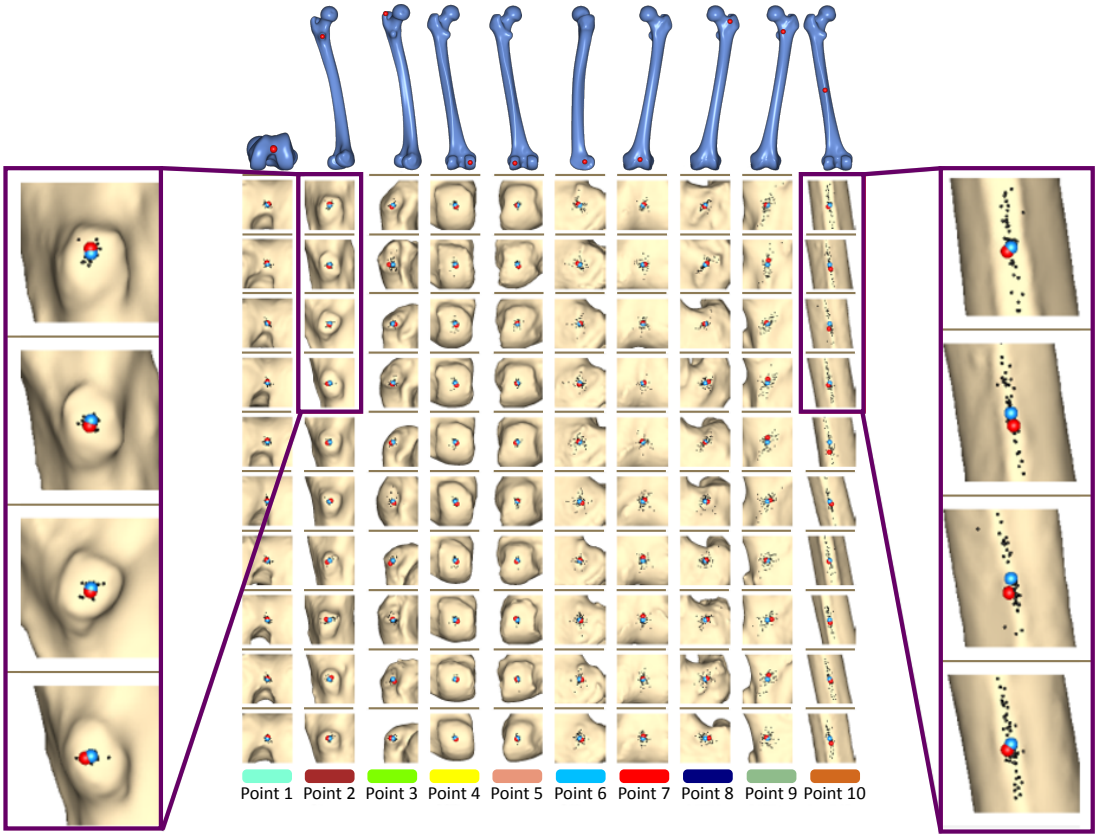

Figure 3.6: Overview of point clouds for every specimen and test point.

	Point 1[mm]	Point 2	Point 3	Point 4	Point 5	Point 6	Point 7	Point 8	Point 9	Point 10
Sample 1	1,3	1,2	1,6	1,2	0,3	1,7	1,1	1,1	1,1	1,6
Sample 2	1,2	1,5	3,2	1,5	1,7	1,9	1,7	1,8	3,6	3,7
Sample 3	0,5	0,9	1,9	1,6	0,5	0,8	0,6	0,5	1,2	4,2
Sample 4	1,0	1,7	1,1	2,0	0,5	1,2	1,0	2,8	3,4	1,9
Sample 5	1,4	1,8	1,7	1,3	1,4	1,2	0,9	0,4	3,8	7,8
Sample 6	0,5	1,1	1,6	2,3	0,4	2,3	2,0	1,8	2,4	2,7
Sample 7	1,0	2,2	3,1	1,5	1,0	0,6	2,6	1,2	1,1	1,0
Sample 8	0,6	2,7	0,7	2,0	1,7	1,0	3,1	1,8	3,4	2,2
Sample 9	0,5	1,9	2,1	1,2	0,4	1,6	0,3	1,7	3,3	1,5
Sample 10	1,1	1,2	1,8	0,8	0,6	1,9	1,9	2,9	1,2	4,1
Average	0,9	1,6	1,9	1,6	0,8	1,4	1,5	1,6	2,5	3,1

Table 3.1: The algorithmic mapping error, grouped by point location. It's defined as the distance between the algorithmically mapped point and the mean of the manually marked points.

To further compare the differences of the mapping algorithm and the manually marked points by the medical experts the actual distances have been drawn as bar plots. Figure 3.7 shows the distances between the algorithmically mapped point and the mean of the manually marked points. Whereas fig. 3.8 displays

the corresponding root mean square (RMS) deviations of the manually marked points, which are a measure for the uncertainty with which corresponding points were identified (the values represent the RMS of the distances of the marked points from the mean point, for example the distances of the black dots from the blue point in fig. 3.6). As can be seen, the uncertainty varies somewhat with the location of the template point. The point with the highest locational variance is point 10, located on the femur shaft. In this case, there is a strong anisotropy in the distribution of the points: obviously, there is a larger uncertainty along the direction of the femoral shaft rather than orthogonal to it, since the ridge on which it is located ("Linea Aspera") possesses saliency only in the transversal, rather than sagittal, plane. Similar characteristics can be observed for point 9. Highly characteristic points like e.g. point 2 shows low locational variance (see fig. 3.6).

The distances for the manually marked points can be seen in plot 3.8 and have been defined using the root mean square (RMS) deviations. Whereas the algorithmic mapping error is shown in 3.7.

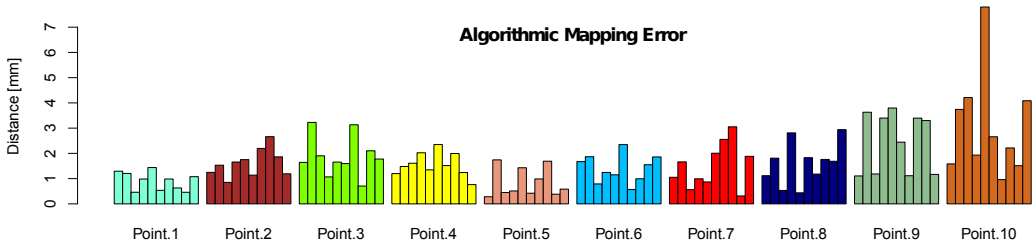

Figure 3.7: The algorithmic mapping error, grouped by point location. It's defined as the distance between the algorithmically mapped point and the mean of the manually marked points.

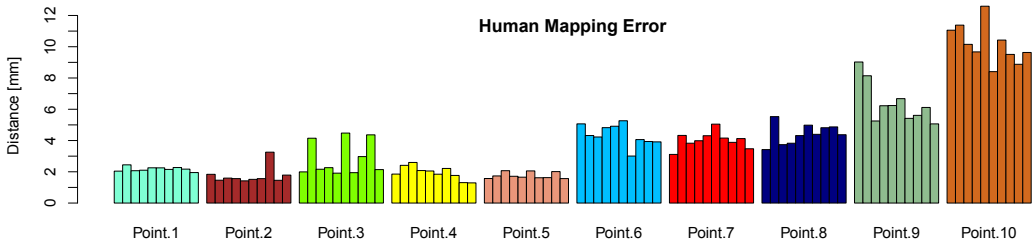

Figure 3.8: The human mapping error of the manually marked correspondences, grouped by point location. It's defined as the root mean square (RMS) deviations of the manually marked points.

Ideally, the red and the blue points would coincide on every sample, which

means that the algorithm and the human subjects (or rather, their average) agree exactly on where to place the corresponding points. As displayed in diagram 3.7, the actual distances range from 1 mm to 2 mm, which seems very satisfactory for the intended use.

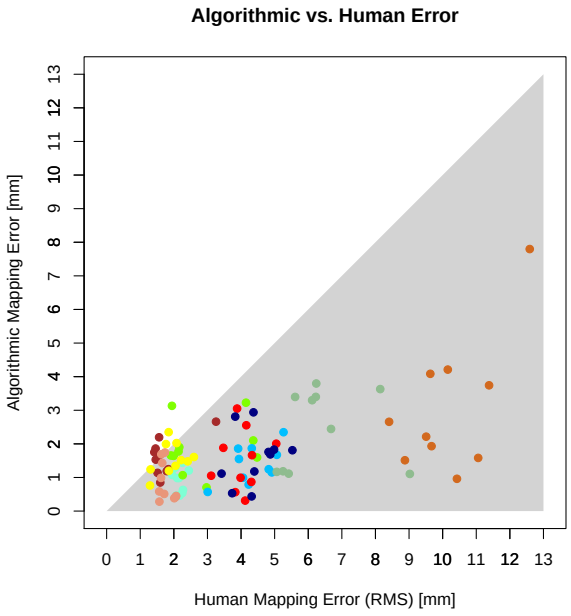

Figure 3.9: Comparison of mapping error and human error. The shaded error represents the region in which the human error exceeds the mapping error.

A natural way to assess the accuracy of the matching algorithm is to set the mapping error in relation to the RMS error of the manually marked points. Intuitively, a small RMS deviation but large mapping error would mean that the humans agree on where the point should be, but the algorithm places it apart. Likewise a large RMS error but small mapping error would mean that the humans have no clear notion where the point should be, but the algorithm places it near their average (our assumed gold standard) nevertheless. Figure 3.9 shows a combined plot of the two error values. Each point in the plot represents an unique (sample, template point) pairing, with the x axis denoting the human RMS error of this pairing and the y axis denoting its mapping error. The shaded area represents the region in which the human RMS error exceeds the mapping error. As can be seen, nearly all points lie inside this area. Informally, this can be stated as "uncertainty of the humans in finding point correspondences is higher than the mapping error of the algorithm", which we take to indicate that the algorithmically detected correspondences are closer to the "gold standard"'s position than those obtainable from an average human.

So it could be shown that the algorithmic mapping error is for almost all points smaller compared to points which have been mapped by medical experts. The study was published in detail in [SGR+14, GSR+10].

3.2.3 Mapping of measurements

In section 3.2 "Mapping" (see page 39) point correspondences were introduced which enable mapping functionality between the single bone samples, for the current work especially pelvic bones. The mapping data can be used to map a single point defined on a template pelvis to every other patient's sample registered in the database.

One can see that these geometrical entities and their given definitions depend solely on points and/or other given basic primitives. With the help of the correspondence information and the mapping algorithm it is now possible to map an entire construction which has been defined on a template bone by transferring the points to a patient's sample. By mapping the points and duplicating the graph G the construction can be transferred on every sample in the database.

A measurement defined on a template pelvis is mapped to a patient's sample pelvic bone by cloning the graph structure with all primitives and edges and mapping all the point primitives using the correspondence information of the database.

A template measurement on a template bone and formally defined via the graph G_T should now be mapped to a sample bone via the mapping information revealing the point correspondences to get a sample measurement G_S.

3.3 Conclusion

Within this chapter the actual usage and generation of the point correspondences have been presented. They enable the actual point mapping between a template and a single sample and therefore the transfer of the defined geometrical constructions. Further a survey was presented which proved the accuracy of such a mapping. It reveals that the human uncertainty of finding point correspondences is higher than the algorithmic error.

Along with the point correspondences the Mapped CAD System was presented and how it works using a graph. With the Mapped CAD System and the verified point correspondences it is possible to define and calculate the required pelvimetric measurements on the whole bone database in an efficient and reliable way to get correct and reproducible measurement results for a very large patient count.

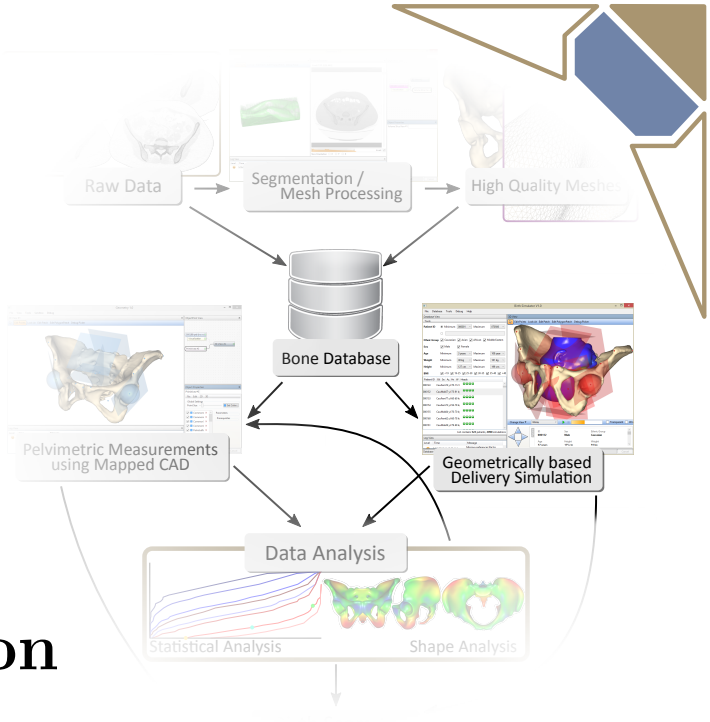

Chapter 4

Delivery Simulation

In the introductory section of chapter 1 a sequence of phases during a natural vaginal delivery was presented. The most important three phases among the five presented in fig. 1.1 on page 1 are Engagement, Internal Rotation and Extension. These phases describe the fetal position within the inner pelvis at different times on a trajectory during a vaginal delivery.

The current location of the fetal head along the birth trajectory which describes how far the baby's head has already traveled along its path is measured and monitored in obstetrics with the so called "Station" (see section 1.1.1 "Birth Mechanics" on page 2). It is in some way a relative distance value to the "Interspinal Plane" given in $\pm x$[mm]. So it is interesting to further investigate what happens to the baby within the inner pelvis during a vaginal delivery. To do that the simulation should generate objective and reproducible data which can be later used for finding possible indications for obstructed labor.

The delivery simulation takes a pelvis and a virtual baby head and calculates the head's trajectory within the inner pelvis. A trajectory represents the path through the inner pelvic bone represented by a sequence of discretized poses in 3D. At every evaluation point on that trajectory the head's rotation is determined describing the head's pose along that path. So it is possible for medical experts and especially gynaecologists to see which way a baby's head has to go and what rotation values occur for every single moment during the virtual delivery.

In figure 4.1 the simulation between the baby head and its counterpart - the pelvis - is shown schematically. The simulation takes a patient's pelvis from the bone database and a baby head model as its configuration and calculates the resulting birth trajectory. This path of the baby is drawn in green color. The green circles along the path represent the discretized evaluation points where

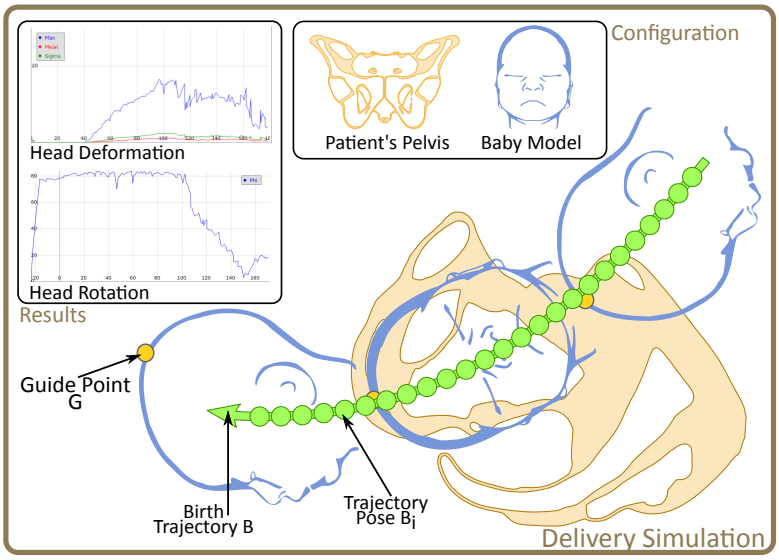

Figure 4.1: Overview of the delivery simulation using a baby's head model and a patient's pelvis.

the algorithm determines the optimal pose for the baby's head and its guide point G to reach the full extent of the available space and therefore minimizes the head's deformation. During the simulation the head's rotation and deformation is measured and recorded.

Before a 3D model of a pelvis can be used in the delivery simulation it has to be prepared in some way first. The sacrum's tip, called "Coccyx", and its local surroundings are made of no bony structure and are therefore in some way more flexible than other parts of the bone, as they consist of several small bones connected flexible to each other. So it is known that the coccyx will be pushed aside by the baby's head to provide more space in the lower part of the inner pelvis. During the pelvis mesh preparation the coccyx region will be identified and removed automatically. To do that a virtual op setup has been implemented. More on that is described in section 4.2.1 "Coccyx Removal".

After the coccyx has been removed, simulation specific landmarks for that individual pelvis have to be found which are used by the simulation algorithm. For example start-stop planes have to be determined as they represent the starting and termination criteria for the simulation (see section 4.2.2 "Simulation Landmarks").

From that starting plane the baby's head starts its journey through the inner pelvis. Using this plane an initial start pose B_0 has to be defined for the pelvis which is used to place the baby's head into that pelvis. An overview for the initial pose is given in section 4.3.2 "Initial Pose" (see page 67).

The mesh model of a baby head has to be prepared as well and - similar to the pelvis - landmarks are required. Also its coordinate system has to be standardized

to define a baby head model which consists of more information than just the mesh data alone. For collision detection and resolution between the pelvis and the head model a point set S is defined for the baby model. Such points $S_i \in S$ discretizes the head's surface as they are distributed equidistantly on the surface of the mesh.

In the real world babies differ in their individual sizes and weights. To simulate this more models have been generated and used for the delivery simulation. The different models are designed according to their size distribution. Section 4.3.1 "Baby Heads" presents the different babys' heads in more detail.

The algorithm calculating the simulation is explained more thoroughly in the following section.

4.1 Simulation Algorithm

To describe the simulation algorithm and how it calculates the resulting trajectory for the baby model through the inner pelvis (shown schematically in green color in fig. 4.1) the trajectory B can be defined formally as being a finite sequence of poses $B := (B_0, B_1 \dots B_l)$ with $B_i \in \mathbb{R}^{3\times4}$ of length l.

Using an initial pose B_0 the baby model will be placed and oriented accordingly to the patient's pelvic bone. This ensures that all babys' heads are located in a standardized and comparable start pose for all sample pelvises. The definition of the initial pose B_0 is given in detail in section 4.3.2 "Initial Pose".

At every step B_i of the trajectory B a pose optimization is performed to ensure that the baby head is aligned to have its maximal space within the pelvic cavity. The pose optimization is done using geometrical calculations and to determine a single pose B_{i+1} as the successor pose to B_i during a single iteration of the simulation loop.

The baby's head model used by the simulation algorithm starts from the initial pose B_0 to calculate the trajectory B. From that starting pose the other succeeding poses are calculated. As a pose like B_i has six degrees of freedom (6 DOF) - three translational and three rotational - the six parameters have to be determined during a pose optimization.

The six parameters of a pose B_{i+1} are determined from a pose B_i using the following iterative update scheme presented in algorithm 2.

First a normalized pull direction $\vec{p}$ (drawn in violet in fig. 4.2) is used, which is defined as one of the pelvis landmarks (see section 4.2.2 "Simulation Landmarks" for a definition). With this pull vector the baby head's guide point G will be

Algorithm 2 Delivery Simulation Algorithm

B_i ith pose in trajectory,
$G \in \mathbb{R}^3$ guide point, G_i guide point at B_i
$\vec{p} \in \mathbb{R}^3$ pull direction
Γ regular grid to approximate a plane at G_i and normal $\vec{p}$

$$T := \begin{cases} \mathbb{R}^3 & \mapsto \mathbb{R}^{3\times 4} \\ \vec{t} & \mapsto (I|\vec{t}) \end{cases} \text{ translates along a vector } \vec{t} \in \mathbb{R}^3,\ I \in \mathbb{R}^{3\times 3} \text{ Identity}$$

Calculate Trajectory T:

$G_i \leftarrow B_0 \cdot G$
while (G_i is above stop plane):
  $G_{i+1} \leftarrow T(\vec{p}) \cdot G_i$
  $\Gamma \leftarrow \textsc{Grid}(G_{i+1}, \vec{p})$
  $B_{i+1} \leftarrow \textsc{FindOptimalPose}(\Gamma, B_i)$
  $\textsc{DeformHead}(B_{i+1})$
  $G_i \leftarrow B_{i+1} \cdot G$

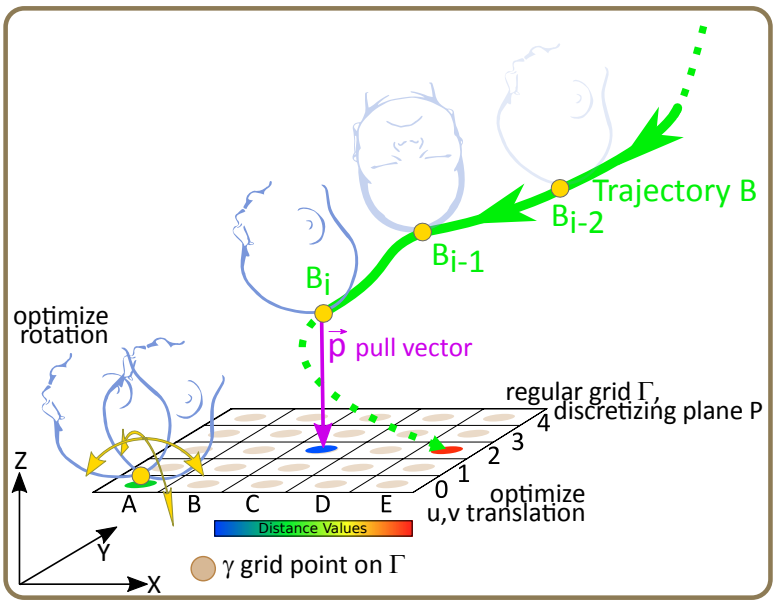

Figure 4.2: Schematic overview of the 6 DOF optimization. From a pose B_i the guide point G_i is moved along the pull direction $\vec{p}$ to define a grid Γ. It is used to optimize the remaining 5 DOF.

translated $T(\vec{p})$ along the pull direction and therefore out of the X/Y plane to define a point G_i.

The final pose B_{i+1} is determined by the pull vector $\vec{p}$ which pulls the guide point G downward with a magnitude of 1 mm and an optimization of the other five remaining parameters (2 translational and 3 rotational parameters) of the 6 DOFs. The optimization is presented in detail in figure 4.3 and the respective pseudo code is listed in algorithm 3 for function FindOptimalPose.

After the pose B_{i+1} has been determined the head shape can be deformed accordingly. This is done via the routine DEFORMHEAD. The details how it is done is presented in section 4.1.2 "Head Deformation".

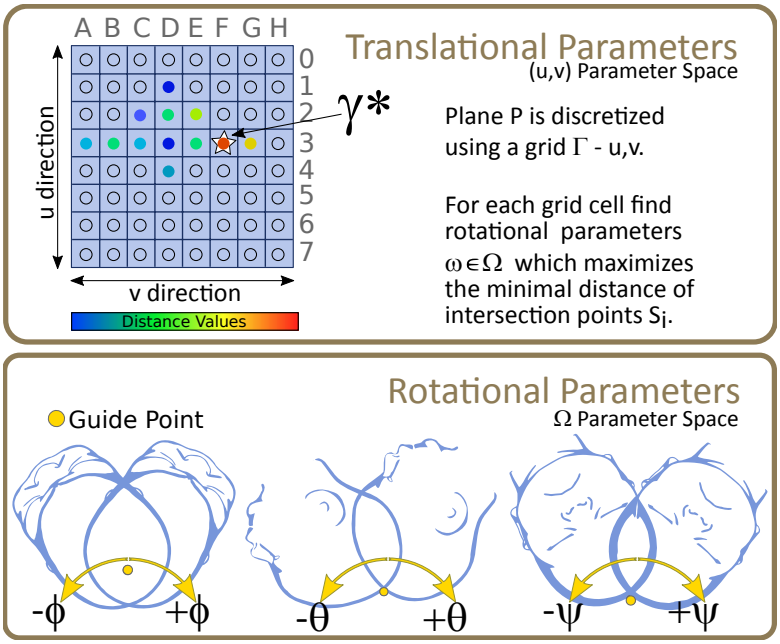

Figure 4.3: Schematic overview of the 5 DOF optimization using the regular grid Γ and angular search radius Ω to determine an optimal pose for the baby's head.

The five parameters $(u, v$ translation within a plane P and the three rotation values) together with the pull vector $\vec{p}$ indirectly defines the 6D parameter space. The parameters are optimized for every B_i to find the best pose which provides the head's maximal available space within the inner pelvis.

Plane $P := (G_i, \vec{p})$, defined by G_i and the pull direction vector $\vec{p}$, is discretized by a regular grid Γ with a cell size of 1 mm and an extent of 100 mm centered around the plane's base point G_i. So a 2D grid is defined ranging from $[-50\text{mm}; +50\text{mm}] \times [-50\text{mm}; +50\text{mm}]$. For every grid point $\gamma \in \Gamma$ an optimal rotation R_γ has to be found. This grid Γ is shown in illustration 4.3. The single grid points γ are drawn as circles.

Pose R_γ has the property as being that rotation which has the maximal value of the minimal distances for every grid point on Γ. The minimal distances are given by the points $S_i \in S$, defined on the baby's head, to any other point on the pelvis' surface. The points S_i are the equally distributed points on the head's surface which are used for collision detection between the pelvic shape and the baby. A more detailed overview of the used collision detection mechanism is given in the respective section 4.1.1 "Collision Detection".

The rotation R_γ calculated for every grid point γ is parameterized by $\omega :=$

Algorithm 3 Delivery Simulation Algorithm - FindOptimalPose

B_i ith pose in trajectory, $\vec{p} \in \mathbb{R}^3$ pull direction
Ω angular search radius
Γ a set of discretized points γ on a regular grid.

$$\varrho := \begin{cases} \Gamma & \mapsto \mathbb{R}^3 \times \mathbb{R} \\ \gamma & \mapsto (\omega, \delta) \end{cases} \text{ rotational parameters } \omega \text{ and minimal distance } \delta \text{ for every } \gamma$$

$$R := \begin{cases} \mathbb{R}^3 & \mapsto \mathbb{R}^{3\times3} \\ \omega & \mapsto R_z(\omega_\psi) \cdot R_y(\omega_\theta) \cdot R_x(\omega_\phi) \end{cases} \text{ rotation matrix for } \omega$$

FindOptimalPose(Γ, B_i):
1: **for each** $\gamma \in \Gamma$:
2: $\quad \varrho(\gamma) \leftarrow$ FindOptimalRotation(γ, Ω, B_i)

3: $\gamma^* \leftarrow \arg\max_{\gamma\in\Gamma}(\varrho(\gamma)_\delta)$
4: $\omega^* \leftarrow \varrho(\gamma^*)_\omega$
5: $B_{i+1} \leftarrow R(\omega^*) \cdot T(\gamma^*) \cdot T(\vec{p}) \cdot B_i$
6: **return** B_{i+1}

$(\phi, \theta, \psi) \in \Omega$ representing the three angular values - ϕ, θ and ψ - which encodes the rotation. A possible valid rotation R_γ can be found by testing all poses within a maximal angular search region which is given by $\Omega := [-\phi; +\phi] \times [-\theta; +\theta] \times [-\psi; +\psi]$. The search range is discretized in 32 steps for every dimension which led to an overall probe count of $32^3 = 32768$ evaluations for every grid point.

Rotational parameters ω are stored in a look-up table ϱ together with the minimal distance value δ. The minimal distance value δ is determined by applying the rotation R_γ to all points S_i during collision tests. Hence the look-up table ϱ stores for every grid point γ a tuple of ω and minimal distance δ.

A final maximum search over all grid points reveals the maximal value of the minimal distances (see line 3 in algorithm 3). The respective grid point which fulfills that criterion is now called γ^* and is drawn as the red circle with a white star-shaped background in figure 4.3 (see cell $F3$ in the given example).

Using the cell point γ^* as the position and $R(\omega^*)$ as the respective rotation it is possible to define the pose $B_1 := (R(\omega^*)|\gamma^*) \in \mathbb{R}^{3x4}$.

The described process is presented in algorithm 3 in pseudo code. It uses the function FindOptimalRotation which is defined in algorithm 4. This routine is implemented as a compute shader and is executed on the GPU. In section 4.1.1 “Collision Detection” the collision detection using the point set S is

explained.

Having B_1 as the successor pose of B_0 and repeating the described process all over again the pose B_2 and all other transitive successor poses B_{i+1} can be determined from the current pose B_i.

4.1.1 Collision Detection

While executing the routine FindOptimalRotation (see algorithm 4) which is invoked for every grid point γ, an optimal rotation pose R_γ is found (see line 2 in algorithm 3). The routine is executed on the GPU using its massive parallel architecture to test all possible poses and vote them accordingly to their resulting minimal distance values.

It is necessary that this routine is executed on the GPU because a lot of calculations have to be done to find the optimal rotation. The distance values of all points $S_i \in S$ as the voting criteria, are determined for all candidate poses which are tested during the processing time of FindOptimalRotation. By iterating the discretized angular search range Ω a respective candidate pose C_ω is defined and used for collision tests.

Algorithm 4 Delivery Simulation Algorithm - FindOptimalRotation

B_i ith pose in trajectory, $\vec{p} \in \mathbb{R}^3$ pull direction
Ω angular search radius
Γ a set of discretized points γ on a regular grid.
C_ω candidate pose for a grid point γ and rotational parameters ω
S a set of sample points S_i on baby head's surface for collision detection

FindOptimalRotation(γ, Ω, B_i):
    $\delta^* \leftarrow \infty$
    $\omega^* \leftarrow (0,0,0)^T$
    for each $\omega \in \Omega$:
        $C_\omega := R(\omega) \cdot T(\gamma) \cdot B_i$
        $\delta \leftarrow \min_{S_i \in S}(\Delta(C_\omega \cdot S_i))$
        if $(d < \delta^*)$: $\omega^*, \delta^* \leftarrow \omega, \delta$
    return (ω^*, δ^*)

To enable the routine to be executed on the GPU a simple collision detection mechanism has to be used. Here the baby's head is approximated using a point set S and a signed distance function $\Delta(X)$ (see definition 3.8 in chapter 3 "Mapped CAD System" on page 42) for the pelvis. Both the test points and the distance function can be used directly within a shader program as they can be loaded into

GPU's memory and are available as shader resources.

The head shape's surface is equidistantly sampled by points to define a set of test points $S := \{S_i\}$. The sampling is done once via geodesic distances during the baby head model generation. More information about that is given in section 4.3.3 "Collision Points". The set S is stored within the baby's head model. These points are used to test each candidate pose C_ω.

With the help of a distance function $\Delta(X)$ of the pelvis the point S_i can be tested whether it is inside ($\Delta(W \cdot S_i) < 0$) or outside ($\Delta(W \cdot S_i) \geq 0$). Points with negative distance values are classified as inside points and therefore the colliding points. C_ω is a resulting candidate pose dependent on $R(\omega)$:

$$C_\omega := R(\omega) \cdot T(\gamma) \cdot T(\vec{p}) \cdot B_i \quad \text{with} \quad R(\omega) := R_Z(\omega_\phi) \cdot R_Y(\omega_\theta) \cdot R_X(\omega_\psi)$$

The candidate pose C_ω is applied to all S_i and the distances are evaluated for them. The optimal rotation R_γ over the whole parametrization Ω has the minimal distance between the point set S and the pelvic bone.

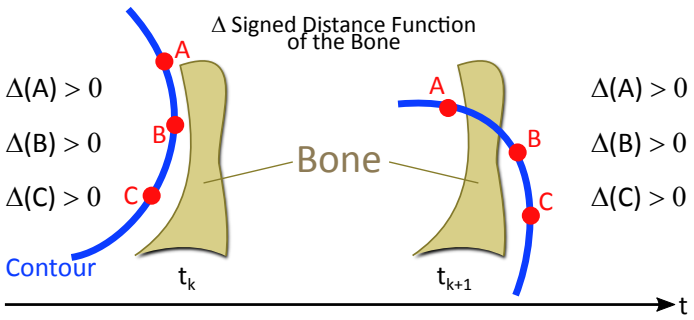

Figure 4.4: Schematic overview for collision detection. Thin bone structure makes the collision detection fragile.

While designing and developing the delivery simulation the first attempt of collision detection failed because the pelvic bone structure is very thin and the simulation was calculated in discrete time steps. Especially in the symphysis area or on both ilium parts the bone is less than a few millimeters thick and is therefore fragile for such collision tests. See overview 1.3 in chapter 1 on page 3 for the pelvic structures. While calculating the trajectory's pose B_{k+1} the points in S are lying on the right hand side of a bone structure in fig. 4.4 and are therefore classified as being outside and no collision has been detected. But in a previous time step k the points were on the left side of the bone structure. The distance function $\Delta(W \cdot S_i) > 0$ revealed positive values as well and so no collisions have been detected for both time steps k and $k + 1$.

The problem is that collision tests are done in a discrete setup and showed no collisions while in a continuous setting the points would have penetrated the

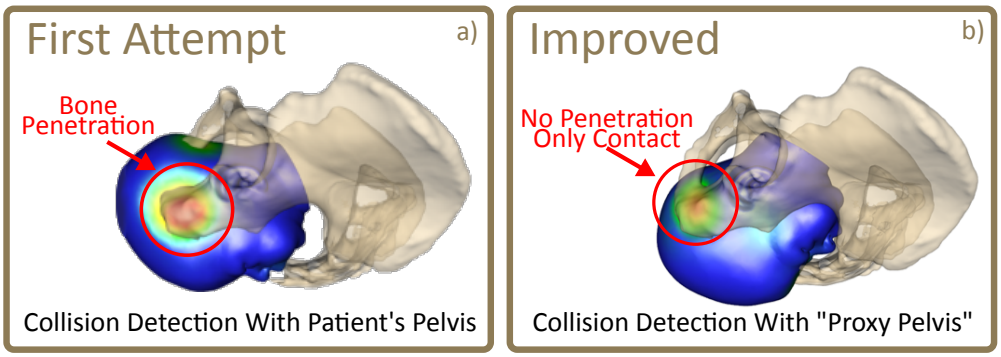

Figure 4.5: Collision Detection: In the first attempt (a) the baby head moves through the pelvic bone because of too thin bone structures. In the improved version (b) the simulation uses a proxy shape instead of the original patient's pelvis.

bone's surface. In rendering 4.5a this problem is presented. During the simulation the baby's head wanders through the pelvic structure because of the failed collision tests.

An approach to overcome this would be to reduce the step size but it would further increase processing time enormously. To avoid that and provide a more robust collision test another approach has to be used. One way to do this is to "thicken" the pelvic bone structure and use a "Proxy Shape" instead. Such a proxy shape has to be generated once for every patient's pelvis. The details for the proxy shape generation can be found in section 4.2.3 "Proxy Shape". The rendering in fig. 4.5b shows the same simulation setup using the respective proxy shape during collision tests instead. With the thicker bone structure the collision detection is more robust and the head does not penetrate the pelvis anymore.

Using all that the computationally expensive rotation search can be evaluated directly on the GPU using a robust and yet simple collision detection.

4.1.2 Head Deformation

After the successor pose B_{i+1} has been determined for a pose B_i the head deformation has to be calculated and stored in the simulation results. This is done via the HeadDeformation(T_{i+1}) call in the last line of algorithm 2 on page 52.

With the help of the new pose B_{i+1}, the pelvis' distance function $\Delta(X)$ and the point set S which approximates the surface of the baby's head, a subset of inner points $I := \{S_i | \Delta(C_\omega \cdot S_i) < 0\}$ can be identified. All the points in I lie inside the pelvic bone, penetrating the pelvis' surface and require a collision resolution. The resolution is done geometrically by a postprocessing step on the CPU before the

Algorithm 5 Head Deformation - B-Spline lattice Θ fitting

$S_i \in \mathbb{R}^3$ sample point on baby's head, non deformed, $S := \{S_i\}$ set of source points

$T_i \in \mathbb{R}^3$ sample points on baby's head, deformed and resolved, $T := \{T_i\}$ set of target points

B-Spline lattice $\Theta := \{\Theta_{ijk}\}$ as a set of displacement vectors $\Theta_{ijk} := (x, y, z)^T$ as it is defined in section 3.2.1 "Correspondence Generation".

A deformed source point S_i' is calculated from S_i using the deform function from definition 3.5:

$$S_i' = \text{deform}(\Theta, S_i) = S_i + \sum_{l,m,n=0}^{L-1,M-1,N-1} B_l(u)B_m(v)B_n(w)\Theta_{i+l,j+m,k+n}$$

To fit the lattice Θ an error term has to be defined and minimized. Such an error term measures the actual distance between the two point sets S and T for a candidate lattice Θ_C:

$$\text{Error}(\Theta_C, S, T) := \sum_{S_i \in S} \|S_i' - T_i\|^2 = \sum_{S_i \in S} \|\text{deform}(\Theta_C, S_i) - T_i\|^2$$

The minimization is done using the LMA algorithm (see section 3.2.1) and so a gradient of the Error term is required. The derivative in the spatial dimension x is:

$$\begin{aligned}
\frac{\partial}{\partial x}\text{Error}(\Theta_C, S, T) &:= \sum_{S_i \in S} \langle \frac{\partial}{\partial x} \|S_i' - T_i\|^2 \rangle \\
&= 2 \sum_{S_i \in S} (\langle \frac{\partial}{\partial x} S_i', S_i' \rangle - \langle \frac{\partial}{\partial x} S_i', T_i \rangle) \\
&= 2 \sum_{S_i \in S} \langle \frac{\partial}{\partial x} S_i', S_i' - T_i \rangle = 2 \sum_{S_i \in S} \langle \frac{\partial}{\partial x} \text{deform}(\Theta_C, S_i), S_i' - T_i \rangle \text{ for } x
\end{aligned}$$

Calculating the respective derivative how a displacement vector Θ_{ijk} influences the deform function leads to:

$$\begin{aligned}
\frac{\partial}{\partial x} S_i' = \frac{\partial}{\partial x}\text{deform}(\Theta_C, S_i) &= \sum_{l,m,n=0}^{L-1,M-1,N-1} B_l(u)B_m(v)B_n(w) \cdot (\frac{\partial}{\partial x}\Theta_{i+l,j+m,k+n}) \\
&= \sum_{l,m,n=0}^{L-1,M-1,N-1} B_l(u)B_m(v)B_n(w) \cdot \begin{pmatrix} 1 \\ 0 \\ 0 \end{pmatrix} = c \cdot \begin{pmatrix} 1 \\ 0 \\ 0 \end{pmatrix} \text{ with } c \in \mathbb{R} \\
&= \begin{pmatrix} c \\ 0 \\ 0 \end{pmatrix} \text{ for } x, \ \frac{\partial}{\partial y} S_i' = \begin{pmatrix} 0 \\ c \\ 0 \end{pmatrix} \text{ for } y \text{ and } \frac{\partial}{\partial z} S_i' = \begin{pmatrix} 0 \\ 0 \\ c \end{pmatrix} \text{ for } z
\end{aligned}$$

The single derivatives for x, y and z can be combined forming a vector $w := (c, c, c)^T$ to formulate the required gradient of the Error term for spatial dimensions x, y and z:

$$\frac{\partial}{\partial x, y, z}\text{Error}(\Theta_C, S, T) = 2 \sum_{S_i \in S} \langle w, S_i' - T_i \rangle = 2 \sum_{S_i \in S} \langle \begin{pmatrix} c \\ c \\ c \end{pmatrix}, S_i' - T_i \rangle$$

actual head deformation can be calculated. The inner points from I are examined and resolved to get a new set I' which represents the set of resolved inner points.

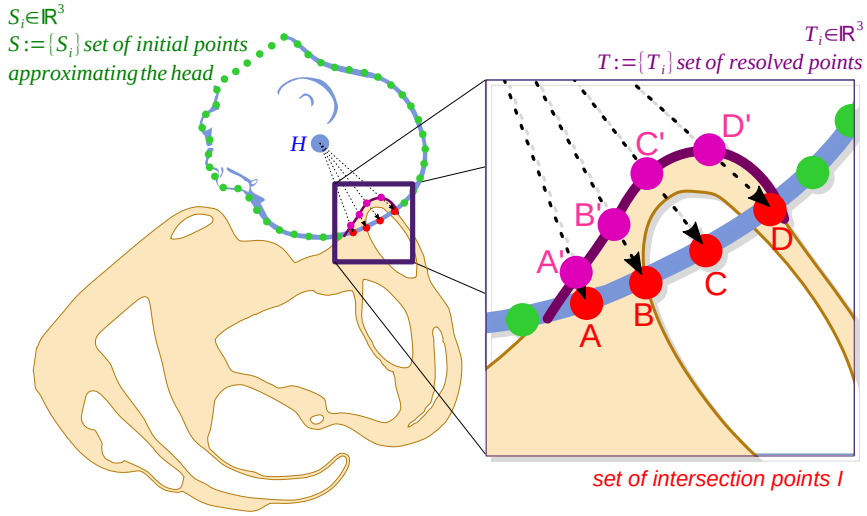

Figure 4.6: Schematic overview for geometrically based collision resolution.

The affected points $S_i \in I$ have to be processed separately. For every single point S_i a line can be defined from the head's geometrical center H: line S_iH.

As the point S_i lies inside the pelvic bone an intersection point Q exists between the line S_iH and the bone's surface. If more than one point Q exists the nearest point to $S_{i,k-1}$ - the point S_i at the previous evaluation (time step $k-1$) - will be chosen. After the collision resolution a point set T exists which includes the new positions for the points.

$$T := (S \setminus I) \cup I' \text{ with } I' := \{\text{resolve}(S_i) | S_i \in I\} \tag{4.1}$$

After collision detection and the following resolution two point sets S and T exist. By fitting a B-Spline lattice $\Theta := \{\Theta_{ijk}\}$ a non-rigid transformation function can be found to define a continuous deformation field which minimizes the distance for every point S_i to its corresponding point T_i.

The fitting of a lattice Θ is similar to the fitting of a lattice for the point correspondences which was presented in section 3.2.1 "Correspondence Generation" of chapter 3 "Mapped CAD System" on page 42. In contrast to that only the two sets S and T are used to fit the lattice Θ. The respective error term $\text{Error}(\Theta_C, S, T)$ and its gradient $\frac{\partial}{\partial x,y,z}\text{Error}(\Theta_C, S, T)$ which are required for the optimization is presented in algorithm 5. The evaluation of the error term is done on the GPU while the optimization loop of the Levenberg-Marquardt Algorithm (LMA) is executed on the CPU.

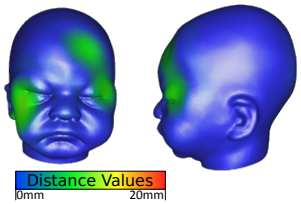

Figure 4.7: The deformed baby head is rendered using a heat-map to illustrate the current deformation values.

Using this continuous deformation given by the fitted B-Spline lattice Θ the baby head's mesh could be deformed by transforming all its vertices.

The actual distance value for a vertex $V_i \in V$ is defined the following way:

$$\text{displacement}(V_i) := \|\text{deform}(\Theta, V_i) - V_i)\| \tag{4.2}$$

Such a displacement value can be used along with a heat-map to illustrate the deformation values on the head shape in renderings. See figure 4.7 for an example. To do that the vertices V_i are augmented with a vertex color depending on the displacement value.

4.2 Pelvis Model

Before the actual simulation algorithm can be used to calculate the trajectory B for the baby's head the pelvic bone shape from the database has to be prepared first. This preparation is done by applying different steps which are done separately in successive order.

Figure 4.8: The pelvis preparation pipeline. The required steps to prepare a pelvis model to be used in the delivery simulation.

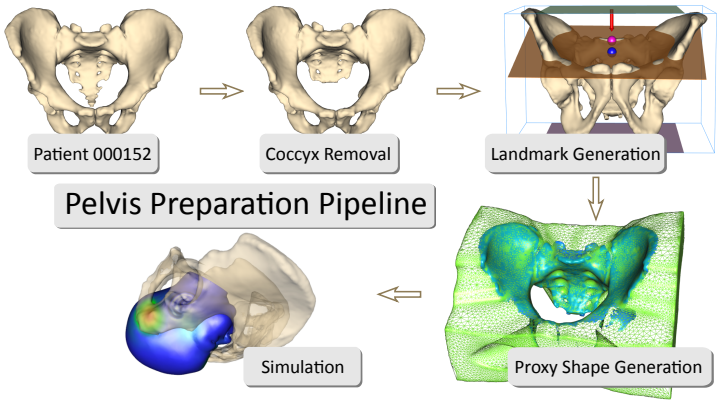

First the patient's sample pelvis has to be selected from the database. The next step performs a virtual op to change the geometrical shape to alter its mesh representation by removing the coccyx - the small part of the sacrum's tip which is so flexible as to be biomechanically neglected during a vaginal delivery. The start of the coccyx - related region has to be detected and the mesh will be changed by removing the selected part using boolean operations for shapes. This step as all the others of the pipeline are presented in figure 4.8.

After that the pelvic mesh has been truncated, the simulation related landmarks can be detected to find amongst others the required start and stop planes which are essential parameters of the simulation algorithm. The stop plane defines the termination criterion and therefore the last point on the resulting birth trajectory.

In the following step the changed pelvic mesh is used to compute the patient specific proxy shape for the pelvis which will be used during the collision tests between the baby's head and the pelvic bone. It is done in step "Proxy Shape Generation".

After the coccyx has been removed, the simulation features have been detected and the proxy shape has been generated, all required parts are available to define a pelvis model. Such a model is used for the actual simulation to calculate the birth trajectory.

4.2.1 Coccyx Removal

The rear part of a pelvis is called "Sacrum". The distal sacrum consists of several smaller bones as it has been presented in section 1.1 "Medical Background" (see page 3). The sacrum's tip is called "Coccyx". It is located on the lower tip of the vertebral column and is commonly referred to as the tail-bone. The coccyx consists of several small flexible bones connected to the sacrum via small joints.

During a natural vaginal delivery the baby displaces the coccyx to get more space within the inner pelvic cavity. As it is flexible it can be pushed beside by the baby head.

Therefore it has no real influence for a real delivery and is pushed away to gain more volume. The coccyx is not necessary for a virtual simulation and can be ignored. The coccyx will be removed from the initial patient specific mesh to define a new pelvis without the tail-bone which will be used during the delivery simulation.

Given an initial hint plane a mesh analysis can be done to find the narrowings on the sacrum's tip. The coccyx is located at the lower part of the sacrum. So a hint plane is defined by three points on a template pelvis. With the mapping function map(X) (see definition 3.4 in chapter 3 "Mapped CAD System" on page 33) the given three points were mapped onto the patient specific pelvis. Such an initial plane is drawn red in figure 4.9.

Shape contours are generated for the initial and the other planes within a search radius of 30 mm and their length are calculated to find the most narrow

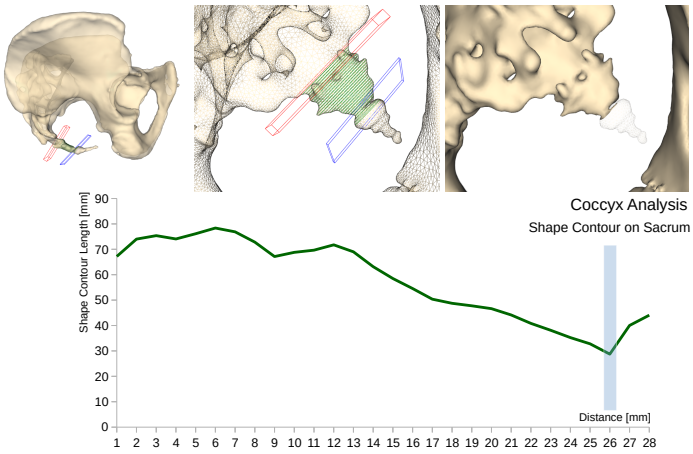

Figure 4.9: Removal of the coccyx: The required steps to remove the pelvic bone's flexible part on the distal sacrum.

region in the tail-bone's surroundings. The contour generation and the length calculation is described in more detail in section 4.3.1 "Baby Heads".

Once the plane with the minimal contour length has been found (the plane drawn in blue) it can be used to generate a box in 3D by extruding the plane. As this box is a triangulated mesh a difference operation between the box and the pelvic shape divides the two parts. The larger part is the pelvis without the coccyx.

In figure 4.9 the removal of the coccyx is presented showing a plot of the minimal contour length to identify the most narrow region where the coccyx' related region starts. Also the initial plane (drawn in red) and the final plane (in blue) are visible. The tested contours are drawn in green.

So after the coccyx is removed the pelvic mesh is prepared and available for further processing.

4.2.2 Simulation Landmarks

After the coccyx has been removed, the mesh is changed. As the simulation related landmarks depend on the changed mesh the features have to be detected afterwards. Such landmarks depend on the bounding box which is spanned by the directions of the anatomical coordinate system from the bone database. See section 2.6 "Shape Registration" on page 29 for more information about the anatomical coordinate system. The resulting simulation landmarks and the modified mesh are required parameters for the simulation algorithm and depend on the patient specific landmarks presented in section 2.5 "Landmark Detection" on page 27.

The simulation related landmarks are:

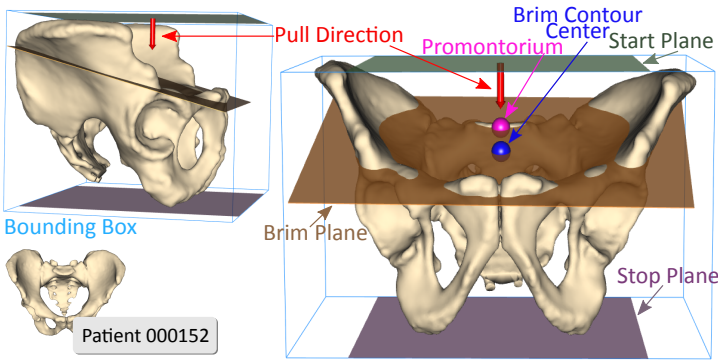

Figure 4.10: Simulation features defined as landmarks for every single patient's specimen.

- **Start Plane** The start plane, visualized in green in illustration 4.10, is located within the bounding box and touches the pelvic bone. It has the same normal as the bounding box' height dimension which is the inferior-superior direction in the anatomical coordinate system.
- **Stop Plane** Similarly the stop plane has been defined and touches the bottom of the pelvic bone. It is drawn in violet in figure 4.10.
- **Promontorium** The promontorium is the most ventral point of the proximal sacrum. It has been presented in the medical introduction given in section 1.1 "Medical Background" of chapter 1 (see fig. 1.3 on page 3). The promontorium has been labelled on the pelvic template and mapped to every patient specific sample.
- **Brim Plane** The Brim Plane P_{Brim} (shown in brown in figure 4.10) is defined as the best fit plane from a set of mapped points which are placed on the template's symphysis and the promontorium.
- **Brim Contour** Using the Brim Plane P_{Brim} the corresponding Brim Contour is defined as the inner closed path of the intersection of the Brim Plane and the inner pelvic surface.
- **Brim Center** The Brim Center C_{Brim} is the geometrical center point of the Brim Contour. It is drawn in blue.
- **Pull Direction** The pull direction $\vec{p}$, shown in green in picture 4.10, can be seen as a direction hint the baby's head will be pulled towards during the simulation process. It is used in the described simulation algorithm (see algorithm 2 on page 52).

4.2.3 Proxy Shape

The collision detection as described in section 4.1.1 “Collision Detection” on page 55, uses a point set S for the baby head and a proxy shape for the pelvis.

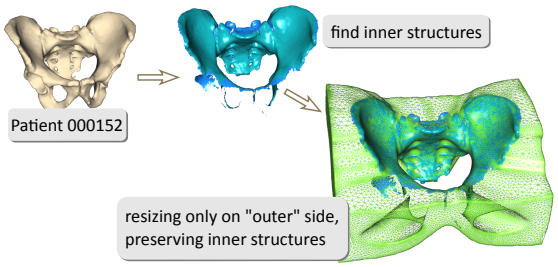

Figure 4.11: Pelvis thickening on the outer side to make collision detection more robust.

To generate a proxy shape some steps have to be performed. Figure 4.11 gives a schematic overview of how a proxy shape is generated for every patient’s pelvis.

First, the inner part of a pelvis, has to be found. It is important that the inner part stays in its original state as possible changes would alter the trajectory B and give entirely different simulation results.

Algorithm 6 Proxy Shape Generation Algorithm - CreateProxyShape

Pelvic mesh $M := (V, F)$, inner mesh $I := (V', F')$, F' set of selected inner faces
Γ volumetric grid enclosing the mesh M, γ single voxel of grid Γ
L_{Brim} line at C_{Brim}, proxy shape P

CreateProxyShape(M):

```
1:  I ← FindInnerStructure(M)
2:  for each γ ∈ Γ:
3:      C ← Center(γ)
4:      C' ← Project(L_Brim, C)
5:      L ← Line(C, C')
6:      Λ ← Intersect(I, L)
7:      α ← 0
8:      for each λ ∈ Λ:
9:          if (λ ∈ [0, 1]): α ← α + 1
10:     if (α = 0): Γ[γ] ← 1
11: P ← MarchingCubes(Γ, 0.5)
12: return P
```

Then the actual proxy shape can be generated using a voxelization approach. The pelvic mesh is embedded in a rectangular grid Γ structure of a given resolution. The respective algorithm is presented in algorithm 6. The grid discretizes the bounding box and has been initially expanded by 5 cm in every direction. For every voxel γ a line L is defined between the voxel center C and its projection C' onto L_{Brim}. If no intersections between the line segment L and the inner mesh I

Algorithm 7 Proxy Shape Generation Algorithm - FindInnerStructure

Pelvic mesh $M := (V, F)$, F' set of selected inner faces
inner mesh $I := (V', F')$, L_{Brim} line at C_{Brim}

FINDINNERSTRUCTURE(M):
  $F' \leftarrow \emptyset$
  for each $f_i \in F$:
    $C \leftarrow$ CENTROID(f_i)
    $C' \leftarrow$ PROJECT(L_{Brim}, C)
    $\vec{d} \leftarrow$ NORMALIZE($C - C'$)
    if ($< \vec{n_i}, \vec{d} > \leq 0$): ADD($F'$, f_i)
  $I \leftarrow$ SUBMESH(M, F')
  return I

has been found ($\alpha = 0$) the voxel will be classified as being an inside voxel and it is marked with 1 in line 10. Otherwise its marking will remain 0.

The inner structure F' and the resulting inner mesh I will be calculated via the function FINDINNERSTRUCTURE in line 1 of algorithm 6. Such a routine uses the simulation relevant landmarks from the previous section to identify the inner structure of the pelvis. The Brim Center C_{Brim} is the geometrical center of the Brim Contour. Together with the normal of the start plane C_{Brim} it defines a line L_{Brim}. It is located at the inner pelvis and is directing along the parturient canal.

The faces $f_i \in F$ of the pelvic mesh $M := (V, F)$ are classified as to whether they belong to the inner or outer part of the pelvis. This is done using the face normals $\vec{n_i} \in N$. A face's centroid C is projected onto the line L_{Brim} to get the point C'. By defining the direction $\vec{d} := C - C'$ a discriminant value is given by the dot product of the face normal $\vec{n_i}$ and the normalized direction vector $\vec{d}$. If the two directions are opposing the resulting sign value is negative and the face f_i belongs to the set of inner faces. Therefore it will be added to F', the set of inner faces. See algorithm 7 for this classification procedure. Figure 4.12 shows this schematically in 2D. A face f_0 (drawn in blue) is defined lying on the inner contour of the pelvic cavity. And a face f_1 (drawn in violet) is defined on the

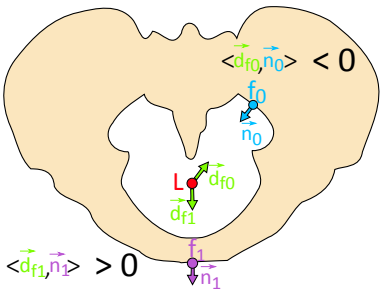

Figure 4.12: Identifying the inner structure of the pelvis in 2D.

outside. The brim's center line L_{Brim} is in 2D visualized as the red point L. The faces f_0, f_1 have their respective surface normals $\vec{n}_0$ and $\vec{n}_1$.

The actual proxy shape is extracted using the Marching Cubes Algorithm and an iso-value of 0.5 from the volumetric grid Γ. It can be processed further to produce a high quality mesh using the algorithms described in chapter 2 "Bone Database".

4.3 Baby Model

The simulation algorithm requires a patient specific pelvis and a baby's head model. During the simulation a baby moves through the inner pelvis. Such a model consists of a head shape, landmarks and collision points.

4.3.1 Baby Heads

Real babies differ in their sizes and weights. Some have a larger head than others. Measurements for the Fetal Pelvic Disproportion imply the head diameter is an important feature. But the head's circumference is important as well. The "Circumferentia fronto-occipilatis" (greatest head circumference) is measured between the most distal point of the head's back and its counterpart on the forehead called the "Glabella" between the eyebrows. A schematic overview of the described measurement of the head's circumference is given in figure 4.13. For a newborn it normally lies between 33 and 37 cm, with the mean at 35 cm. The range is given as $28 - 43$ cm according to [Deu10].

Using this data and knowing its range and distribution, the information can be used to define a set of different head models. An initial model is constructed from a CT scan of a training doll. The training doll for midwifes and gynaecologists represents a normal baby with a head circumference of 35 cm. It was CT-scanned and an iso-surface was extracted via the Marching Cubes Algorithm afterwards. The resulting mesh was then further processed to be simplified and remeshed. For this the same algorithms and techniques from section 2.3 "Shape Cleaning" on page 22 were used. The other head models can be generated via scaling from that initial shape.

The measurement of the head's circumference is approximated by a polygon's perimeter. The polygon can be calculated via the intersection of the mesh and a plane which has been defined on the initial mesh (see fig. 4.13). Using the same topology, like vertices, edges and faces, for the scaled mesh will not bring about a

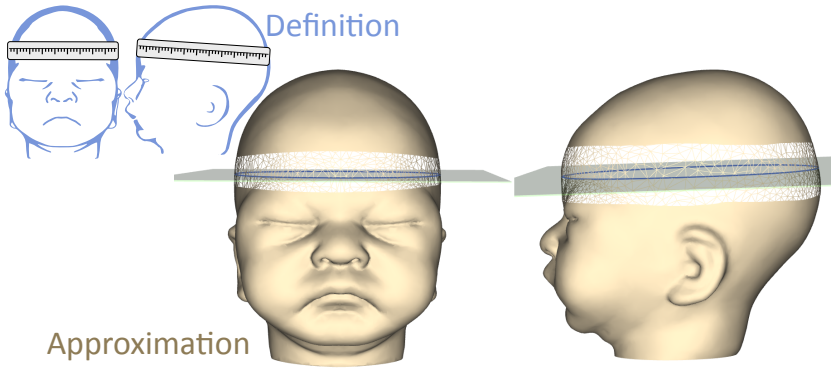

Figure 4.13: Definition of baby head's circumference and its approximation on the mesh.

change, as the affected edges and intersection points between an edge and plane for those edges are invariant of scaling. Every point has an intersection coefficient λ which encodes the position of the point along that edge. Using these λ values the head's circumference can be calculated by the same polygon. Its perimeter is determined by the sum of its linear sections.

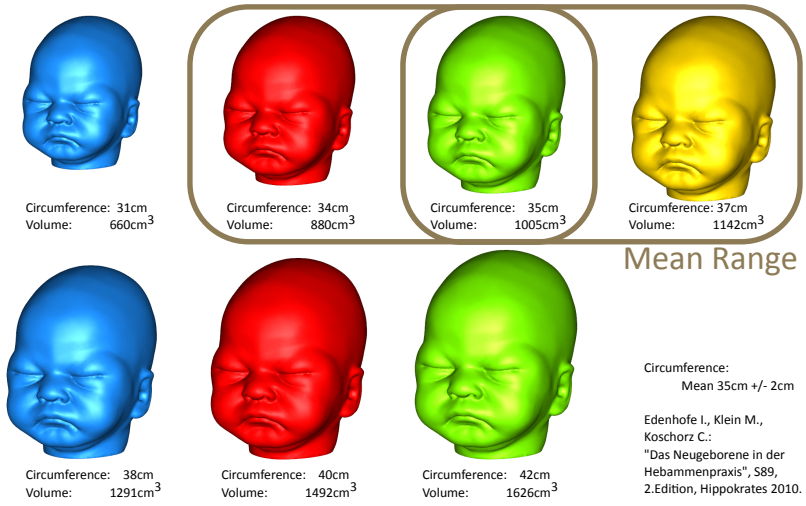

Figure 4.14: Available baby head shapes used for simulation.

Using this approach a set of baby's head meshes can be generated and provided for the simulation. The shapes of the head models which have been generated and used for every pelvic bone of the bone database are rendered in figure 4.14. The overview shows all baby's head models along with their respective properties such as their circumference and volume.

4.3.2 Initial Pose

After generating the scaled baby meshes, landmarks have to be provided and the coordinate system has to be standardized. As the topological configuration of a

mesh does not change on scaling, such landmarks can be defined on the initial mesh. With the help of the consistent mesh topology the identified landmarks can be transferred to the scaled babys' heads in a natural way.

The "Guide Point" G is an important landmark for a baby model. It is called this as it is the pivot point for all rotations which are performed during the simulation and guides the model along the trajectory B. This is done to simulate the natural behavior during a vaginal delivery where the baby's head leads the way for the newborn's body as it is described in the introductory section 1.1.3 "Fetal Head" on page 5. G is defined lying near the small fontanel and the highest point on the baby head's surface. An overview of the anatomy of the fetal head and its fontanels is given in figure 1.5 on page 5. The definition of G - drawn in yellow - is presented schematically in figure 4.15.

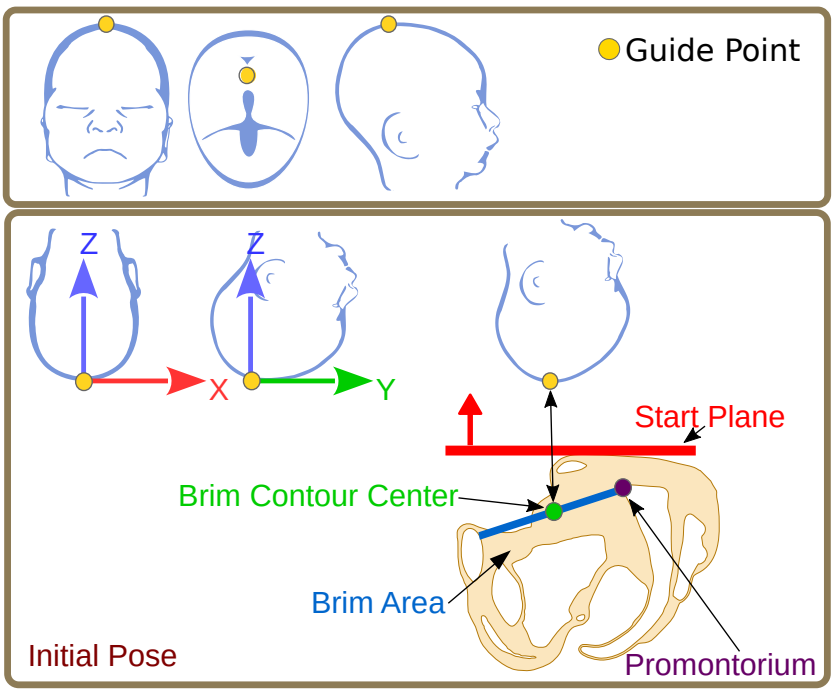

Figure 4.15: Definition of the initial pose B_0 of baby's head relative to the pelvis at delivery simulation's start.

Beside using G as the pivot point, it is also used as the origin of a standardized coordinate system having the coordinate values $(0, 0, 0)^T$. The mesh of the initial baby's head has been transformed accordingly to express all of its vertex information relatively.

The standardized coordinate system is now defined that Z axis originates from G and is pointing to the neck. The Y axis is perpendicular to Z and represents baby's viewing direction. Doing this results in defining the X direction to be pointing medial-lateral from the head's G toward the baby's left side.

Figure 4.15 presents also the standardized coordinate system having the yellow guide point G as the origin of the baby's head. The axis are defined the described way.

Using this definition of a coordinate system and the guide point G an initial pose B_0 can be defined for every patient as another landmark. The Brim Contour's center C_{Brim} gives an anchor point for the baby head's guide point G. B_0 can be defined to place the baby head's guide point G onto C_{Brim}. The Z axis of the standardized coordinate system should be collinear with the start plane's normal. The baby's viewing direction has to be set to point medial-posterior in the pelvis' anatomical coordinate system.

Using such an initial pose B_0 all of the babys' heads can be positioned on a starting position systematically and deterministically on every pelvic sample.

4.3.3 Collision Points

As the collision detection has to be performed during the pose optimization which is implemented in the shader program of the FindOptimalRotation routine (see algorithm 4 on page 55) collisions points have to be provided. Such points are used to implement a simple and efficient collision detection mechanism. All points $S_i \in S$ are tested for penetration of the patient's pelvis and are relocated during the collision resolution if necessary.

The collision points S are chosen to approximate the head's surface. As the vertices of the mesh are not distributed equidistantly on the mesh, the vertex positions cannot be used. For a collision detection it is important that no specific region of the head's surface is over- or undersampled. For a reliable collision test each region must be handled equally. To provide a better approximation than the vertices of the mesh, the points S_i have to be defined and are independent of the underlying mesh structure. By using an equidistant point distribution and with the help of geodesic distances the point set S can be defined in a way to ensure a regular and dense sampling of the head's surface.

Geodesics are a generalization of straight lines on curved surfaces to connect two points directly using the shortest path. For example the distance of two points on a sphere is given by the length of the shortest circle segment given by two points on that sphere. See [GHL04] for a more detailed introduction of geodesics. In figure 4.16a such a shortest distance between two points (A and B) on a sphere is illustrated.

Furthermore iso-circles exist on a sphere which represent all points having the

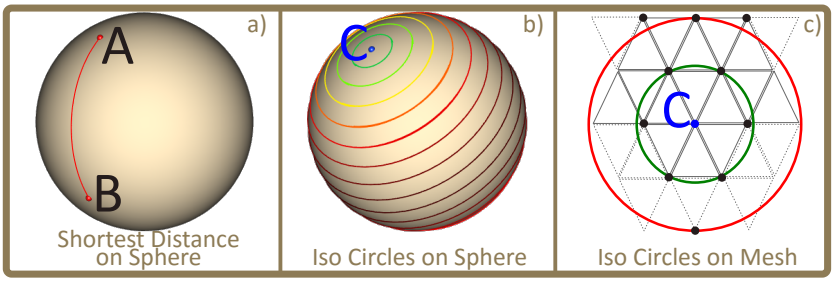

Figure 4.16: Usage of geodesic distances: Shortest path on a sphere (a), iso-circles on a sphere (b) and iso-circles on a regular mesh in 2D (c).

same distance from a given seed point C forming concentric circles. See fig. 4.16b for such an example. The different colored circles represent the iso-circles on that sample sphere. Each circle has a different distance from the seed point C - drawn in blue. All points are elements of a single circle having the same distance to C.

The concept of iso-circles can be transferred and generalized to triangulated meshes as it is presented in figure 4.16c showing a sample mesh in 2D with two iso-circles (drawn in green and red).

To calculate geodesic distances for an arbitrary mesh, algorithms like Fast Marching Algorithm (see [KS98, XZY10]) exist and have been implemented to generate the necessary geodesic distance function $\Delta_{geo}(X)$. The calculation starts from a seed point C and all distances are calculated relatively to C. Direct vertex neighbors N_i of C which are connected via an edge N_iC have their respective edge length $\|N_i - C\|$ as their distance values. From then on an iterative update scheme can be used and is described in more detail in [XZY10] to calculate the other distances via a breadth first sweep over the entire mesh.

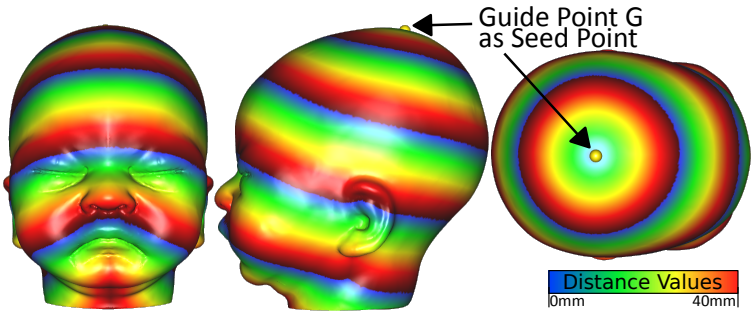

Figure 4.17: Renderings of the baby head with iso-circles from 3 different camera positions.

Once the distance function $\Delta_{geo}(X)$ has been calculated it can be used to render iso-circles on the baby head. The three different renderings of the baby head in figure 4.17 show the distance distribution on the head using a heat-map. The guide point G was chosen to be the seed point. And so the iso-circles represent the set of points which have the same distance to the guide point G.

To define the required collision points S_i and distribute them equidistantly on the baby head's surface the iso-circles have to be used. The points are selected, having a distance of $\delta = 5$ mm to their neighbors. The maximal count of available iso-circles for the head shape is given by:

$$M := \left\lceil \frac{\max_{V_i \in V} \Delta_{geo}(V_i)}{\delta} \right\rceil \tag{4.3}$$

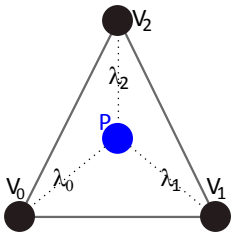

Figure 4.18: Point P expressed via bary-centric coordinates $(\lambda_0, \lambda_1, \lambda_2)$ within a face f_i.

By iterating all M iso-circles of a mesh - given by vertices V and faces F - the points will be distributed on the head's surface. The points on a single iso-circle are selected by finding all faces $f_i \in F$ which are part of that iso-circle and then using bary-centric coordinates to get the location of a single point within a face. A face f_i is intersected by the iso-circle if an edge of the face's edges exists that on edge's vertex e_0 has a lower, and e_1 has a greater, geodesic distance value than the iso-circle has. Bary-centric coordinates within a face are a triple $(\lambda_0, \lambda_1, \lambda_2)$ of weights which determines a point P within a face $f_i = (V_0, V_1, V_2)$ given by three vertices:

$$P := \lambda_0 V_0 + \lambda_1 V_1 + \lambda_2 V_2 \text{ with } \lambda_0, \lambda_1, \lambda_2 \geq 0 \ \wedge \ \lambda_0 + \lambda_1 + \lambda_2 = 1 \tag{4.4}$$

This results in a polygon for every iso-circle whose curve length can be resampled equidistantly.

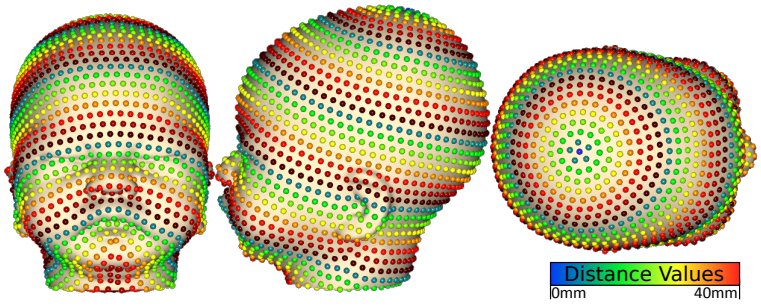

Figure 4.19: Equally distributed points on the baby's head model for collision detection using geodesics. The guide point G was used as the seed point.

Starting from guide point G the geodesic distances have been calculated and points have been distributed equidistantly on the head shape. The points have a distance of 5 mm to their direct neighbors. On the normal baby head with 35 cm head circumference, $2,092$ points have been placed on the head's mesh. The head and the points as part of the iso-circles can be seen in figure 4.19 from three different camera positions.

4.4 Conclusion

The chapter introduced the geometrically based delivery simulation. Figure 4.20 shows a small sequence of images of a simulation result which shows the rotational behavior during a vaginal delivery at three different stations as it is described in medical literature (see fig. 1.1 on page 1).

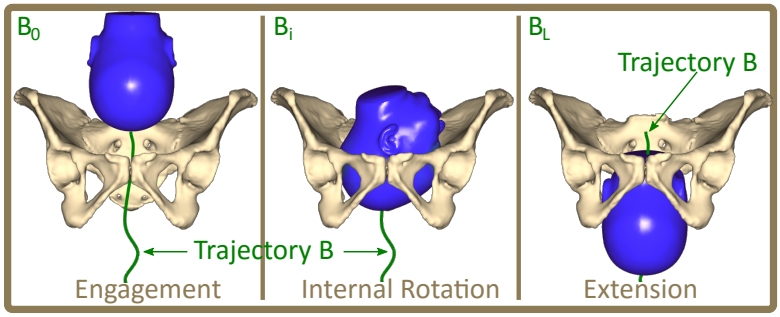

Figure 4.20: Simulation of the mean baby's head and a female pelvis and showing the rotational behavior during a vaginal delivery.

With the help of this simulation standardized baby heads were used along with patient pelvises from the database to calculate a birth trajectory B and record the head's rotation and deformation along the path.

The data structures used were presented as well as how the respective models have been generated for both the pelvis and the baby's head. A patient specific pelvis has to be prepared and then analyzed to derive relevant simulation features. Proxy shapes have been generated for each pelvis which are necessary and used for the collision detection.

The baby's head models have been created and prepared as well forming the resulting head model. A set of such baby's head models were generated to represent the size distribution for the baby's head as given in medical literature. Overall seven different head models were generated and used for the simulation.

The recorded data from that simulation can be used in later chapters to perform statistical analysis retrospectively and to define a "Birth Score" which can be used as labellings to describe how well a single pelvis has performed during the virtual delivery. Such labeling is required for the machine learning algorithms to generate a prediction model. The labels are used along with the pelvimetric measurements to define the training data the learning algorithms are working on.

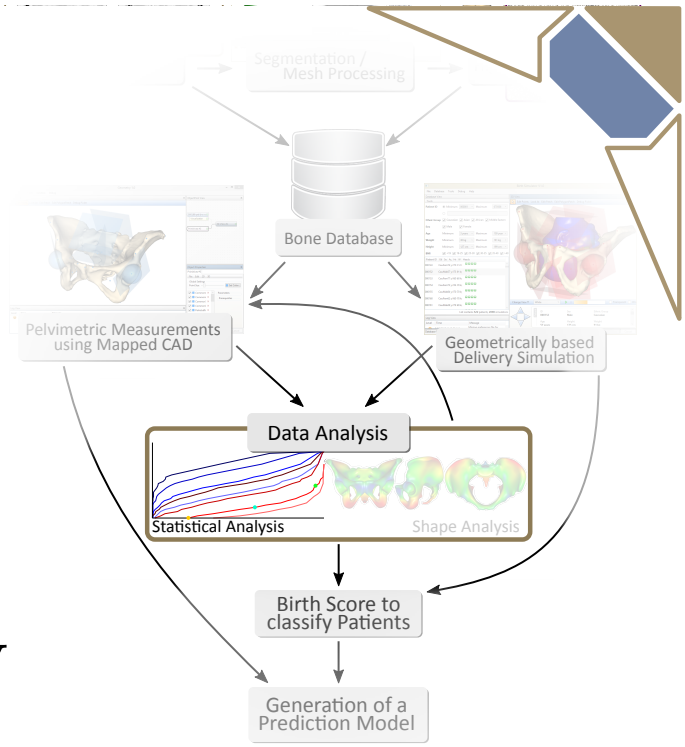

Chapter 5

Pelvimetric Survey

The aim of systems biology is to understand biological organisms and processes within an overall concept. To do that a biological phenomenon is examined and experimental data are collected and recorded. With the help of such experimental data mathematical models can be formulated. These models are the theoretical base for computer simulations which reproduce that phenomenon of interest. They help to examine the biological process in greater detail. In combination with experiments which are done in labs (in vitro) and virtually using the computer (in silicio) the mathematical models can be verified and iteratively adjusted to generate new knowledge. The described systematic approach is visualized in figure 5.1.

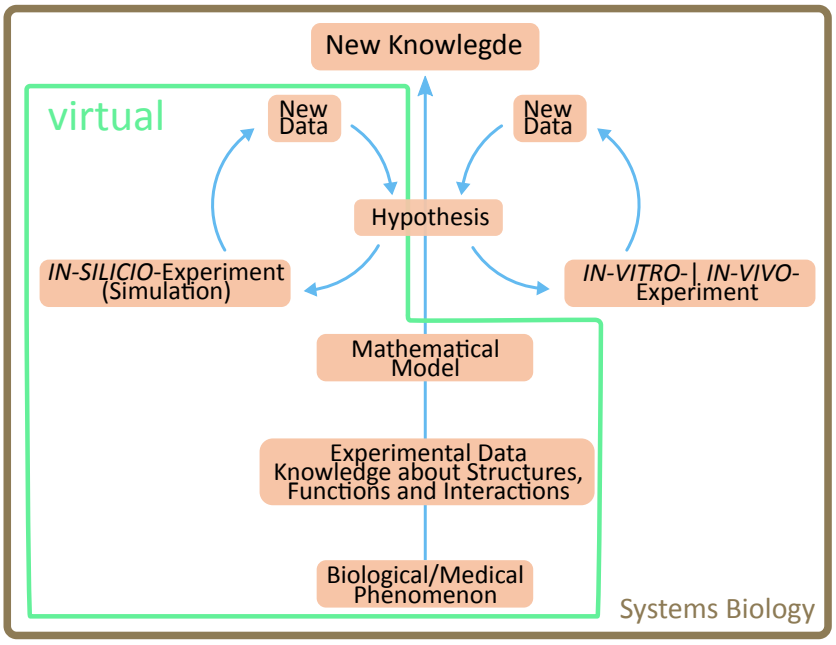

Figure 5.1: An overview of the systematic approach in systems biology.

In context of this thesis the phenomenon of obstructed labor is examined. The initial clinical data and pelvimetric measurements led to simple indices as FPI and Narrowings. From that the collected clinical data have been integrated into the presented bone database (see chapter 2 “Bone Database”). Pelvimetric measurements in 3D have been performed using the Mapped CAD System from chapter 3 “Mapped CAD System”. In parallel a geometrical based delivery simulation has been developed and used to gather more fundamental data about how well a specific and individual patient’s pelvis performs during a vaginal birth. The simulation and measurements are done virtually and represent the experiments in silicio within the systems biology’s approach.

The next step in such an approach is to derive a mathematical model from that experimental data which can be verified within the iterative process. To do that and derive a prediction model, the pelvimetric measurements and the simulated head deformations have to be combined to rate an individual pelvis according to its birth performance which is based on how it deforms the baby’s head model used along the birth trajectory during the delivery simulation.

So it is necessary to find an objective criterion based on the experimental data which allows a classification of the sample pelvis from the bone database. Such a criterion should be called “Birth Score”. Using that new criterion the pelvimetric measurements are statistically analyzed using the classification information to examine the two different classes - pelvises which perform well and pelvises which tend to have complications during a vaginal birth - separately. This helps to understand which measurements are predictive enough to describe the phenomenon more accurately, and measurements which are not, can be disregarded.

5.1 Birth Scoring

Classifying the pelvimetric measurements and then using this, the patient can be voted according to the measured attributes. But how to define an objective birth score using the experimental data? How to define mathematically what a “normal” or “problematic” delivery is? Medical literature does not reveal the required numbers or mathematical models which can answer such questions. But to define such a value, some statistical evaluations have been performed to define a birth score according to the measured head deformations which have been gathered with the help of the delivery simulation.

5.1.1 Definition of a Birth Score

To find a criterion which is descriptive enough for classifying the ability to bear a child, female and male pelvises are compared. Due to evolution and natural selection men are not built for giving birth in contrast to women and this fact should be reflected in the data. To determine these deformation values the male and female have been simulated with a number of different baby's head shapes. The deformation values of each baby model have been recorded and the maximal head deformations were used which occur along the birth trajectory. These values have been analyzed by representing them in a histogram.

To boost the fact that men are not evolutionarily selected for giving optimal birth to children, the results for larger baby models were analyzed as it is more likely to see differences in the data than using the smaller babys' head models.

For the baby model with the head circumference of 37 cm - representing the greatest standard head model which is in the normal range according to the obstetrical literature [Deu10] - the relevant values are presented in table 5.1. The respective histogram is plotted in 5.2.

	Total Patients	526	Female	206	Male	320
	Deform <= [mm]	Total	Female	Female [%]	Male	Male [%]
A	0	3	3	1,46	0	0,00
	1	11	10	4,85	1	0,31
	2	16	15	7,28	1	0,31
	3	31	30	14,56	1	0,31
	4	36	35	16,99	1	0,31
	5	48	47	22,82	1	0,31
	6	57	56	27,18	1	0,31
	7	68	66	32,04	2	0,63
	8	86	80	38,83	6	1,88
B	9	97	90	43,69	7	2,19
	10	113	105	50,97	8	2,50
	11	131	120	58,25	11	3,44
	12	152	136	66,02	16	5,00
	13	169	148	71,84	21	6,56
	14	180	154	74,76	26	8,13
C	15	194	161	78,16	33	10,31
	16	210	168	81,55	42	13,13
	17	233	177	85,92	56	17,50
	18	253	179	86,89	74	23,13
	19	272	186	90,29	86	26,88
	20	293	191	92,72	102	31,88
	25	404	199	96,60	204	63,75
	30	479	204	99,03	274	85,63
D	> 30	48	2	100,00	46	100,00

Table 5.1: An overview over the simulated deliveries and the head deformations using the standard baby model with 37 cm head circumference.

Row A in table 5.1 reveal that three patients have a maximal deformation

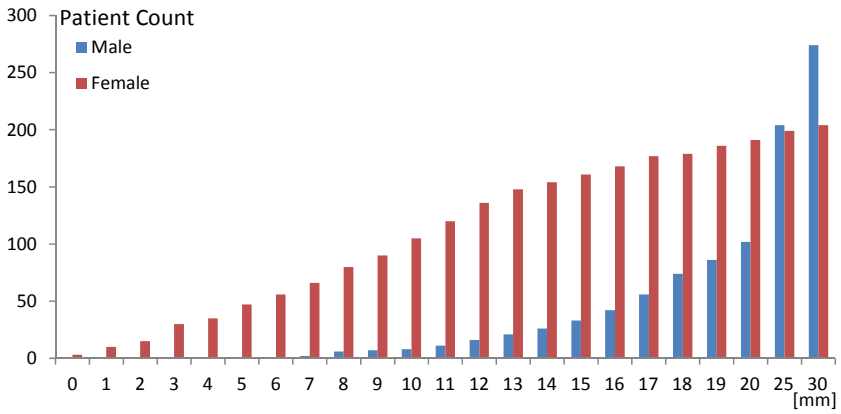

Figure 5.2: Plotted cumulative histogram of the patient count according to the head's deformation with a baby head circumference of 37 cm as presented in table 5.1.

value of 0 mm. All three patients are female and none of them are of male sex. That results in percent values of 1.46% for 206 female patients and 0% for 320 male patients.

A maximal deformation of 9 mm had 97 patients (see row B). From that count 90 are of female sex and the other 7 are male ones. These figures correspond to 43.7% for the females and 2.19% for the males.

The greatest difference between males and females is located at a deformation value of 15 mm in row C in table 5.1. The difference here is 128 patients from the 194 patients that have a maximal deformation of 15 mm whereas 161 are female and 33 are male.

Row D shows the figures for all patients which have a higher deformation than 30 mm. Only 2 females have a higher maximal deformation value and 46 male patients are affected.

The plot 5.3 presents the percent values from the given table as line plots. A violet line at 15 mm highlights the largest gap between the two lines.

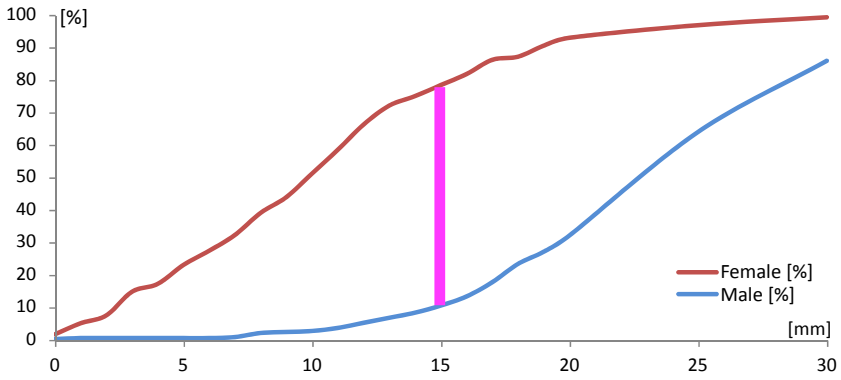

Figure 5.3: A plot of the patients count in [%] dependent on the head deformation values using the baby head with 37 cm head circumference.

To compare the maximal deformation values for the baby model with 37 cm head circumference to the standard baby model with a head circumference of

35 cm[1] a table has been generated (see table 5.2 - the complete table can be found in the appendix on page 131). Row C marks the figures for 15 mm deformation. It reveals that almost 95% of all females has lower deformation value than 15 mm, and all female patients show lower maximal head deformations than 30 mm (see row D).

	Total Patients	526	Female	206	Male	320
	Deform <= [mm]	Patients	Female	Female [%]	Male	Male [%]
	0	25	24	11,65	1	0,31
	14	287	193	93,69	94	29,38
C	15	311	194	94,17	117	36,56
	16	333	196	95,15	137	42,81
	30	515	206	100,00	308	96,25
D	> 30	12	0	100,00	12	100,00

Table 5.2: An excerpt over the simulated head deformations using the standard 35 cm baby model.

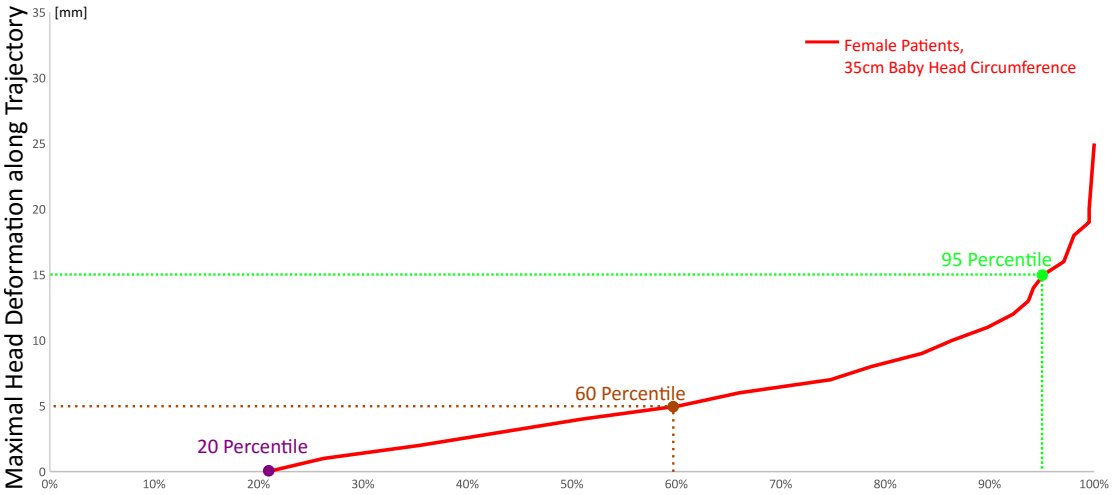

Figure 5.4: Percentile plot for female patients and the respective baby's head deformations.

The deformation value of 15 mm (see row *C* in table 5.2) reveals that almost 95% of all females have smaller head deformation values. According to statistics women with a deformation value of 15 mm or lower are in the 95th percentile. This is also shown in a percentile plot for the women and the standard baby model with the given head circumference of 35 cm. The 95th percentile is marked in fig. 5.4 with a green point. The 60th percentile is marked with an orange dot showing a deformation value of 5 mm. Therefore 60% of the women would deform the baby head at most 5 mm or lower. It is also interesting that the 20th percentile (marked

[1] The mean head circumference is 35 cm for baby heads (see section 4.3.1 "Baby Heads" on page 66).

with the violet point in fig. 5.4) represents only 1 mm or lower deformations.

From medical literature it is known that $6 - 7\%$ of the women are affected having a too narrow pelvis which can be problematic during a vaginal birth. This fact emphasizes more the use of a deformation value of 15 mm for a classification to generate adequate labels for the model fitting and classification in later chapters.

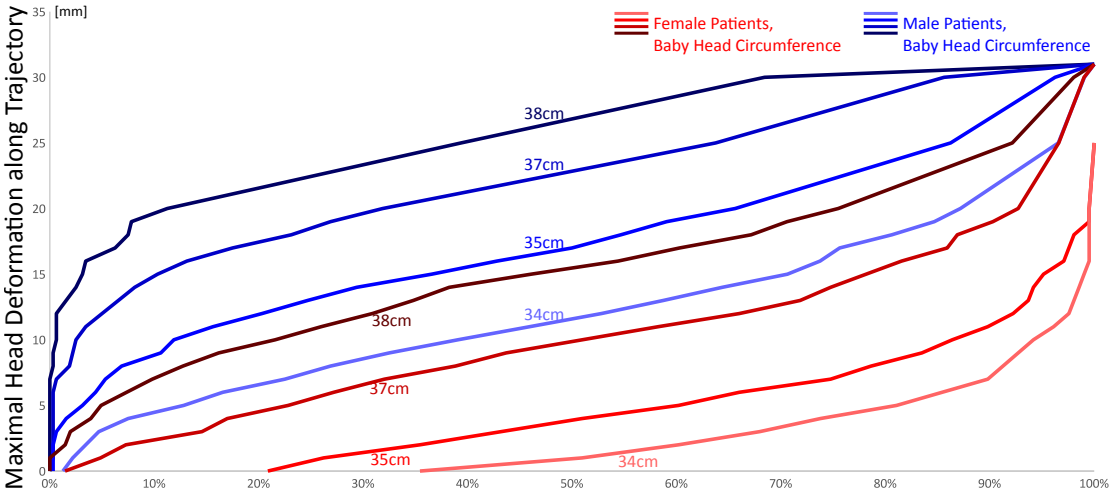

Figure 5.5: Percentile plot for male and female patients and their respective head deformations.

The percentile plots of all relevant baby head models are shown in diagram 5.5. The lines representing the percentile chart are generated for both, for male (blue lines) and female (red lines). For each sex the 3 relevant baby models - 34 cm, 35 cm and 37cm (see fig. 4.14 for an overview of all baby models on page 67) - and the baby model with 38 cm circumference were used and plotted. The 38 cm model is not part of the normal range and therefore leads to higher deformation values. It can also seen that the female related curves look similar to an exponential curve whereas the curves for the male ones look more like a root curve.

As there have been no criteria defined in the medical literature to describe the ability of bearing a child the maximal head deformation of 15 mm could be a possible way in the present status of medical knowledge to classify the pelvises and provide labeling information for the actual prediction model generation.

5.1.2 Compared to Other Indices

In the previous section a birth score was defined. According to the statistical analysis of the head deformations a value of 15 mm was defined to classify how well a pelvis will perform during a vaginal delivery of a standard baby model of

35 cm head circumference. Using this definition the 95th percentile of the women fulfill this requirement.

In the introductory part (see section 1.2 “Pelvimetric Measurements” on page 6 in chapter 1 “Introduction”) models and measurements from the literature were presented and it was explained how they are used to classify the pelvis and are the basis for a risk analysis. But, as already mentioned, they are discussed controversially (see [FND+98] for the Fetal Pelvic Index).

Nevertheless the defined birth score should be compared according to the Fetal Pelvic Index (FPI) - described in section 1.2.2 “Fetal Pelvic Index” - and the criteria which are used to identify Pelvic Narrowings from section 1.2.1 “Pelvic Narrowing”.

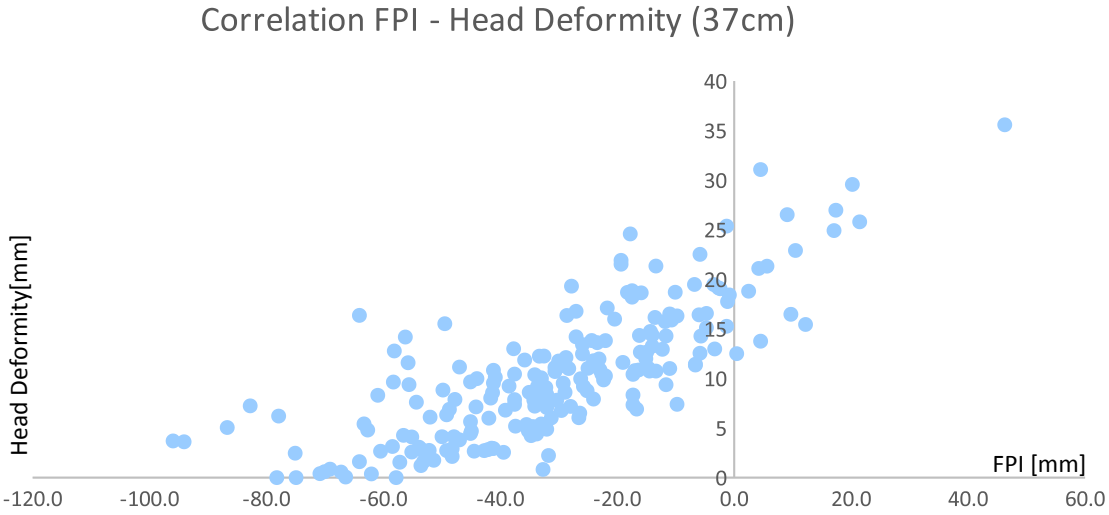

Figure 5.6: Correlation plots showing the relationship between the deformation values of the baby’s head and the FPI.

All female pelvises are used for the survey and the required measurements are performed using the Mapped CAD System (see chapter 3 on page 33). With this setup all 206 female pelvises from the bone database are processed to reveal the required values. As it can be seen for both types - FPI and Narrowings - 7% of the female pelvises are classified as being problematic and they are the same patients which have higher head deformation values.

To investigate this further diagrams 5.6 and 5.7 show correlation plots which indicate the relationship between the baby head’s deformation and the FPI and Narrowings from the medical literature. An overview of a correlation analysis and the definition of the correlation coefficient is given in section 5.3.2 “Correlation”.

Diagram 5.6 plots the relation for the FPI and the deformation values of the

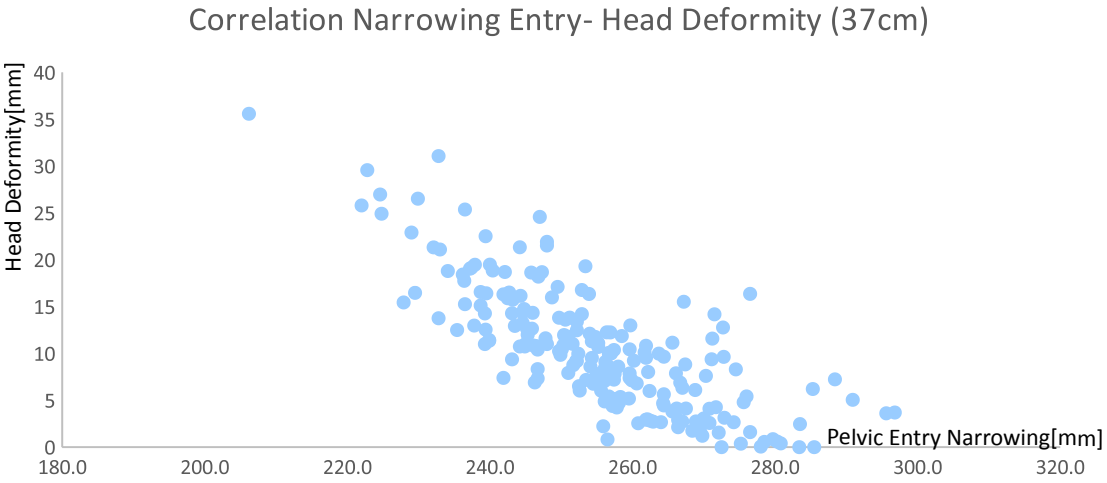

Figure 5.7: Correlation plots showing the relationship between the deformation values of the baby's head and Narrowings.

baby's head whereas diagram 5.7 presents the relation of the Pelvic Narrowings and the deformation values of the baby's head. The correlation coefficient is 0.78 for the FPI and -0.78 for the Pelvic Narrowings.

5.2 New Measurements

The pelvimetry as introduced in section 1.2 "Pelvimetric Measurements" defines various measurements to derive indications for example the Fetal Pelvic Index (FPI) or the Pelvic Narrowings in the entry, middle or exit sections of the pelvis. Such indices can be used to predict obstructed labor.

Beside those measurements proposed and described in medical literature refinements of already existing and new measurements are possible and can be defined and used for the evaluations.

5.2.1 Refinements

The measurements' definitions are of simple nature and quantify diameters and distances. Circumferences are approximated for example and can now be calculated directly in higher accuracy in 3D using the Mapped CAD System.

Among others there is an approximation of the geodesic length of the sacrum defined in the list of suggested measurements as they are defined in [MWW02].

This approximation is calculated by three points on the sacrum and the sum of the piecewise point distances.

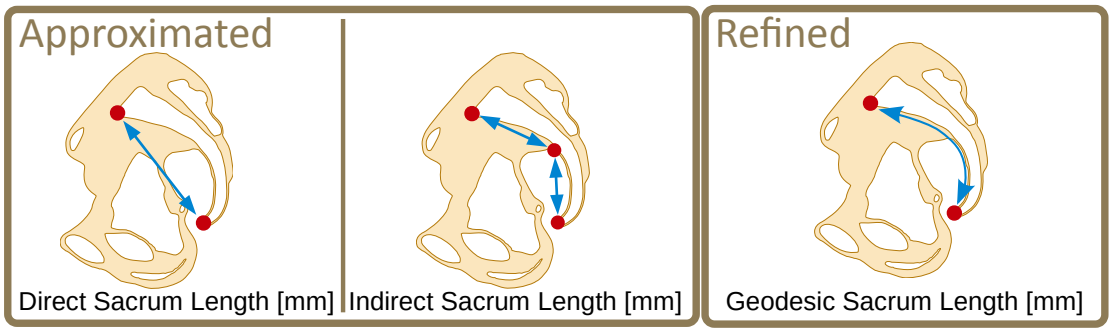

Figure 5.8: Different measurements to measure distance values on the sacrum.

Using the geodesic distances a more precise value can be derived. Figure 5.8 compares the two defined measurements "Direct Sacrum Length" and "Indirect Sacrum Length" with using the new geodesic distances.

By fitting a circle of such points on the sacrum a curvature value can be derived representing the bending of the sacral part of the pelvic bone. The curvature value is defined as being the reciprocal value of the radius. Greater values of such a radius will result in a low curvature value as the sacrum's bending is smaller. Figure 5.9 shows the pelvic bones representing the minimal and maximal radii.

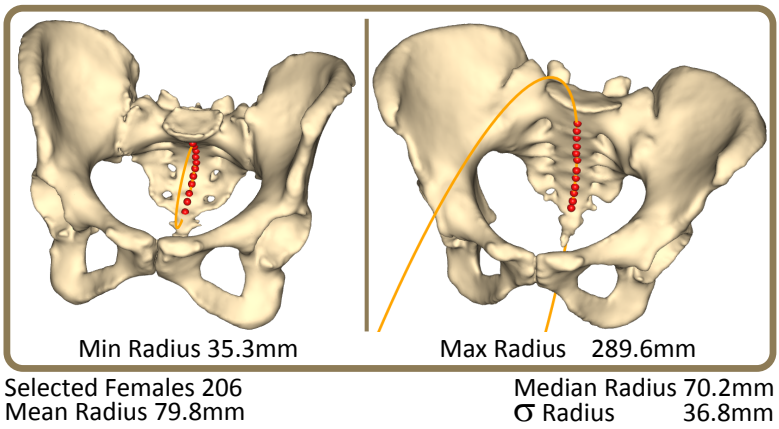

Figure 5.9: Fitted circles on the sacrum. Renderings of the female pelvic bones which represent the two extreme values.

With the help of the Mapped CAD System (see chapter 3) such calculations are possible and can be used for pelvimetric measurements in 3D.

5.2.2 Combined Measurements

Further, combinations of measurements are possible to boost their individual influence within the model. This means that a "BrimArea" measurement can be more predicative than just the two diameters alone. This is possible as it describes the area as a product of two factors instead of a linear combination of the two measurements. This technique helps to amplify the predictive power of a single measurement.

Other combined measurements are for example the "BrimRatio" or the "OutletArea". The second is defined as being the product of the "Tightness Conjugata" and the "Dist. Interspinalis". The "BrimRatio" is the ratio of the "Conjugata Vera Obstetrica" and the "Diameter Transversalis". A value of 1 reveals that the two diameters of the brim region have equal length and the pelvic entry looks more like a circular shape than an elliptical one. Such a pelvis is known as "Gynecoid" in the Caldwell-Moloy classification of pelvises as it has been introduced in figure 1.4 in section 1.1.2 "Pelvic Bone" on page 4. A value < 1 shows that the pelvis is wider than its anterior-posterior extent and is typical for a "Platypelloid" pelvis. "Anthropoid" pelvises have a brim ratio of > 1.

Similar to the other measurements, the combined ones have been defined on the template bone and used to measure the whole female pelvis population from the bone database. The measurements have been performed using the Mapped CAD System (see chapter 3).

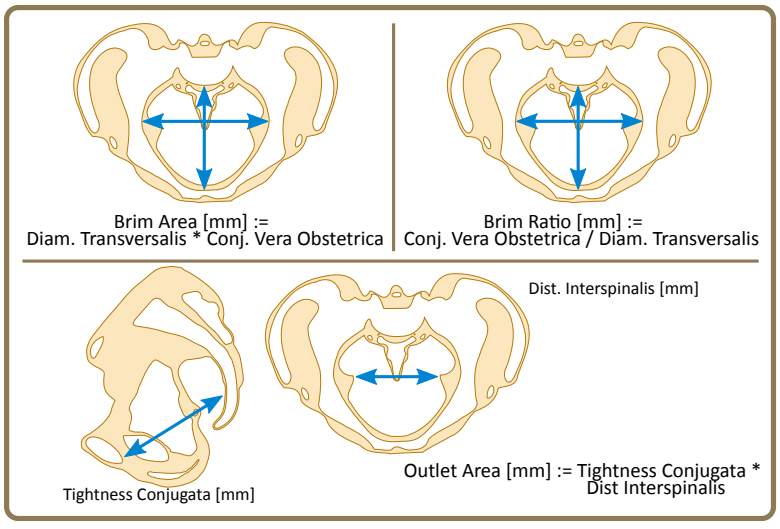

Figure 5.10: Overview and definition of the combined measurements.

An overview of the combined measurements and how they are defined is shown in figure 5.10.

Using the defined birth score from the previous section together with the pelvimetric results the measurements can be further evaluated using statistical methods. This is done in the following section (see section 5.3 “Pelvimetric Statistics”).

5.3 Pelvimetric Statistics

Once a definition for a birth score has been established, it can be used for the further statistical evaluations regarding the pelvimetric measurements. These measurements have been computed via the Mapped CAD System on all patients who have been integrated in the bone database.

The measurements’ results can now be combined with the birth score to classify how well the patients perform during the delivery simulation. This combination is necessary to compare the measurements according to their predictive power.

5.3.1 Statistical Evaluations

For every measurement a box plot and a density plot can be generated to analyze its statistical properties.

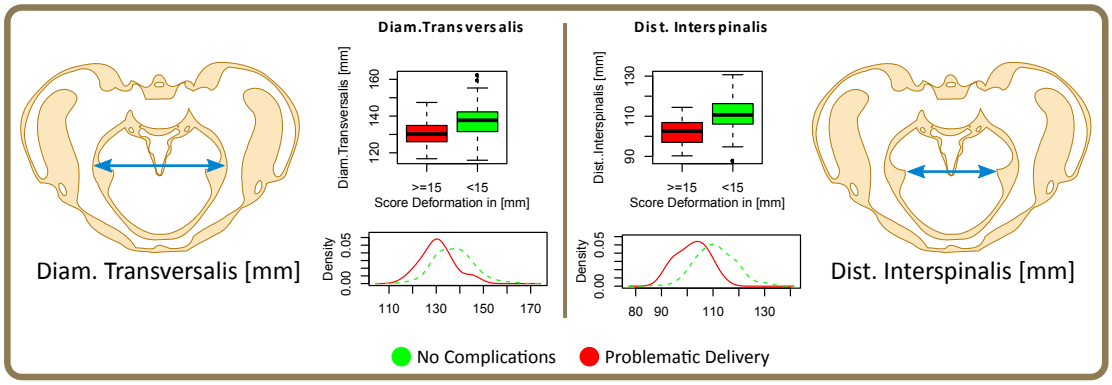

Figure 5.11: Single features from pelvimetric now classifiable using the birth score.

Figure 5.11 shows two of the measurements, namely the “Diameter Transversalis” and the “Dist. Interspinalis”. A schematic overview of these measurements is given on the far left and far right hand side. The “Diameter Transversalis” is presented on the left side followed horizontally by the respective box and density plot. On the right “Dist. Interspinalis” is schematically drawn along with its respective charts.

Using the birth score the patients can be partitioned into two sets shown in green and red. Green represents the females having a “good” birth score and red

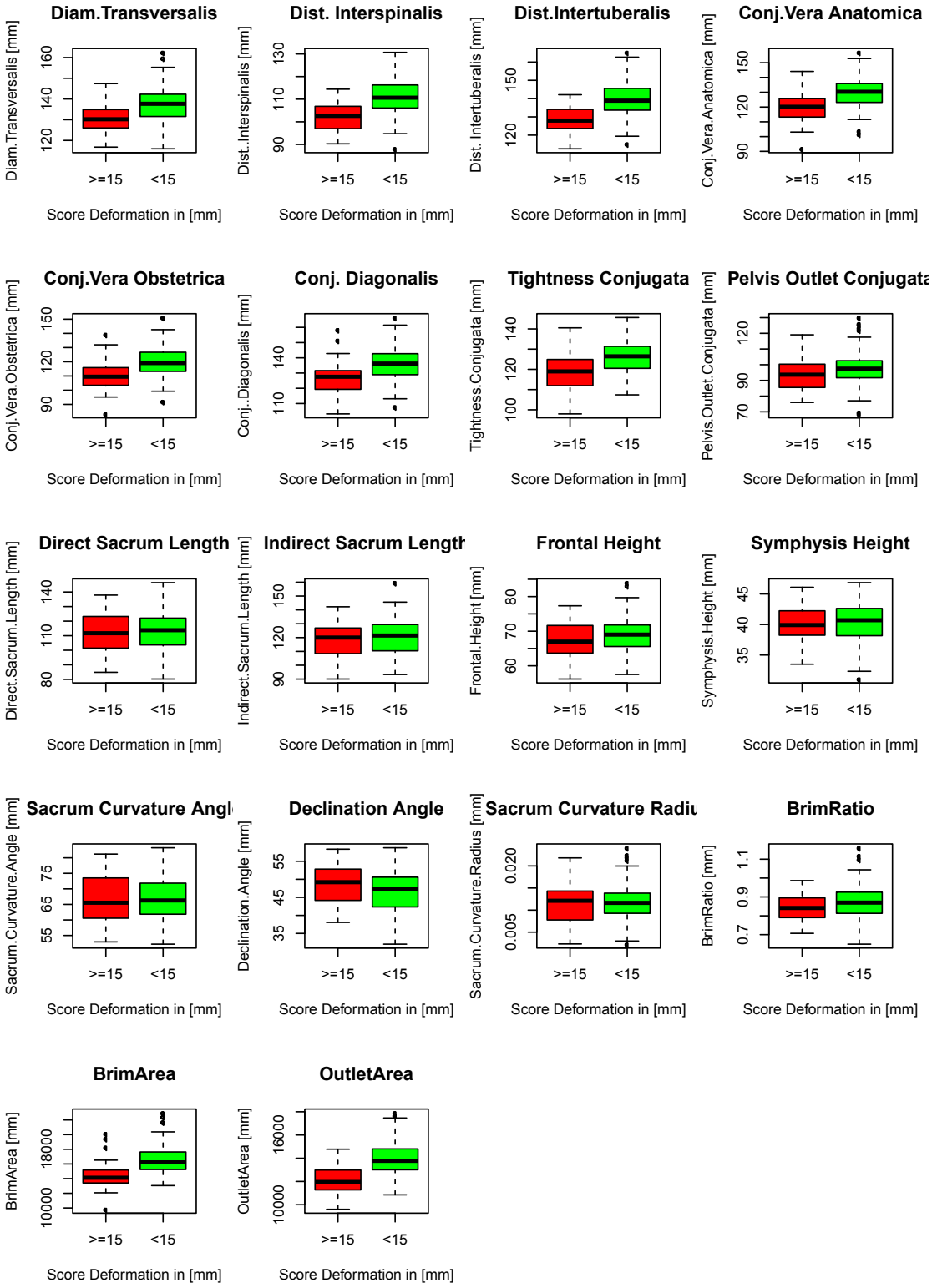

Figure 5.12: Box plots for the pelvimetric measurements.

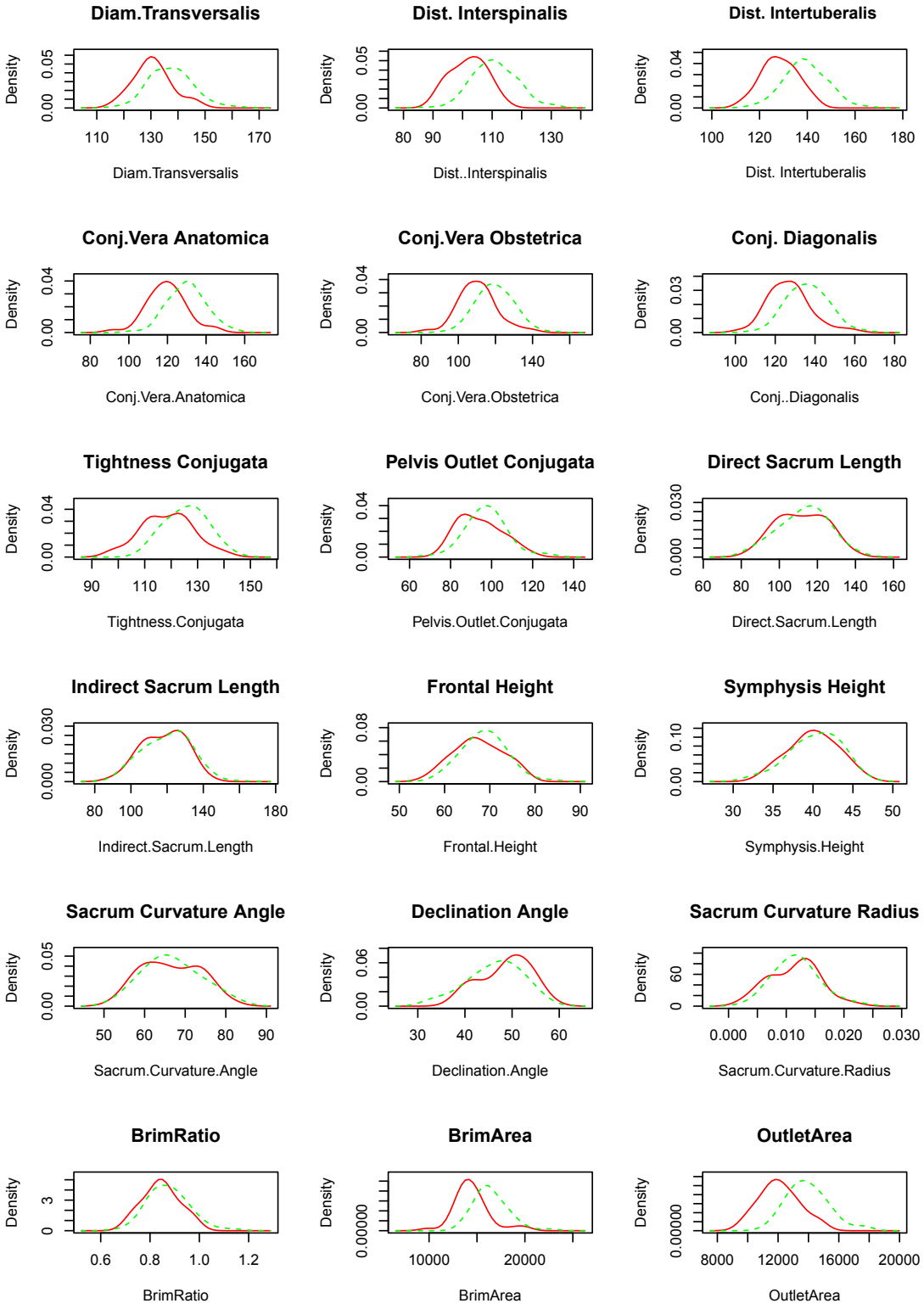

Figure 5.13: Density plots for the pelvimetric measurements.

for the remaining samples.

The box plot shows how significant the single measurement is to distinguish between the two subsets of the female samples. In addition the density plot shows how the measurements' distributions are for the two groups.

Figure 5.12 shows the box plots for the other standard measurements and figure 5.13 respectively the density plots. The definitions of the used 14 standard measurements are given in appendix A "Pelvimetric Measurements" on in figure A.3 page 128.

The combined measurements BrimArea, OutletArea and the BrimRatio have been evaluated as well as their respective plots and are also given in the figures 5.12 and 5.13. Also the sacrum curvature radius which has been described in section 5.2.1 "Refinements" has been evaluated and plotted.

More plots of statistical evaluations of the measurement results are given in the appendix A "Pelvimetric Measurements" on page 125.

5.3.2 Correlation

Correlation analysis gives a first insight into how a measurement correlates to others. Are they dependent or do they provide further information? If two measurements correlate to one another, they do not provide further information for a possible prediction model. So this is in some way redundant and can therefore be disregarded.

Two measurements are correlated when their respective correlation coefficient has the following property $0.6 \leq |c| < 1$. Values $|c| > 0.7$ show a strong linear relationship between the two measurements [Lin07].

The correlation coefficient c for two measurements X and Y is dependent on the covariance and the two standard errors σ_X and σ_Y. It can derived by:

$$c := \frac{Cov(X,Y)}{\sigma_X \sigma_Y} \tag{5.1}$$

And the covariance of the two measurements X and Y is dependent on the respective mean values $\bar{X}$ and $\bar{Y}$. It is defined by following equation:

$$Cov(X,Y) := \frac{1}{n-1} \sum_{j=1}^{n} (X_i - \bar{X})(Y_i - \bar{Y}) \tag{5.2}$$

The overview picture 5.14 shows four measurements and their schematics below a scattered plot. The two measurements "Dist. Interspinalis" and "Dist. Inter-

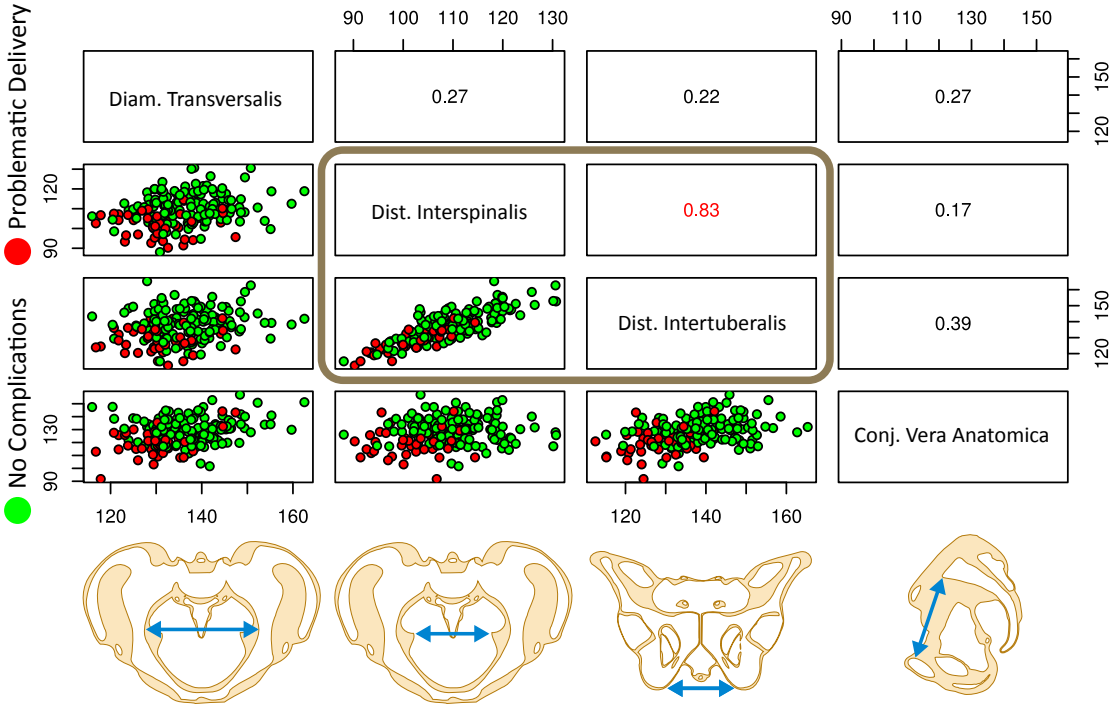

Figure 5.14: Correlation analysis for pelvimetric features. As a detailed view 4 features have been selected. A correlation has been found for Dist. Interspinalis and Dist. Intertuberalis.

tuberalis" are compared and their correlation is calculated. This is illustrated in the image as they are both grouped with the framing box. The names of the two measurements are given in the black boxes drawn on the diagonal of the matrix of boxes. In the box above the diagonal the correlation value of 0.83 is printed in red showing the two measurements are correlated using the definition given above. The point plot below the diagonal shows how the samples are aligned. It can be seen that they apparently define a line. This happens due to the fact that if one of the measurements increases its value, the value of the other measurement increases as well.

Having this in mind one of the two measurements can be disregarded as it does not add further information to a possible prediction model.

The complete scatter plot for all the defined measurements can be found in the appendix C "Pelvimetric Statistics" on page 133.

5.4 Conclusion

A birth score has been defined using a statistical evaluation based on the head deformations from the delivery simulation. If a patient has a maximal deformation of the standard head less than 15 mm they are classified as having a good birth score. This value was chosen as almost 95% of all women fullfill this criterion as can be seen in the percentile plot.

The birth score has been compared with the existing indices such as Fetal Pelvic Index and Pelvic Narrowings and this has shown that their results correlate.

Within the pelvimetric survey the measurements are used in a combined form with the birth score to get more insight how significant the single measurements are and how descriptive they are for a prediction model.

Further measurements as for example the combined ones such as the "BrimArea" and similar were performed and statistically evaluated.

With the help of a correlation analysis the measurements were compared to each other to vote them accordingly. Measurements which correlate with others can be omitted as they are obsolete.

The birth score and the statistical evaluations help to achieve a better overview of the measurements. This is important for generating a prediction model for a safer delivery.

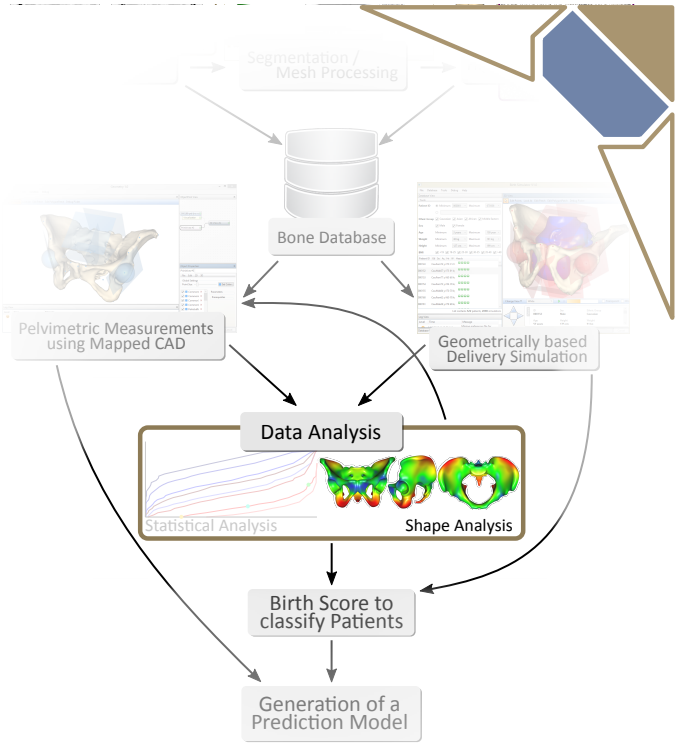

Chapter 6

Shape Analysis

As presented in the medical overview in section 1.1.2 “Pelvic Bone” on page 3, the pelvis is one of the most complex bones of the human skeleton. It consists of several smaller bones as it is presented in figure 6.1.

The mesh representations for every patient’s sample is available in the database as well as registration and mapping information. These meshes and their respective data from the database can now be used to examine what the relevant features, which change from patient to patient, are or what the relevant regions from the pelvis’s surface, which are gender specific, are. What are the differences between male and female pelvises? It is obvious that they differ in size, shape and its bone structure. But which are the relevant structures and regions female pelvises have in common compared to male bones? Can sub-groups of the women be identified representing the part of the women who have a higher risk for obstructed labor and the ones who do not? How do the female ones, which are characterized as showing no complications, differ from the pelvises which do show complications?

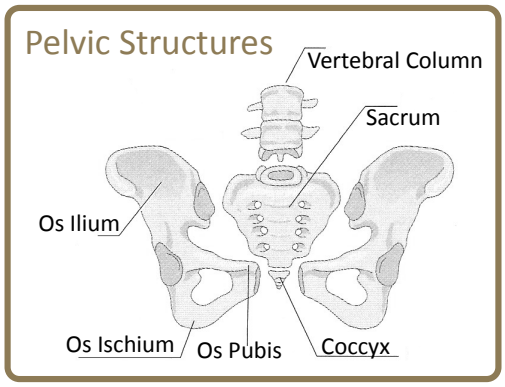

Figure 6.1: Pelvic bone structures from [PBM01].

To achieve that, some research has been done to compare the patients’ bones and to visualize interesting parts and regions for medical experts. Having insight into such special regions makes it possible to investigate these parts of the pelvic bone even further and define some special pelvimetric measurements.

6.1 Mean Pelvis Generation

Physicians and researchers in the field of medicine are often interested in the mean bone. They are interested in the shape which a population has in common. Such a mean bone represents an ideal bone whose surface is the average surface of all provided samples. In the context of this thesis a mean pelvis has to be generated.

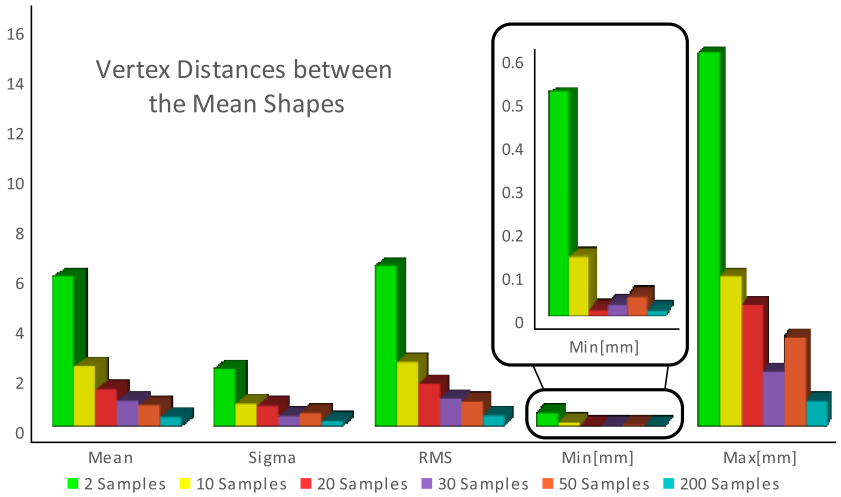

Figure 6.2: Different statistical measures for the vertex distances between the pelvic mean bones.

The bone database consists of more than 500 pelvises and so the mean shape could be generated and based on a large number of specimens as its basis. Nevertheless the question of how many specimens are necessary to get a representative mean pelvis for a population is of interest. To calculate a mean bone the specimens have to be registered to be aligned with some common coordinate system (see section 2.6 “Shape Registration”) and some kind of point correspondence information has to be calculated between different specimens. Using these point correspondences it is possible to calculate the position of a single mesh vertex V_i as the average position of this vertex from all samples.

The necessary correspondence information for points was introduced in section 3.2.1 “Correspondence Generation” (see page 42).

In statistics it is important to know how many entities are required to generate a reliable and significant mean value. Here in the context of calculating a pelvis mean it is important to know how many sample pelvises are required for a significant mean pelvis. Also the rate of convergence is of interest.

For a study different means were generated, each using a different set of randomly chosen patients. The test means were compared with the database mean generated for all of the 524 samples. For a comparison the distances for every

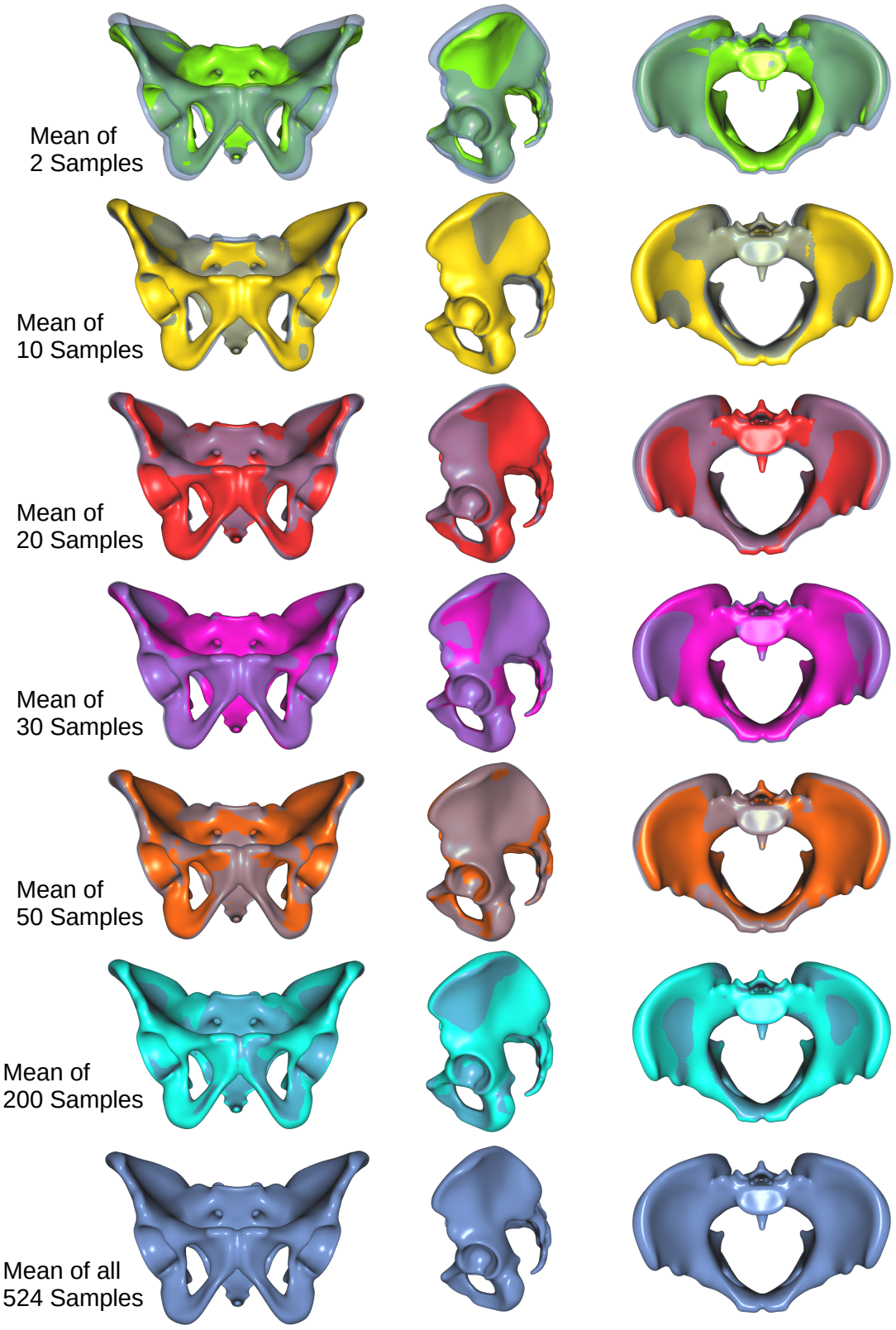

Figure 6.3: A survey of different pelvic mean bones, each of randomly selected patients, compared with the mean of 524 samples.

vertex of the mean is calculated. Statistical values have been derived from those distances which are presented in diagram 6.2 on page 90.

Figure 6.3 (see page 91) shows an overview of such a survey to generate test means from different sample sets. The pelvis means are rendered from three camera positions and are presented horizontally in a row. The last row shows the database mean in blue. The other test means are presented in the rows above, using different colors. Test means are rendered with the overlapping mean from the bone database. The database mean is rendered transparently to show the differences compared to the test means.

6.1.1 Gender Specific Pelvic Means

Having a large set of samples in the database along with the gender information from the database's meta data it is possible to label each pelvis-mesh along with their respective sex.

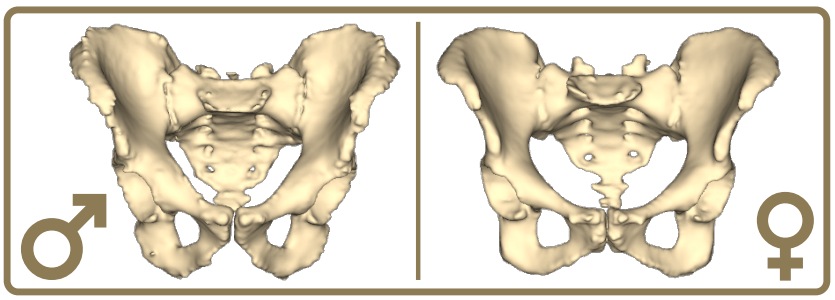

Figure 6.4: Two pelvises of different gender. A male and a female version of a pelvis

It is obvious from figure 6.4 how different the pelvic bone of a male compared to its female version is.

In the previous section it was shown how mean bones were generated using the mapping information which is available in the database as well alongside the mesh data.

By simply grouping the candidate meshes in two sets, F and M, and using the described techniques for the mean generation separately for each set of pelvises, it is possible to create gender specific means. As the mean generation acts like a low pass filter, higher frequencies - for example patient specific and individual irregularities on the bone surface - will be suppressed during the averaging process. The common features within the group (F or M) are preserved.

With the help of the mapping information the generated patient specific means can be compared. So it is possible to calculate the distance from a vertex position of the surface of a female's mean to the respective point on the male's mean.

This measurement can be done for every vertex from the vertex list revealing a list of distance values. These distances can be used to visualize the differences of the two means. The rendering is given in figure 6.5.

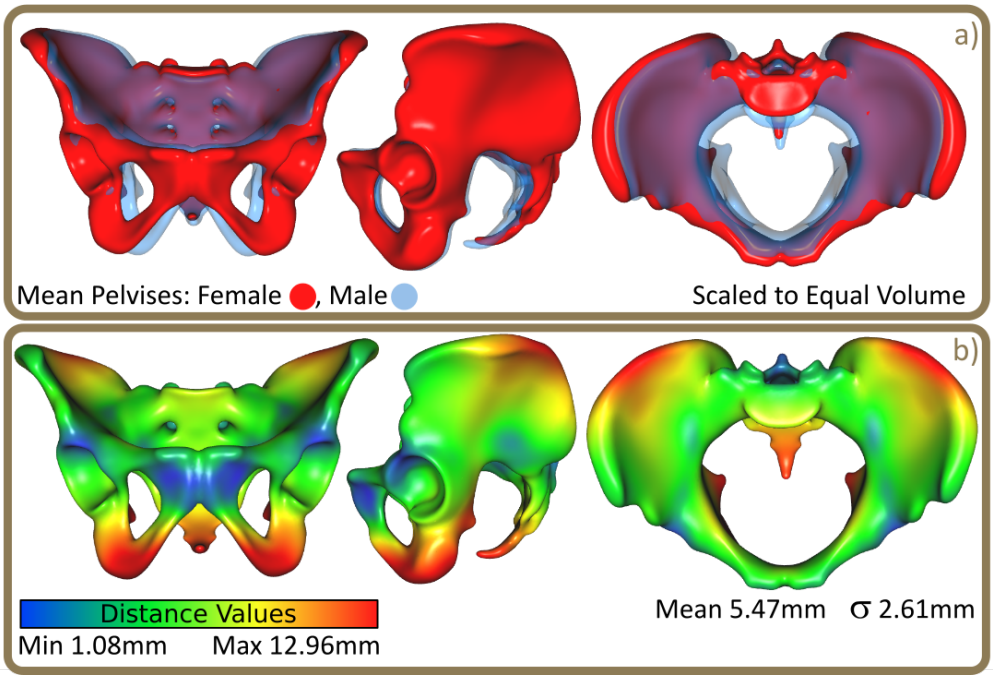

Figure 6.5: Overview of the different gender means (a). Local deviation between gender specific pelvic mean bones (b). Red regions show a higher local deviation than green colored regions.

Image 6.5a shows the two gender specific means with equal volume. To do this the blue mean - representing the males - was scaled down to have the same volume as the red one, representing the female samples. It was done to see that the obvious geometrical differences are not resulting from scaling alone. The blue mean is rendered transparently.

In fig. 6.5b the distance information is illustrated using a heat-map, showing the regions with a higher local deviation of the vertices red and the ones with lower local deviation in blue. Also the statistical values are given.

6.1.2 Birth Score Pelvis Mean

In the context of generating a prediction model for a risk analysis of a delivery to prevent obstructed labor it is far more interesting to generate means from female versions of the pelvic bone and see which areas and regions differ.

With the help of the birth score (see chapter 5 “Pelvimetric Survey” section 5.1 “Birth Scoring”) females can be classified according to their maximal head deformations. The head deformations were calculated and recorded during the delivery simulation for every pelvis and selected baby model. For this survey of the mean pelvis using the birth score the baby head model with 37 cm was chosen and represents the head shape at the upper boundary of head’s circumference range (35 cm $\pm$ 2 cm).

In image 6.6a the two means (best 10% / worst 10%) are drawn overlapping to illustrate the difference. The pelvic means were rendered from three different camera positions: front, left and top. The two means were presented with equal volume like it has been done in the previous paragraph. The green mean - representing the best 10% - was scaled down to have the same volume as the red one. The red mean - representing the worst 10% - is rendered transparently.

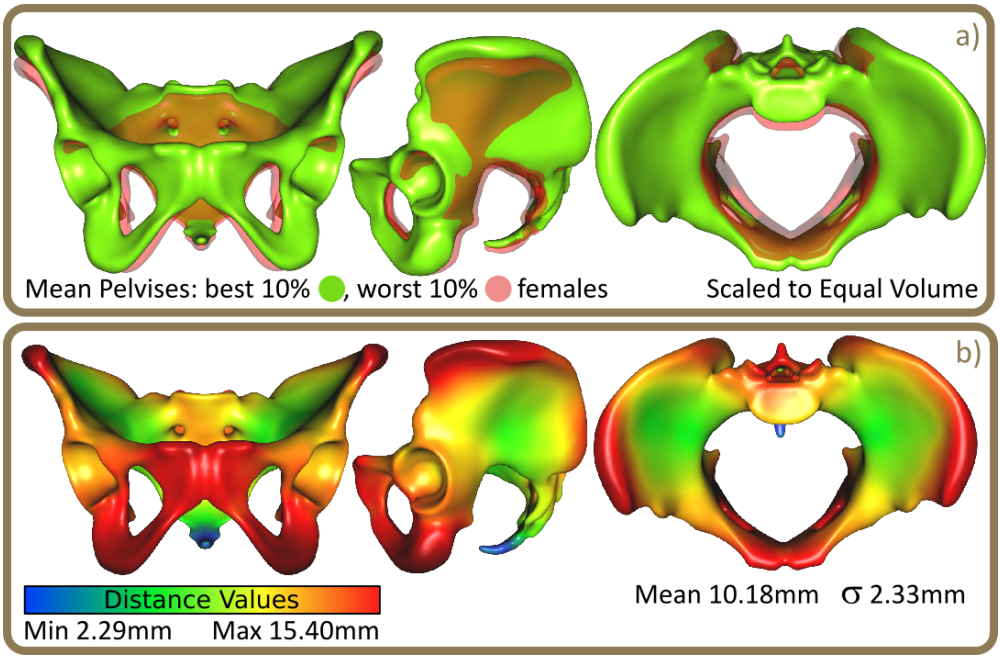

Figure 6.6: Overview and deviation of two different means representing the two classes of females. Green the mean pelvis of the female patients having the lowest maximal head deformation and red the mean of the patients with the highest maximal head deformation.

By calculating the differences between the two single means for each vertex the statistical figures can be calculated as in the previous paragraph. The resulting values and renderings are visible in overview 6.6b, showing red areas predominantly in the pubic and Os Ischii region.

6.2 Point Distribution Models

In the previous section various mean shapes have been generated to identify common regions and areas which are different on the pelvic surface. Such differences are of special interest as they represent possible areas of further investigation. For example, measurements should be defined predominantly in those areas, and the measurements in regions were no differences are found can be disregarded.

But how can this geometrical variance be analyzed more formally than just by a mean generation?

To achieve that Point Distribution Models (PDMs) are used. PDMs are statistical models which reveal the geometrical shape variance by using a mean and statistical modes.

The single entities - the samples - are compared to the mean, and the difference between the sample and the mean is used within the model to determine the relevant changes and variations. Such changes and variations appear in the mathematical model as modes.

Doing that, a mathematical parameter space is defined and the given samples are represented in that space, which is centered around the mean pelvis. The samples are plotted in that space accordingly.

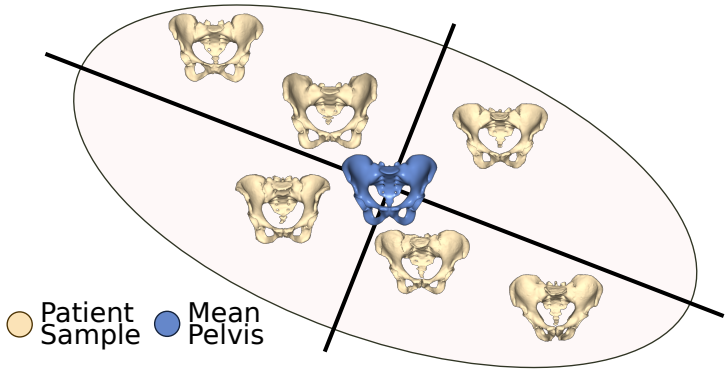

Figure 6.7: Some pelvises aligned into a common coordinate system. Due to their unique size and shape they are different. Similar bones were plotted nearby.

In picture 6.7 the single pelvic bones are drawn in a schematic PDM space to illustrate this in 2D. According to the pelvis' parametrization - here a parameter vector $\vec{b}$ - the samples are plotted in the PDMs intrinsic coordinate system, which is derived by the model's eigenvectors.

The idea is that pelvic bones which resemble each other in some way, for example due to the same height or similar measurement results, will have similar parameters $\vec{b}$ and are plotted in nearby regions within the PDM space.

The eigenvectors are derived for their respective eigenvalues. The absolute

value of the eigenvalue can be interpreted as the influence this special eigenvector has within the model. It is therefore a measure of how significant such an eigenvector is.

Interpreted that way, the eigenvectors are called modes and can be grouped according to their influence in strong or weak modes. Strong modes have more influence than weak ones as they deform the mean pelvis more than the weak modes. The strongest mode is scaling.

The resulting eigenvectors can be sorted in descending order according to their eigenvalues. This way they are ordered to the influence they have on the geometrical changes. As the weak modes do not have much influence by morphing the pelvis, a parameter reduction can be carried out. That can be done by selecting the strong modes and by disregarding the weaker ones to define a subset of modes. This subset defines the support the selected mode selection has. For example the ten strongest modes represent 81% of all the geometrical variations. To provide a coverage of 98.5% 133 modes are required. The plot 6.8 gives an overview of the geometrical variance and how it depends on the PDM mode count. The total variance of 100% is given by the sum of all eigenvalues. A coverage of 98.5% means that enough modes are selected and provided within the model to get 98.5% support of the total eigenvector sum.

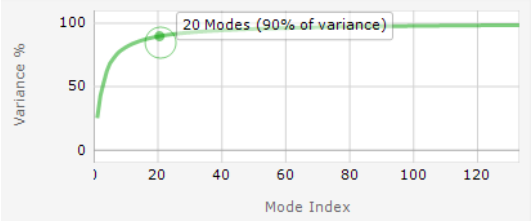

Figure 6.8: Plot showing the geometrical variance in percent dependent on the PDM mode count.

6.2.1 Pelvis PDM Generation

A PDM is represented by a matrix Φ which is made of the eigenvectors of the covariance matrix AA^T. To generate such a model the matrix Φ has to be determined for the set of patients.

From a set of patients $P := \{\vec{p_i}\}$ a single pelvis can be seen as an instance of a parameter vector $\vec{p_i} := (x_0, y_0, z_0, x_1, y_1, z_1, \ \ldots \ x_{n-1}, y_{n-1}, z_{n-1})^T \in \mathbb{R}^{3n}$ with n the vertex count of the respective pelvic mesh.

The generation of the required mean pelvis was presented in detail in section 6.1 “Mean Pelvis Generation”. Normally the correspondence information which is needed for generating a Point Distribution Model is done manually for

every sample. Using the mapping information from the database this can be done automatically. The mean pelvis is represented by the parameter vector $\bar{p}$.

As every vertex $V_i := (x, y, z) \in V$ of a mesh (V, F) is defined using $x, y, z \in \mathbb{R}$ it uses three spatial dimensions. In contrast to the original PDM generation approach, which is given in [CT04], the samples are not scaled to have a common height, extent and volume. The original sizes are preserved as they represent an important feature of the single bone samples and should therefore be preserved within the model. As will be shown later, the scaling will be the most influential mode.

So having a pelvic bone mesh with $n = 50,000$ vertices would result in a parameter vector $\vec{p_i}$ of $150,000$ dimensions. The mean pelvis $\bar{p}$ and the sample pelvises - parameter vectors $\vec{p_i}$ - will be combined as column vectors to form a matrix A:

$$\begin{aligned} A &:= \left(\vec{p_0} - \bar{p} \quad \vec{p_1} - \bar{p} \quad \dots \quad \vec{p_{n-1}} - \bar{p}\right) \in \mathbb{R}^{3n \times |P|} \\ &\rightarrow AA^T \in \mathbb{R}^{3n \times 3n} \end{aligned} \tag{6.1}$$

The covariance matrix which will be used is AA^T and would have $150,000^2$ elements. It is not sparse, and by using doubles for the entries it will result in a memory usage of 167 GB, which is too large.

To resolve this problem two approaches were examined:

- **Vertex Reduction** One way to overcome this fact is to reduce the vertex count of the mesh by using the mesh simplification algorithm which had been used during the actual import of the pelvic bone. The mesh from the database can be simplified even further to have a low resolution version with a lower vertex count. The used mesh simplification algorithm (see section 2.3 "Simplification" in chapter 2 "Bone Database") ensures that only small changes of the shape's geometry occur.

  A simplified sample mesh of a pelvis with a vertex count of approximately $8,000$ vertices would lead to a matrix size of 4.4 GB and is therefore manageable on current hardware.

  Determining the eigenvalues using a simplified mesh shows that only $|P|$ eigenvalues are $\neq 0$. This result leads to another technique.

- **Indirect Solution** To overcome this fact and to deal with that covariance matrix and to determine its eigenvectors can be achieved by using $A^T A$

instead of the standard way AA^T. Using this the matrix will be much smaller - $A^TA \in \mathbb{R}^{|P|\times|P|}$ - as the bone database has 537 pelvises: $|P| \ll 3n$ with n as vertex count.

This can be done because the eigenvalues λ_i from A^TA are the same as for AA^T:

$$\begin{aligned} A^TAx &= \lambda x \quad \text{with } A^TA \in \mathbb{R}^{|P|\times|P|} \\ AA^TAx &= \lambda Ax \mid \cdot A \text{ from left} \\ AA^Ty &= \lambda y \text{ with } y = Ax \end{aligned} \tag{6.2}$$

After the determination of the eigenvalues λ_i the eigenvectors have to be calculated. They have to be transformed with A to get the respective eigenvectors for AA^T.

So with the 537 pelvises from the bone database the matrix A^TA has 537^2 double entries and requires about 2.2 MB of memory.

Algorithm 8 Steps to Calculate the Point Distribution Model

1. Compute the mean of the pelvises

$$\bar{p} := \frac{1}{|P|}\sum_{i=1}^{|P|}\vec{p_i} \text{ , with pelvis } \vec{p_i} \in P \text{ set of pelvises}$$

2. Compute the matrix A by concatenating the pelvic parameters $\vec{p_i}$:

$$A := \begin{pmatrix} \vec{p_0} - \bar{p} & \vec{p_1} - \bar{p} & \dots & \vec{p_{n-1}} - \bar{p} \end{pmatrix} \in \mathbb{R}^{3n\times|P|}$$

3. Compute the matrix $A^TA \in \mathbb{R}^{|P|\times|P|}$ instead of $AA^T \in \mathbb{R}^{3n\times3n}$.

4. Compute eigenvalues λ_i for A^TA and the eigenvectors Φ_i for AA^T by using A as an additional transformation for the eigenvectors of A^TA.

5. Before constructing matrix Φ using the eigenvectors Φ_i the eigenvectors have to be sorted descendently according to their eigenvalues. The t largest eigenvalues are used to define Φ:

$$\Phi := (\Phi_1|\Phi_2|\dots|\Phi_t) \text{, orthogonal matrix}$$

Having an effective way to determine the eigenvectors ϕ_i of AA^T the matrix Φ can be defined to get the required Point Distribution Model. The steps for

creating a PDM is given in algorithm 8.

With the matrix Φ it is possible to reconstruct any sample $\vec{p_i}$ of the training set by approximating its representation using:

$$\vec{p_i} \approx \bar{p} + \Phi\vec{b_i} \Rightarrow \vec{b_i} := \Phi^T(\vec{p_i} - \bar{p}) \text{ , as } \Phi^T\Phi = I \text{ Identity} \tag{6.3}$$

The parameter vector $\vec{b}$ controls the deformable model. Varying the parameter vector's elements b_i the model's shape changes. Every given sample $\vec{p_i}$ of set P has an unique parameter vector $\vec{b_i}$. The valid range for every element of the parameter vector is given by its corresponding eigenvalue $\pm 3\sqrt{\lambda_i}$.

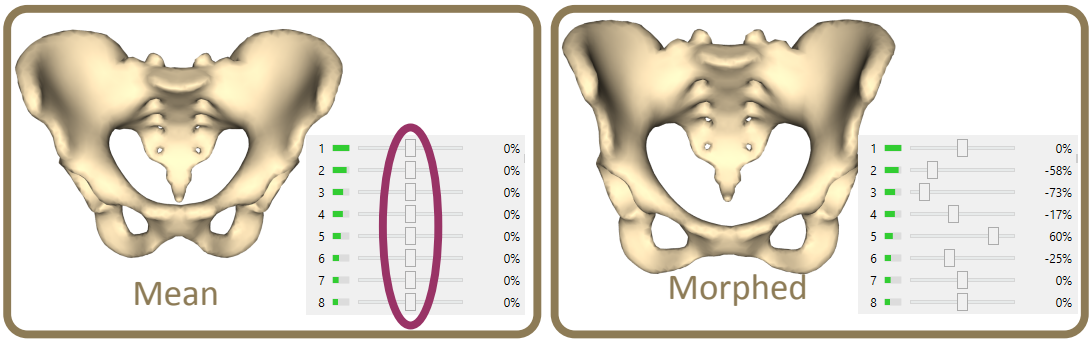

Figure 6.9: Pelvic shapes and their parameter vectors $\vec{b}$. The mean is represented by $\vec{b} = 0$ (a) and a patient from the database with its respective parameter vector $\vec{b}$ visualized with sliders (b).

The mean pelvis ($\vec{b} = 0$) can be morphed by changing the elements of $\vec{b}$. In fig. 6.9 the vector $\vec{b}$ is represented by a set of sliders. A slider's range is given by the respective mode's eigenvalue λ_i leading to $[-3\sqrt{\lambda_i}; +3\sqrt{\lambda_i}]$. Between the samples it is possible to interpolate and deform the pelvic mean by changing the elements' values of $\vec{b}$.

6.2.2 PDM Projection

Once the PDM has been derived for the pelvises it can be used for further analysis. As a single sample bone is represented uniquely by the parameter vector $\vec{b}$ it is in some way a point in the PDM space.

It is actually not possible to visualize the entire PDM space as it has far more than three dimensions. But it is possible to visualize a subset of the dimensions by projecting the overall PDM space into 3D.

Figure 6.10 shows an overview of the pelvises and how they are plotted as points in the projected PDM space. The projection is done in 3D by selecting

three specific elements of the $\vec{b}$ vector describing a single pelvic bone. Three different mode configurations are rendered.

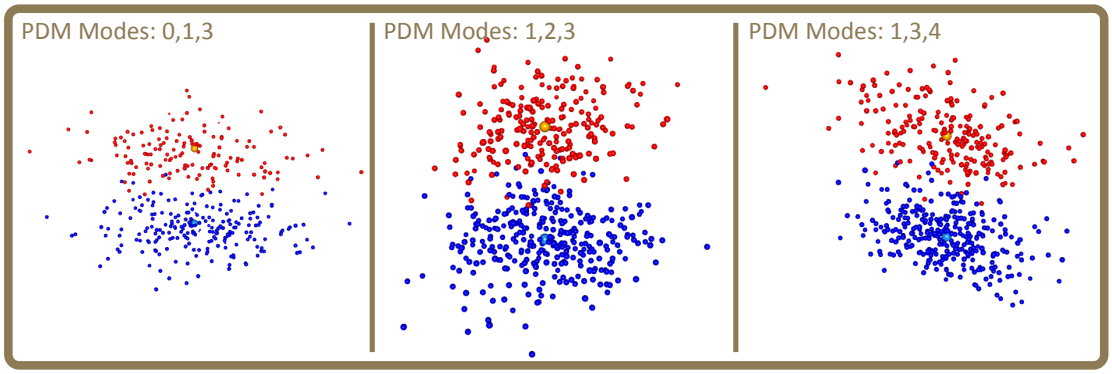

Figure 6.10: A projection of three PDM modes in 3D space. The single points are color coded according to their respective gender: female red - male blue.

In addition, the points were rendered in two colors, representing the respective patient's sex from the patient's meta information. Females are rendered in red whereas the male ones are drawn in blue.

It is interesting how the points - representing the pelvises - are distributed in the PDM space appearing to form two clusters which represent the two genders.

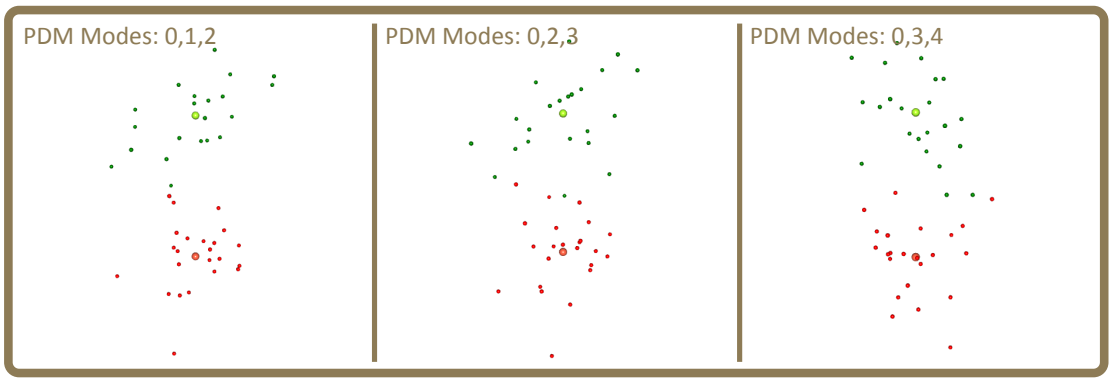

Figure 6.11: A projection of three PDM modes in 3D space. Only the 10% of the best/ 10% of the worst females are plotted. The single points are color coded according to their respective class: lowest 10% maximal head deformation green - maximal 10% maximal head deformation in red.

The same technique can be used to project patients who show the 10% lowest and the 10% highest head deformation values. Figure 6.11 shows the 20% of the females, color encoded. Green dots represent the female patients with low deformation values whereas red points show the female patients with high values.

6.2.3 Eigenvector Visualization

In the PDM space the pelvic bones are represented via the parameter vector $\vec{b}$. By varying $\vec{b}$'s elements the shape can be morphed as it was presented in the previous paragraph. To investigate the pelvic bone even further and to visualize how a single vertex of the pelvic mesh is transformed during the morphing process the eigenvectors should be visualized.

The elements of the vector $\vec{b}$ are weights. These weights control how elements of an eigenvector Φ_j - as being a column vector of the matrix Φ - influence the vertices of a shape and therefore the whole pelvic mesh.

A morphed pelvic mesh is given by $p^* = \bar{p} + \Phi\vec{b}$ and is parametrized by combined and vertically stacked 3D vectors forming $p^* \in \mathbb{R}^{3n}$. So a vertex $V_i^* \in \mathbb{R}^3$ is defined by $V_i^* = (\bar{p})_{3i} + (\Phi\vec{b})_{3i}$.

By selecting a single mode, a single eigenvector can be chosen and analyzed even further as to how it influences the final vertex location. An eigenvector $\Phi_j \in \mathbb{R}^{3n}$ resembles the sample vector $\vec{p_i}$ as it is combined of single vertically stacked 3D vectors. These eigenvectors can be interpreted geometrically as single vectors which translate a shape's vertex along that direction. Larger eigenvectors have more influence than others. By using the length information of such an eigenvector, which is mode dependent, and doing this for all vertices of the mesh, it can be color encoded.

For a single vertex V_i and an eigenvector ϕ_j a displacement vector $\vec{\phi_{ji}} := (\Phi_{j,3i+0}, \Phi_{j,3i+1}, \Phi_{j,3i+2})$ can be defined. The displacement vector $\vec{\phi_{ji}}$ translates the vertex V_i for mode j. The parameter vector's element $\vec{b_i}$ act as a scale factor for the displacement vector $\vec{\phi_{ji}}$.

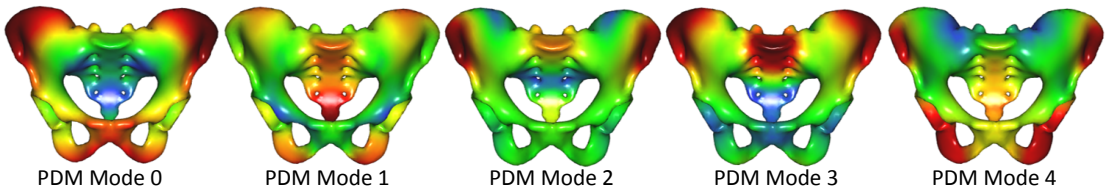

Figure 6.12: Color coded length of eigenvectors on the mean pelvic bone for the five strongest modes.

To examine regions which are deformed more than others, the eigenvector Φ_j and its respective parts $\vec{\phi_{ji}}$ can be used. Figure 6.12 shows five different renderings of the pelvis mean shape color encoded using a heat-map. Each rendering represents the displacements for a single eigenvector Φ_j and the vertices V_i of the

mean pelvis are rendered according to their respective length of the vector $\vec{\phi_{ji}}$. Vertices V_i with a high dislocation - influenced by a long displacement vector $\vec{\phi_{ji}}$ - are rendered in red, whereas vertices with little movement are shown in blue.

For example the ilium is influenced by mode 0 as larger displacements are rendered in red in figure 6.12. Mode 1 influences mostly the sacrum.

6.3 Conclusion

The pelvic bone shapes from the database have been used to gain more insight into how different they are and it was shown how the sample bones resemble one another. They have similar shapes, and by generating a mean bone from the samples, the common structures are preserved and become visible while small spikes and individual geometrical outliers are suppressed during the nature of a mean generation. Via the point correspondences it is possible to generate the mean from a large set of patients. A study revealed how the mean generation is sensitive to different patient counts and how many patients are required to generate a representative mean. Different means have been generated, which show the differences between the two genders and between different groups of females.

Further a Point Distribution Model has been generated to compare the geometrical variance of the pelvises more formally. It has been used for deriving modes and has visualized them via projections. These projections reveal an interesting point distribution between the male and female samples within the PDM space. The eigenvectors of the PDM can also be used to visualize the geometrical variances of the bones, as they represent the local modifications which are influenced by the specific modes.

Using the analysis and visualization techniques, medical experts are able to identify more relevant regions on the bone's surface and judge the single measurements of the pelvimetry according to their relevance.

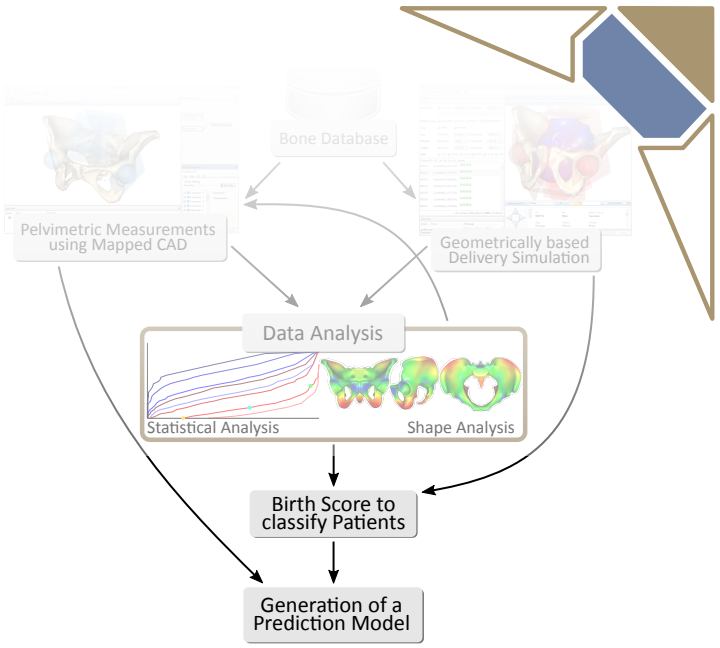

Chapter 7

Prediction Model

In previous sections the data acquisition, the pelvimetric measurements using the Mapped CAD functionality from the bone database and the delivery simulation have been introduced. The statistical evaluation of the measurements has been presented in section 5.3 “Pelvimetric Statistics” and the presented correlation analysis has shown that some measurements have a higher significance than others as they are not in the some way dependent on others. The defined birth scores which have been derived and presented in section 5.1 “Birth Scoring” can now be used to label the patients according to their ability to bear a child.

Using and combining all those techniques and the generated data, it is now possible to generate a prediction model using techniques and algorithms from machine learning. To achieve this the statistical data have to be analyzed and suitable techniques have to be selected to rate which of the possible pelvimetric measurements are significant enough to be used in a prediction model. And that does also mean which of the features can be selected to reduce the required measurement count to derive a simpler model with fewer features.

One of the used methods is Logistic Regression, which has already been used in other medical studies. In addition a Support Vector Machine (SVM) has been used to derive a prediction model.

All evaluations are done and the various models are generated with the statistical software package R[1].

In the following sections, a brief overview of machine learning and an explanation of how the models have been derived using the mentioned algorithms is given. Using the generated models in standardized tests some key values are generated

[1] R Project, 2014-10-15, *http://www.r-project.org/*

to compare the different models according to their prediction performance in the field of birth prediction.

7.1 Supervised Learning

In contrast to normal problem solving strategies where computers are used to solve equations and calculate results for a given task in machine learning the model itself is not known and is the actual result of the calculations.

To derive and develop such a model a training set $M := \{m_i\}$ of samples m_i is required. Using this training set M it is possible to fit model parameters rather than implementing a decision tree for that specific set.

In the so called "Supervised Learning", the training set M consists of l input/output pairs $M := \{m_i = (\vec{x_i}, y_i)\} \subset X \times Y$ with $|M| = l$. The sample m_i is a tuple of two items: $\vec{x_i}$ defines the input vector of such a pair whereas y_i represents the output or labeling for that sample m_i.

The pairing of a sample value and its appropriate label defines an implicit mapping. A learning algorithm tries to generate a so called decision function $\mu(\vec{x}) := X \mapsto Y$ which represents the decision model and the implicit mapping given by the input set. The various pelvimetric measurements will be used as the patient's attributes $\vec{x_i} \in X \subset \mathbb{R}^n$ for n measurements. For the output of such a pairing we can use the birth score to define a label $y_i \in Y := \{-1, +1\}$:

$$y_i := \begin{cases} -1, \text{ if maximal head deformation} \geq 15 \text{ mm} \\ +1, \text{ if maximal head deformation} < 15 \text{ mm} \end{cases} \tag{7.1}$$

The final aim is to generate a model which is not only capable of representing the implicit mapping for the given training set but also for a priori unknown values $\vec{x_j} \in X$ which were not used in the original training set M. So all available samples for which the features and labels are known, can be subdivided into two sets M and T. Whereas M is used as the training set T is used for testing the trained model. Typically a set $T := (\vec{x_j}, y_j) \subset X \times Y$ is defined in such a way that the two sets M and T are disjoint: $M \cap T = \emptyset$.

Fitting the parameters during the model generation it is the goal to classify the samples m_i of the training set M in the correct way so that the input labels y_i match the predicted labels $\mu(\vec{x_i})$. The generalization performance for the model is measured by testing the samples $t_i \in T$ from the test set T.

As described in the previous paragraph, two aims exist when fitting a model. First find a model μ, also called hypothesis, which classifies the training set M correctly, and than compare that model μ_i to other models μ_j according to their generalization performance.

The different models μ_i, μ_j do not necessarily require the same parameter count or even parameterization. So it is possible that model μ_i has a decision function $\mu_i := \mathbb{R}^n \mapsto Y$ and $\mu_j := \mathbb{R}^m \mapsto Y$ with $m \neq n$ in the general case.

7.2 Model Generation

Binary classification is typically done via a separating hyperplane $H \in \mathbb{R}^n$ in n dimensions. For a point $p \in \mathbb{R}^n$ the binary predictor measures the signed distance and determines with the help of the sgn function the resulting class for p. A hyperplane $H \subset \mathbb{R}^n$ can be described by a $n+1$ tuple $(\vec{\nu}, d)$ where $\vec{\nu} \in \mathbb{R}^n$ is the hyperplane's normal and $d \in \mathbb{R}$ the perpendicular distance value to the origin. Figure 7.1 shows a blue line representing a hyperplane in 2D space.

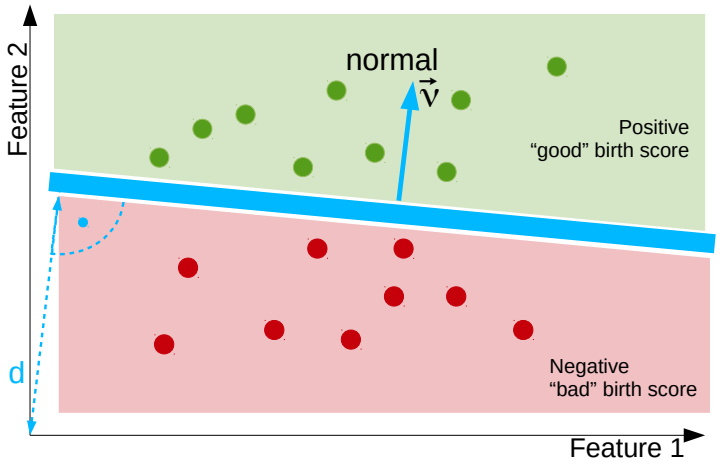

Figure 7.1: A hyperplane $H = (\vec{\nu}, d)$ separating a 2D space into two half spaces. The space is defined by two features and the samples are plotted according to their features' values color encoded representing the labels of the samples.

To fit a predictor model using a hyperplane it is necessary to fit the hyperplane's parametrization and find the optimal values for $\vec{\nu}$ and d. So a model μ can be expressed as a hyperplane H for a given training set M.

In the following sections two different algorithms, which are later used to derive prediction models, are presented.

7.2.1 Logistic Regression

One way to determine a hyperplane is to use Logistic Regression. With this technique the parameters required to describe a model for a given training set can be determined. The Logistic Regression is a probabilistic statistical classification model. It is used to predict the response of a binary predictor for a given sample and to determine which one of the two classes of the binary response is more likely than the other.

It has been used in medical statistics for example in the Coronary Risk-Factor Study (CORIS) survey in South Africa [RDPB+83, HTF09].

Logit and Probability

The Logistic Regression Model consist of the logistic function $\sigma(t) := \frac{1}{1+e^{-t}}$ which is a to the sigmoid function and is plotted in figure 7.2.

Figure 7.2: The logit function $\sigma(t)$.

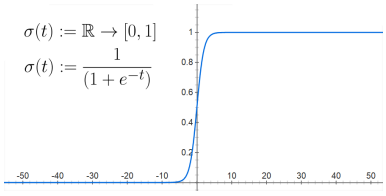

The parameter t in $\sigma(t)$ can be defined as a linear function $t(x) = \beta_0 + \beta_1 x$ representing a line. Using this and replacing the constant t with the linear function $t(x)$ in $\sigma(t)$ leads to $F(x) := \sigma(t(x))$:

$$F(x) := \frac{1}{1 + e^{-(\beta_0 + \beta_1 x)}} \tag{7.2}$$

The parameters β_0 and β_1 are elements of a vector of parameters $\vec{\beta} \in \mathbb{R}^2$ which controls the model by adjusting the logistic function accordingly. The two given parameters are an example of a parameter-space representing a line. By adding more parameters the parameter space can be altered and generalized to represent a hyperplane $H \in \mathbb{R}^n$ in $n+1$ dimensions with $\vec{\beta} \in \mathbb{R}^n$. The extra dimension is necessary because $\vec{x}$ is augmented with an extra dimension set to 1 to handle the bias β_0 in a compact way.

$$F(\vec{x}) := \frac{1}{1 + e^{-(\vec{\beta}^T \vec{x})}} \tag{7.3}$$

Inverting the function $\sigma(x)$ leads to the *logit* function which can be seen as the "logarithm of the odds" [2]:

$$logit(\vec{x}) := \ln \frac{F(\vec{x})}{1 - F(\vec{x})} \tag{7.4}$$

Therefore the value of $F(\vec{x})$ can be interpreted as the probability that the value $\vec{x}$ has a specific label $y \in Y$.

To fit the model parameters $\vec{\beta}$ representing the hyperplane H, which can be used for the later classification whether a female patient has a "good" or "bad" birth score, a Maximum Likelihood Estimation (MLE) has to be performed [HTF09].

The Maximum Likelihood Estimation is a method for estimating the parameters of a statistical model. Here, the model can be interpreted as the hyperplane H which is encoded by the concatenated vector $\vec{\beta} := (\vec{\nu}|d) \in \mathbb{R}^{n+1}$, defining the hyperplane's parameters, in which $\vec{\nu} \in \mathbb{R}^n$ represents the hyperplane's normal and $d \in \mathbb{R}$ the distance from the origin.

7.2.2 Support Vector Machine

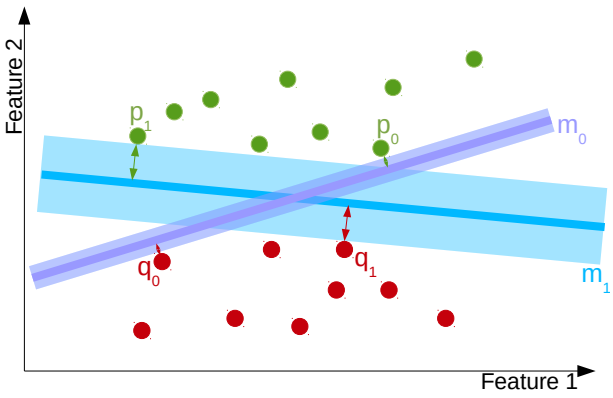

Figure 7.3: Different models m_0, m_1, their functional margin and their support vectors.

Another type of classifier is the Support Vector Machine (SVM). Such a classifier tries to separate a set of samples, the training set S into subsets of different classes in such a way that the space between the classes will be maximized. Therefore a Support Vector Machine is called a "Large Margin Classifier" [Bis06, CST00].

The term "Large Margin Classifier" means that the optimization process that determines the relevant hyperplane during the fitting process maximizes the distance from the nearest sample points to the current candidate plane.

[2] $odds(A) := \frac{P(A)}{1-P(A)}$ the ratio of the probability of an event A and the probability complementary event.

This maximization of the minimal distance ensures that the selected hyperplane H^* has the property of maximal space between the nearest sample vectors. Such points are called the "Support Vectors".

An example for two models μ_0 and μ_1 as well as their respective support vectors can be seen in figure 7.3: $\{p_0, q_0\}$ for μ_0 and $\{p_1, q_1\}$ for model μ_1. The models' margins are illustrated with different line widths in that figure.

More formally the binary classification can be described as a function $\mu(\vec{x}) := X \subseteq \mathbb{R}^n \mapsto Y$ where X is a set of samples which are given by attribute vectors $\vec{x_i}$. The model's decision function $\mu(\vec{x})$ can be defined in the following way:

$$\begin{aligned} \mu(\vec{x}) &= \text{sgn}(< \vec{w}, \vec{x} > +b) \text{ with } \vec{w}, \vec{x} \in \mathbb{R}^n, b \in \mathbb{R} \\ &= \text{sgn}((\sum_{i=1}^{n} w_i x_i) + b) \end{aligned} \tag{7.5}$$

The function $\mu(\vec{x})$ uses the parameter vector $\vec{w}$ and the value b, which can be interpreted as the parametrization of a hyperplane H with normal direction $\vec{w}$ and distance b. The name $\vec{w}$ has been chosen as an abbreviation for "weights" and b for "bias". Using the sgn function you can distinguish between the two classes.

By evaluating the function $\mu(\vec{x})$ for a given sample $\vec{x}$ the results can be interpreted as the signed distance from that point to the projected point $\vec{x'}$ onto that hyperplane H.

The Support Vector Machine uses a so-called dual form of the parametrization, meaning that the normal of the plane is defined in a special way as it depends on the support vectors, which can be seen in equation 7.6.

$$\vec{w} = \sum_{i=1}^{l} \alpha_i y_i \vec{x_i}, \alpha \in \mathbb{N}^+ \tag{7.6}$$

The elements α_i of vector $\vec{\alpha}$ in equation 7.6 is defined to be the sample's weight of a sample $\vec{x_i}$. Using such a weight it can be expressed that a sample has more influence than others. The support vectors - being the samples having the minimal distance to the plane - have higher weights than other samples and therefore define the plane $\vec{w}$ indirectly.

The decision function can now be expressed in the following way:

$$\mu(\vec{x}) = \text{sgn}(\sum_{i=1}^{l} \alpha_i y_i < \vec{x_i}, \vec{x} > +b) \tag{7.7}$$

Normally, a separating hyperplane may not always exist. Reasons for that can be seen in the fact that there is on the one hand a high noise level, which causes a large overlapping of the classes, and on the other hand the classes are not separable and overlap slightly. To find a separating hyperplane in the presence of a small set of outliers, a "Soft Margin SVM" exists.

A hyperplane $H = (\vec{w}, b)$ must fulfill following requirement:

$$y_i(< \vec{w}, \vec{x_i} > +b) \geq 1 \tag{7.8}$$

This requirement is true if the predicted label $< \vec{w}, \vec{x_i} > +b$ equals the ground truth label y_i. In contrast to that a soft margin hyperplane allows a possibility of violating that requirement by introducing slack variables ξ_i and formulating:

$$y_i(< \vec{w}, \vec{x_i} > +b) \geq 1 - \xi_i \text{ with } \xi_i \geq 0 \tag{7.9}$$

Another way to overcome non-separability is to use kernel functions. The inner product in equation 7.7 is generalized by introducing the so-called kernel function $K(\vec{x_j}, \vec{x})$. With the help of such a generalized kernel it is possible to calculate an inner product directly in the feature space which depends on the original attributes from the original attribute space. Using different kernels non-linear classification is possible with a linear classification algorithm.

$$\mu(\vec{x}) = \text{sgn}(\sum_{i=1}^{l} \alpha_i y_i K(\vec{x_i}, \vec{x}) + b) \tag{7.10}$$

To fit a SVM model, a quadratic function has to be optimized according to linear constraints. Such an optimization can be done by gradient descent techniques, having in mind that a local extreme value of a quadratic function is the global extreme value of the problem. The SVM models have been fitted using the "kernlab" package within the statistics software R (see [KSHZ04] for this).

7.3 Model Evaluation

Once a model μ has been generated using the described techniques and the training set M in the previous section, the model can be evaluated. To test it the samples $(\vec{x_i}, y_i) \in T$ are evaluated with the model μ to compare its outcome $\mu(\vec{x_i})$ with the predefined label y_i.

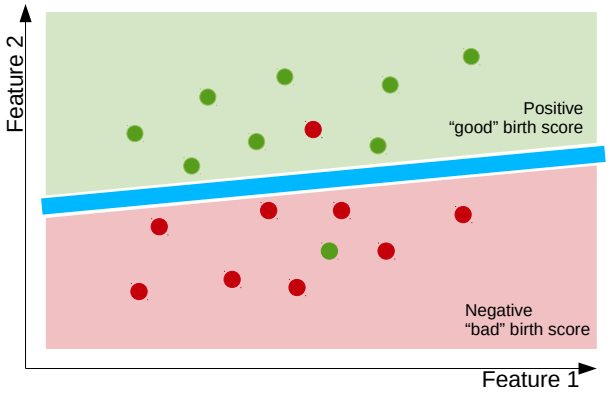

Figure 7.4: Example of non separability.

The diagram in fig. 7.4 shows the samples which are ordered according to their features' values, here feature 1 and 2. The labels of the samples are illustrated via different colors. A line (in blue) divides the $\mathbb{R}^2$ space into a positive and negative half-space, which is located above and below the blue line. The training set is not linearly separable as there are some samples which have a "good" birth score but are located in the negative half-space. These mislabelled samples appear on half-spaces of different color than their own. Figuratively they are printed in green and are located in the red region (False-Negatives). And on the other hand there are False-Positives, the red ones which are located in the positive half space above the blue line.

7.3.1 Testing and Classification Method

A simple test is to count all the mislabelled samples which have another outcome $\mu(\vec{x_i})$ than the corresponding label y. The ratio between the mislabelled sample count and the total sample count is defined as being the "Accuracy".

A more elaborate view is given in figure 7.5. The four possible characterizations True/False Positive/Negatives are visible in figure 7.5, framed by the blue rectangle.

Confusion Matrix With the help of this sample characterization, more sophisticated key values can be defined to evaluate the models $\mu(\vec{x})$. Figure 7.5 shows a diagram which orders the sample counts according to their characterizations as being True/False Positives/Negatives (figuratively the four cells within the blue rectangle).

The diagram shows how important key values like "Sensitivity" (TPR - True Positive Rate) and "Specificity" (True Negative Rate - TNR) are defined and how they are worked out as they rely on the True Positives and True Negatives. They are statistical measures to quantify a binary classifier's performance. The "Sensitivity" represents the portion of the samples which are correctly classified,

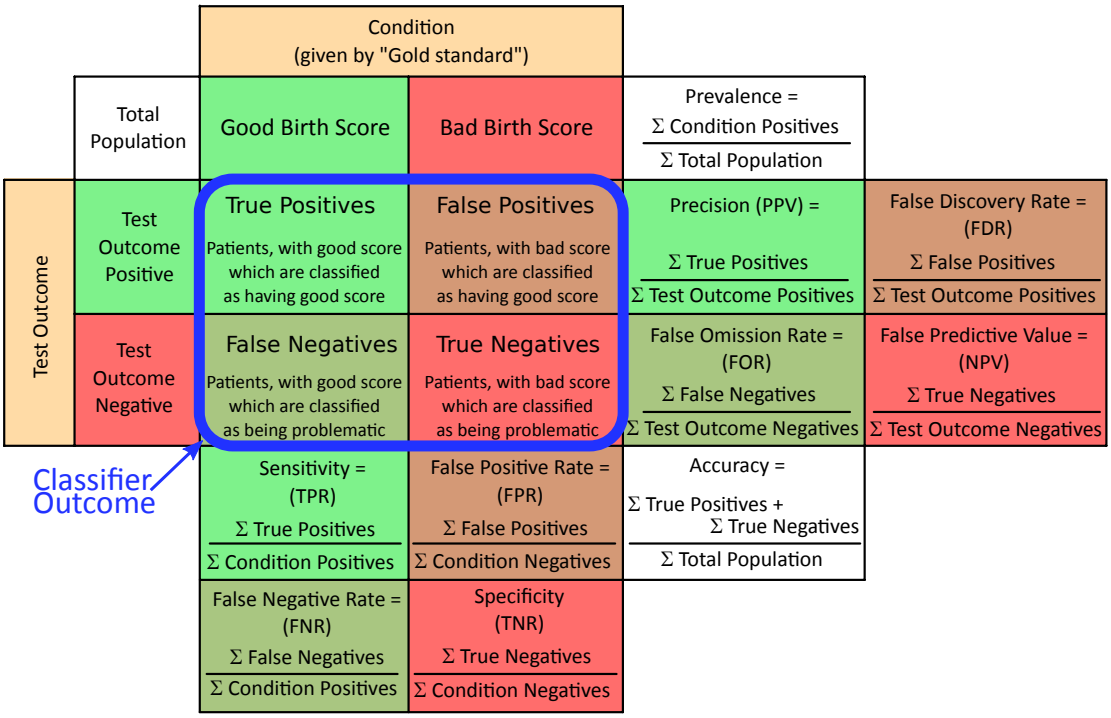

Figure 7.5: The confusion matrix which shows schematically the classification result and the derived classification measures [Faw06, Pow11].

having a good birth score, and the "Specificity" quantifies the portion of the samples which are correctly classified, having a bad birth score.

Their complementary values are "False Negative Rate" (FNR) and "False Positive Rate" (FPR). The FNR measures the ratio of how many patients are classified as to having a good birth score but are labelled with a bad one, whereas the FPR quantifies the ratio of patients who are classified wrongly as having a bad birth score.

The best possible predictor has a sensitivity rate of 100% and a specificity rate of 100%, the complementary error values being $FPR = 0\%$ and $FNR = 0\%$, which shows that all samples are classified correctly.

K-Fold Cross Validation The actual values in the table are calculated by using a 5-fold cross validation test. With such a k-fold cross validation test (with $k = 5$), the set of all samples are split into five disjoint parts: $P_{i\in\{0...4\}}$. The samples are distributed randomly to be elements of the different partitions [WNC05]. For each of the five test cycles, the two sets M and T are generated from the five parts. The using of 80% of all samples which are given by 4 of the 5 partitions defines the

	14 Standard Measurements				
	Accuracy	Sensitivity (TPR)	Specificity (TNR)	FPR	FNR
LR	87.4%	92.9%	69.2%	30.8%	7.1%
SVM	90.4%	94.2%	78.0%	22.0%	5.8%

Table 7.1: Classification measures for the 14 standard measurements using 80% for the model and 20% of the 200 female samples for testing. The tests have been performed using 5-fold cross validation.

training set M and the remaining partition (= 20%) defines the test samples T. For the i^{th} cycle the sets are $T_i := P_i$ and $M_i := \bigcup_{j=0}^{k-1} P_j \setminus T_i$. This leads to $M_0 := P_1 \cup P_2 \cup P_3 \cup P_4$ and $T_0 := P_0$ for the first cycle. After the model generation the classification values TPR_0, TNR_0, FNR_0 and FPR_0 can be calculated. In the second cycle you can define $T_1 := P_1$ and $M_1 := P_0 \cup P_2 \cup P_3 \cup P_4$ respectively, etc.

The resulting key measure $TPR := \frac{1}{k} \sum_{i=0}^{k-1} TPR_i$ is defined to be the mean of the corresponding values for each of the k cycles of the cross validation test. Using that the other classification values - TNR, FNR and FPR - are defined in the same way.

Classification of Standard Measurements

Using the proposed measurements which have been derived from Anapelvis (defined in section 1.3 “Anapelvis” of chapter 1 “Introduction”), a set of 14 standard pelvimetric measurements can be defined and selected to fit the models $\mu_{Standard,LR}$ and $\mu_{Standard,SVM}$. The classification is done by using the 37 cm baby's head to have a greater number of patients who are labelled as being True Negatives having a maximal head deformation as 15 mm. That leads to a total number of 45 female patients instead of 12. This has to be done because otherwise a 5-fold cross validation test would not be possible as not enough True Negative patients were available to ensure that every of the required five sets $P_{i \in \{0 \ldots 4\}}$ have True Positives and True Negatives as the patients are distributed randomly.

While $\mu_{Standard,LR}$ is being generated by using Logistic Regression, μ_{SVM} is derived with the help of the Support Vector Machine in R. The model $\mu_{Standard,SVM}$ is generated by using the standard linear kernel. The classification results for the two models $\mu_{Standard,LR}$ and $\mu_{Standard,SVM}$ are given in table 7.1. The actual figures giving the number of True/False Positives/Negatives are not presented in the table as they are averaged when the tests have been performed five times during a 5-fold

	Non-Standard Measurements				
	Accuracy	Sensitivity (TPR)	Specificity (TNR)	FPR	FNR
LR	86.9%	93.7%	65.0%	35.0%	6.3%
SVM	86.4%	93.7%	63.0%	37.0%	6.3%

Table 7.2: Classification measures for the new combined measurements using 80% for the model and 20% of the 200 female samples for testing. The tests have been performed using 5-fold cross validation.

cross validation test.

Classification values reveal that the accuracy values are higher for the model $\mu_{Standard,SVM}$, which has been generated by using the SVM. The same is true for the other values, like sensitivity and specificity. Specificity is about 8% higher because the FPR value is lower, classifying more True Negatives correctly than with the other model $\mu_{Standard,LR}$.

Using other kernels for the Support Vector Machine than the standard linear kernel did not improve the classification results, so all models are generated with the linear one.

Classification of Non-Standard Measurements

Beside the standard set, other measurements can be used as feature space to derive a model. From the proposed measurements in section 5.2 "New Measurements" of chapter 5 "Pelvimetric Survey", a set of measurements can be selected to define a new feature space. The combined measurements (see section 5.2.2 "Combined Measurements") BrimArea, BrimRatio and OutletArea are selected together with the curvature radius (see 5.2.1) to define the measurement set "Non-Standard" to see how well the new and refined measurements perform alone compared to the 14 standard ones. The resulting classification values for the respective models $\mu_{Non-Standard,LR}$ and $\mu_{Non-Standard,SVM}$ are given in table 7.2.

It can be seen that a model using the combined measurements as its feature space having four measurements has an accuracy of about 86%, compared to the standard measurements with an accuracy value of 87%. The sensitivity values are similar for the different feature spaces, but the specificity is lower compared to the values of the standard features.

7.3.2 Optimizing Features

By fitting the model using the training set M and optimizing the model to classify samples from M correctly, the model can be "over-fitted". As the example data in figure 7.4 (on page 111) are not linearly separable, a linear model is not usable to provide a correct classification for all the given samples. The model μ_i, which is represented by the decision function, is very well adjusted for the training set M, but it does not perform well in terms of generalization. So samples which are not part of the training set are misclassified. It shows that the decision model just uses the training set as a kind of a look-up table and has no further information for the input values in the general case, which are not part of the training set [CST00].

In a more general case the hypotheses will become too complex instead of being consistent for the use case they have been designed for. A possible resolution for this will be a parameter restriction for the feature space. But this will also lead to a non-perfect classification result again. So a trade-off between accuracy and generalization has to be made.

After a model μ_i has been fitted by using Logistic Regression, the samples from the test set T can be evaluated and the samples' respective labels can be tested to find out whether the outcome $\mu(\vec{x_i})$ matches the input label y_i.

Doing that the single elements of the parameter vector $\vec{\beta}$, representing the hyperplane H in Logistic Regression, can be qualified by using the Z-Value, which is defined as the ratio of the coefficient's value β_i and its respective standard-deviation σ_{β_i}:

$$Z_i = \frac{\beta_i}{\sigma_{\beta_i}} \tag{7.11}$$

Z-Value is a measure of the significance of that coefficient β_i and the pelvimetric measurement it represents. A parameter is defined to be significant if |Z-Value| is greater than 2 [HTF09].

Non significant parameters (having |Z-Value| $<$ 2) can be disregarded to reduce the parameter space, and the model can be fitted again to generate a new model m_{i+1}. To do that iteratively, the parameter with the lowest absolute |Z-Value| $<$ 2 will be omitted and the fitting process will be redone. If no non-significant elements are available in the parameter vector β, the model cannot be reduced even further and the optimization terminates.

In algorithm 9 this iteration procedure is given in pseudo code notation. The iteration loop is implemented by using a recursive call in line 10 where the method

Algorithm 9 Feature Optimization

C set of classification results, $\vec{\beta}$ current parameter configuration
M training set, T test set

OptimizeFeatures($C, \vec{\beta}, M, T$):
1: **if** (Contains($C, \vec{\beta}$)):
2: **return**

3: $\mu_{LR} \leftarrow$ FitLogit(BirthScore $\sim \vec{\beta}$, M)

4: $N \leftarrow$ NonSignificantParameters(μ_{LR})
5: **if** ($N = \emptyset$):
6: $C[\beta] \leftarrow$ TestSamples(μ_{LR}, T)
7: **return**

8: $\beta_N \leftarrow$ LeastSignificantParameter(N)
9: $\vec{\beta^*} \leftarrow \vec{\beta} \setminus \{\beta_N\}$
10: OptimizeFeatures(C, $\vec{\beta^*}, M, T$)

	Best4 Measurements				
	Accuracy	Sensitivity (TPR)	Specificity (TNR)	FPR	FNR
LR	88.9%	94.8%	67.8%	32.2%	5.2%
SVM	90.4%	97.4%	65.5%	34.5%	2.6%

Table 7.3: Classification measures for the minimal parameter set having the maximal accuracy value.

OptimizeFeatures is called for the reduced parameter set. And so the $\vec{\beta^*} := \vec{\beta}\setminus\{\beta_N\}$ will be calculated by removing the least significant parameter β_i before the recursive invocation. Classification results that show how well the current model classifies T are stored in set C (line 6). This set is also used for some bookkeeping to prevent the same configuration from being computed all over again (line 1). During the initial call the set is defined to be $C = \emptyset$.

After the execution a set of all possible and significant parameter configurations and their respective classification results is available.

More details of how the model is tested and how the routine TestSamples actually tests the samples by using the model is given in section 7.3 "Model Evaluation". An overview of the measurements' definitions is given in figure 7.6.

The minimal parameter set having the tested maximal accuracy value is defined by four measurements: "BrimRatio", "Dist. Interspinalis", "Diam. Transversalis" and "Conjugata Diagonalis". The ratio of the pelvic entry has no unit and encodes

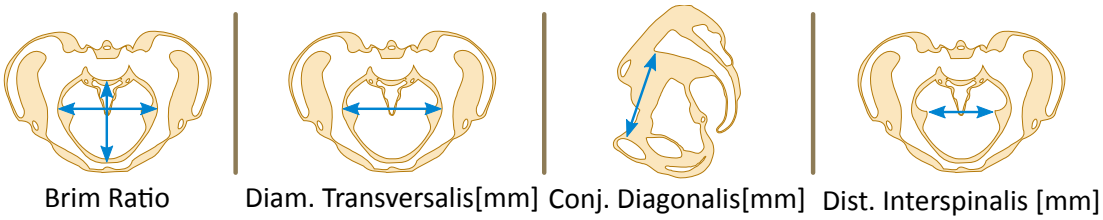

Figure 7.6: Measurements which are used to derive a model $\mu_{Best4,LR}$ with the minimal feature count and the maximal accuracy.

the shape of the pelvic entry. A value close to 1 represents a circular shape and resembles a more “Gynecoid” pelvis. “Anthropoid“ pelvises have a ratio greater than 1 whereas ”Platypelloid“ pelvises have values between 0 and 1. The pelvis classification has been presented in figure 1.4 in section 1.1.2 “Pelvic Bone” of chapter 1 “Introduction” on page 4. The required scales of the diameter are provided by the ”Diam. Transversalis“ and “Conjugata Diagonalis”. So these two measurements are also necessary for the model. The ”Dist. Interspinalis“ is a measurement which provides information about the pelvic exit.

By using these four measurements a new feature space called “Best4” can be defined and used for modeling $\mu_{Best4,LR}$ and $\mu_{Best4,SVM}$. The classification values are given in table 7.3. An accuracy of 90.4% and a sensitivy value of 97.4% is revealed for $\mu_{Best4,SVM}$. Both values are higher than the ones for the Logistic Regression $\mu_{Best4,LR}$. The specificity and the error values FPR and FPN are similar.

7.4 Conclusion

With the help of algorithms like Logistic Regression and the Support Vector Machine (SVM), prediction models have been derived from the various pelvimetric measurements, forming the models' feature spaces. Together with the birth score as the required labeling information samples have been provided and used to learn the models.

The generated models have been evaluated by using a 5-fold cross validation test, and their generalization performance has been analyzed to get relevant classification results, which are required to compare the different models in an objective way.

To prevent over-fitting and finding the minimal parameter space, which consists of only significant measurements, a parameter optimization has been per-

	Accuracy	Sensitivity (TPR)	Specificity (TNR)	FPR	FNR
LR - Standard	86.6%	85.5%	90.5%	9.5%	14.5%
SVM - Standard	85.8%	85%	88.6%	11.4%	15%
LR - Best4	84.7%	83.7%	88.2%	11.8%	16.3%
SVM - Best4	81.8%	80.8%	85.5%	14.5%	19.2%

Table 7.4: Classification measures using a balanced training set with randomly chosen female patients.

formed. A parameter space of four measurements has been identified. Its respective model $\mu_{Best4,SVM}$ has an accuracy value of 90.4%, whereas the corresponding model $\mu_{Best4,LR}$, which has been derived by using the Logistic Regression, has a lower accuracy value. See table 7.3 in section 7.3.2 "Optimizing Features" for the actual values.

The same performance of the algorithms can be seen for the standard measurements, which have been analyzed and presented in table 7.1. Here, the FPR_{SVM} is 8% smaller than the FPR_{LR}, which represents the rate of False Positives - the patients who have a bad birth score - and who are classified as having a good one. In actual values FPR_{SVM} is 22% and the FNR_{SVM} is 5.8% showing that more of the patients with a bad birth score are misclassified than the other way round.

Having a look at the female samples and using the head deformation values for the 37 cm head, it is obvious that from 201 female patients 156 patients are defined to be non-problematic, as they are labelled positively, and only the remaining 45 patients tend to have complications during a vaginal birth, as they have a higher maximal head deformation during the simulation.

To see whether the bias between the error rates (FPR and FNR) could be changed by adjusting the training set, an experiment was done. A more balanced training set has been defined. As there are only 45 female patients who were identified as having complications during a vaginal delivery, the overall patient count has to be reduced to equalize the element count of the two sets. Only 45 female patients should be randomly selected from the overall 156 patients, who are defined to be non-problematic. The final training set consists of 90 patients of two classes. Each class has the same patient count of 45.

After fitting the respective models and testing the classification performance it can be seen that the relevant error values FPR and FNR have been decreased and the differences between them are reduced, showing a more balanced classification. The accuracy values are now 86.6% for the Logistic Regression and 85.8% using the SVM and the 14 standard measurements. The classification results for the

standard set are presented along with the values for the minimal parameter set of four measurements (Best4) in table 7.4.

For a future evaluation, the models and their classification performance can be improved by collecting more relevant data. As more females with a problematic birth outcome are required for such a model, such data have to be collected for further evaluations. The reduction of True Positives in the example for the new training set has led to a more balanced classification model.

In summary, models for the prediction of obstructed labor have been derived. The models have different feature spaces and a maximal accuracy of 90.4% for the 14 standard measurements and the Best4 measurements as the selected features spaces. The SVM was used to generate these models. Using Logistic Regression, the values were 87.4% and 88.9% for the two measurement sets. All these models showed high sensitivity, but a relatively low specificity. The reason for this can be seen in the relatively high FPR (False Positive Rate) values, which led to a low specificity compared to the sensitivity which is related to the FNR (False Negative Rate).

Higher specificity values and more balanced models can be derived using a more balanced training set. The models derived from such a training set have more equalized specificity and sensitivity values. The specificity could be increased up to 21.3% for the standard measurements and using Logistic Regression, which is now 90.5% compared to 69.2% in table 7.1 when using the non-balanced training set. The same is true for the SVM and the Best4 measurements. The specificity is now 20% higher than the former 65.5%. The balanced model $\mu_{Best4,SVM}$ has 85.5%.

But the accuracy values are lower because only 90 patients were used instead of the total of 201 females for model fitting and evaluation. Having this in mind, more problem specific data have to be collected so that the number of women who are likely to have complications during a vaginal delivery could be increased and more patients could be available for fitting and deriving such a prediction model.

It has been shown that the pelvimetric measurements and the classification based on the maximal head deformation from the virtual delivery simulation is possible and has led to potentially usable models for predicting obstructed labor.

Chapter 8

Conclusion and Future Work

In the previous chapter (see chapter 7 “Prediction Model”) algorithms from machine learning were used to generate mathematical models which are able to predict the indication of obstructed labor and to answer the question whether a vaginal delivery is theoretically possible. To generate such a prediction model various data have been used. The required feature spaces are based on the pelvimetric measurements, which are performed and evaluated by using the presented Mapped CAD System (see chapter 3 “Mapped CAD System”) in an efficient, reliable and deterministic way. The shape analysis of chapter 6 “Shape Analysis” examined the pelvic bone models and clarified how they differ from patient to patient. With such an analysis it was possible to generate mean bones and identify regions which are promising enough to define more predictive measurements and disregard those in uninteresting - very common - areas of the pelvic surface.

The PDM-Analysis provided a deeper insight of how the pelvis shape models differ and which geometrical variations exist in the provided data. With the PDM space and modes, possible ranges of geometrical variations are found and can be used by medical experts to investigate the pelvic anatomy even further.

Beside the pelvimetric measurements, a virtual delivery simulation was presented in chapter 4 “Delivery Simulation”. With the geometrically based simulation a birth trajectory for a baby’s head and a patient’s pelvis has been computed. Along that trajectory the head deformation was determined and recorded. This gathered simulation data have been used in the statistical analysis in chapter 5 “Pelvimetric Survey”. In the presented statistical evaluations, a birth score was defined and compared to the already existing indices from medical literature. This birth score is based on the maximal head deformation and is the relevant criterion for the actually required labeling of the model generation. A label marks

a female person either as having no indications for a problematic delivery or as having a problematic one.

Together with the pelvimetric measurements as the feature space this labelling information forms the training set which is necessary to derive the various prediction models. The models were generated via two different algorithms, namely Logistic Regression and Support Vector Machine, and were classified by using a 5-fold cross validation technique. Also an optimization has been performed to identify a minimal set of measurements that have the most significance. The classification results of the various models are presented in detail in the previous chapter. Generated models have an accuracy value of about $87\% - 90\%$, but they have shown relatively high FPR (False Positive Rate). That led to a high sensitivity but a low specificity value for the models. Good models have high percentage values in sensitivity and specificity and provide a high accuracy in their classification performance.

To examine this phenomenon even further, an experiment has been done to generate a special, more balanced training set with an equal patient count for both labels. The more balanced training set had only 90 patients compared to the 201 patients. The models that were derived by using such a balanced training set showed a more balanced error rate, since the FPR and FNR values were smaller and more equal to each other, compared to previous models. Such low rates also led to higher specificity and sensitivity values.

The data which have been used and generated within this thesis are based on virtual pelvis models which are collected and managed within the presented bone database (see chapter 2 “Bone Database”). Such pelvic bone models have been generated from medical data, which have been collected anonymously and in the patients’ consent from Klinikum Rechts der Isar and from Stryker Corp. These pelvises have been originally used in third party founded projects to improve orthopaedic plates for fracture treatment. Within such data, female patients are available who might not be relevant for a gynaecological study. For such a survey, only women at the age of 18-50 years are of interest, but some older female patients are also taken into account in the used data. Another example is that different ethnic groups were used together whereupon it is known that different ethnic groups have different risk rates for various complications during a vaginal delivery. They had been integrated to have a larger data foundation, which was necessary to generate the prediction models with a larger training set and validate them with a 5-fold cross validation test. Otherwise it would not be

possible to distribute the True Positive and True Negative examples randomly in the five training sets during the validation process. It is necessary that all sets contain enough patients of the two classes. A set with only patients of one class cannot be used to train a model.

Furthermore the data collection, generation and analysis have been done only in the virtual world and cover only the green enclosed part in the approach of systems biology visualized in fig. 8.1. What lacks is the right part in this schematic overview, which is marked in violet and named "real", representing the real world (in vitro/in vivo).

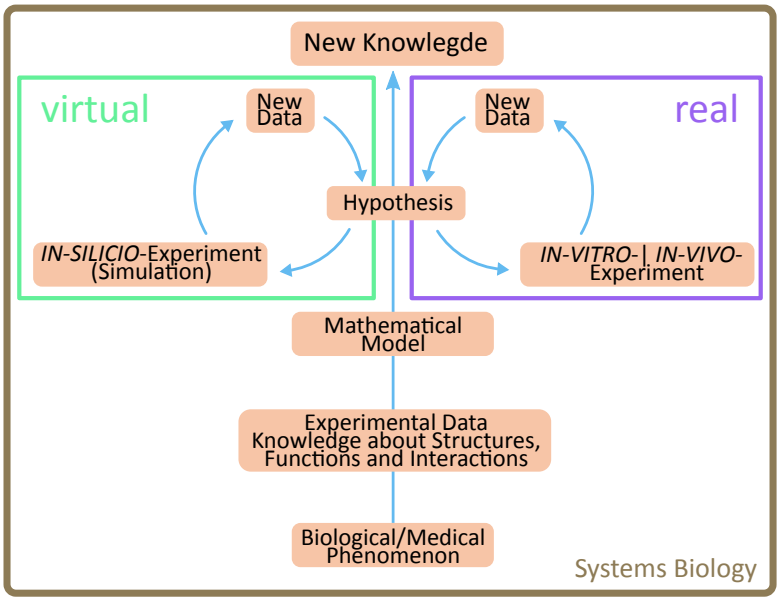

Figure 8.1: Schematic overview of Systems Biology marked both virtual experiments(green) and experiments in the real world (violet).

To overcome that, more clinical data have to be collected which is more focused on a gynaecological study than the data already collected. This means more female pelvises from women who gave birth and real data about their children - especially the relevant measures of the babys' heads - have to be collected. In addition, the female's parity is important and had to be added to the meta data. The parity counts how many times a female person has given birth. A woman who had never given birth is regarded as nulliparous. A primiparous woman has given birth one time and a multiparous one has given birth two or more times. Another important meta data are the diagnostic findings of the women, whether they had indications of Fetal Pelvic Disproportions before the delivery or not. If a vaginal delivery was tried or a caesarean section was done prophylactically instead. If a sectio was done prophylactically, no one knows whether a vaginal delivery would have been possible after all. The most interesting women for such a study are women who

had a sectio after a failed vaginal delivery and question they had had indications of Fetal Pelvic Disproportions beforehand.

Beside the pelvic and fetal measurements, data of real vaginal deliveries and about how the baby's head wanders through the parturient canal within the inner pelvis are of interest, too. It would help a lot to record real trajectories of a fetal head during a vaginal delivery. This real trajectories could be used to verify and optimize the presented virtual delivery algorithm from chapter 4 "Delivery Simulation".

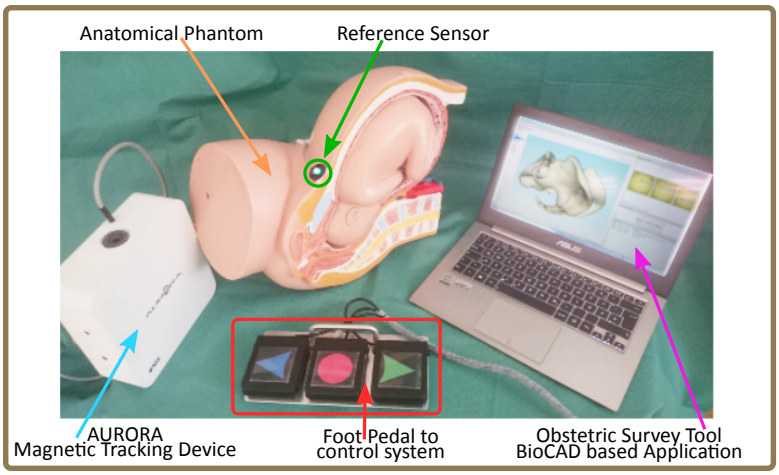

Figure 8.2: Test setup for the Obstetric Survey Tool to generate real data within a clinical environment.

To record such real data, a system for gynaecological examinations has been developed in our research group, which can be used during a clinical examination on real parturients in the delivery room. The system is controlled by a special software called "Obstetric Survey Tool" (OST), which is implemented with the BioCAD framework and which uses a clinical real-time electromagnetic tracking system (Aurora [1] from NDI) to measure the pose of a 5 DOF coil sensor - which has to be positioned on an obstetrician's finger tip below a pair of gloves - relatively to a reference sensor - which has been positioned on the mother's pubis. With the help of the finger sensor, which had been fixated below the gloves due to hygienic reasons and to keep sterility, the fetal head can be touched and in some way scanned by the finger tip's sensor to provide a point cloud for every station. The software uses a registration pose to record the tracked point cloud and therefore the fetal's station information in relation to mother's 3D model pelvis in an exact way. The software is controlled by the obstetrician within the delivery room via a specially constructed foot pedal to retain sterility. By using the foot pedal no

[1] Aurora - clinical real-time electromagnetic tracking system from NDI medical, 2015-05-12, *http://www.ndigital.com/medical/products/aurora/*

manual interaction is required at all. Furthermore, the software provides hints and feedback via screen and text-to-speech output. The sterile fingers are not required for data input and the obstetrician can focus on the patient's examination.

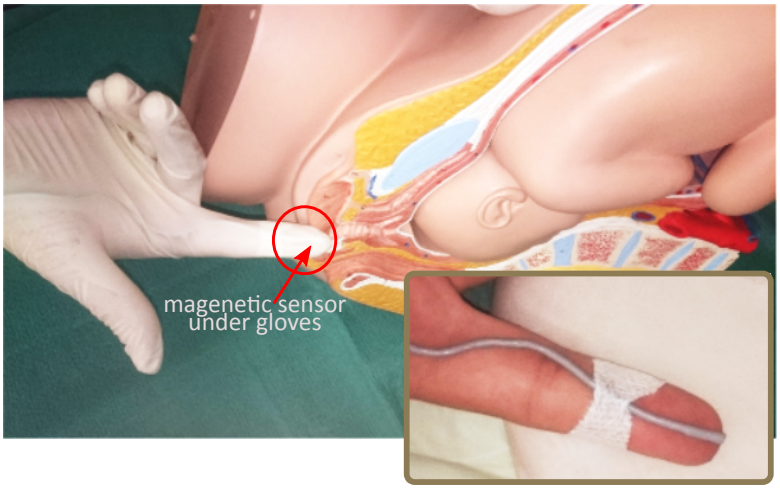

Figure 8.3: Recording station data during a vaginal birth using a 5 DOF sensor coil fixated on the finger tip.

Figure 8.2 shows the setup of the Obstetric Survey Tool with its components exemplified using an anatomical phantom, whereas figure 8.3 shows how the 5 DOF (three positional and two rotational) sensor coil is fixated on a finger tip below a pair of gloves to measure the fetal head's pose and shape during a vaginal delivery exemplified on an anatomical phantom.

But the Obstetric Survey Tool cannot only be used to record the interesting trajectories during a vaginal delivery, it can also be used as a more modern pelvimeter to measure distances and other related data beside techniques such as ultrasound. This would help to find new measures from outside which correlate with the inner features. Inner features are derived via ultrasound imaging, MR scans or the CT datasets used in the bone database for the pelvimetric measurements. Outer or external features can be recorded during a normal medical examination via palpation or a more modern pelvimeter like the OST. Such outer measurement can possibly replace the inner ones, which helps a lot because such values can be derived even simpler, easier and in a more precise and reliable way without using all the complicated and expensive medical imaging techniques such as MR. CT and X-ray are forbidden during pregnancy.

In the future, gynaecologists will have to take over and they will have to collect more real and focused data. Such data are either the described meta data of mother and child and the real recorded trajectories via the OST. With such a real data library it will then be possible to define more accurate and

reliable indices. This would significantly improve the classification performance of generated prediction models. Maybe, with such statistical and computational models it will be possible to find the most relevant features which are necessary for a better risk analysis, so that the overall count of obstructed labor is further reduced and a reliable prediction of a gentle delivery is possible.

Appendix A

Pelvimetric Measurements

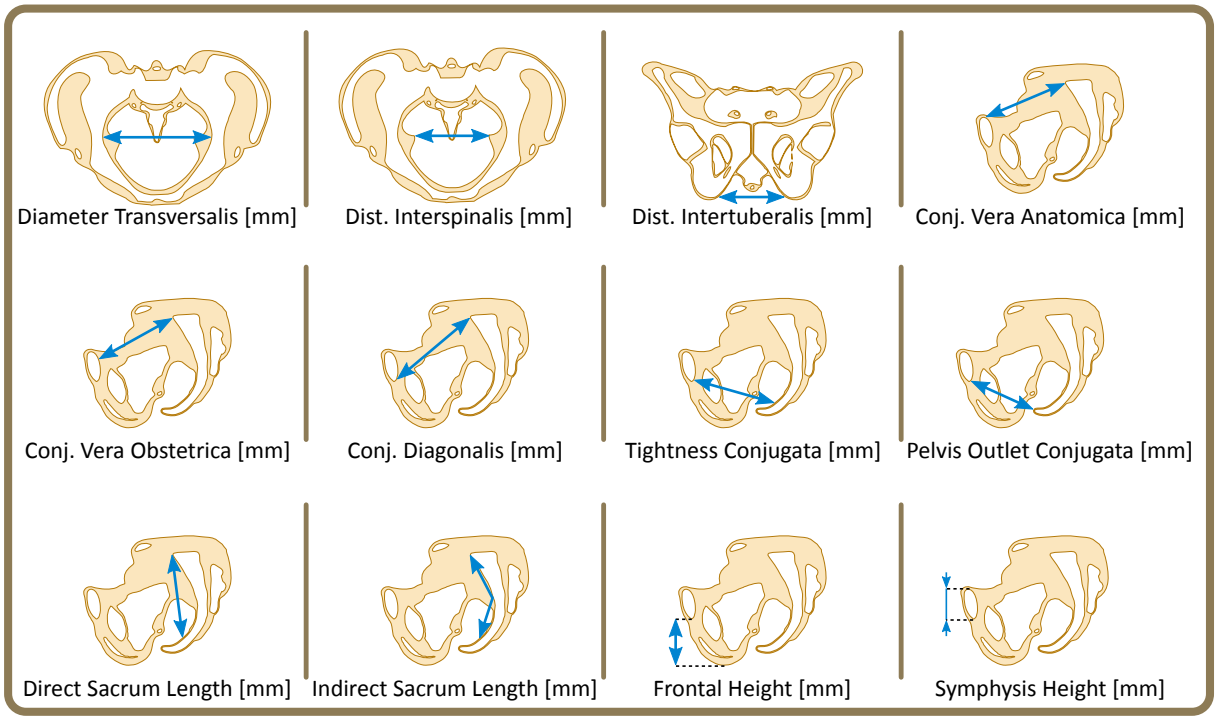

Figure A.1: A list of pelvimetric distance measurements used in Anapelvis.

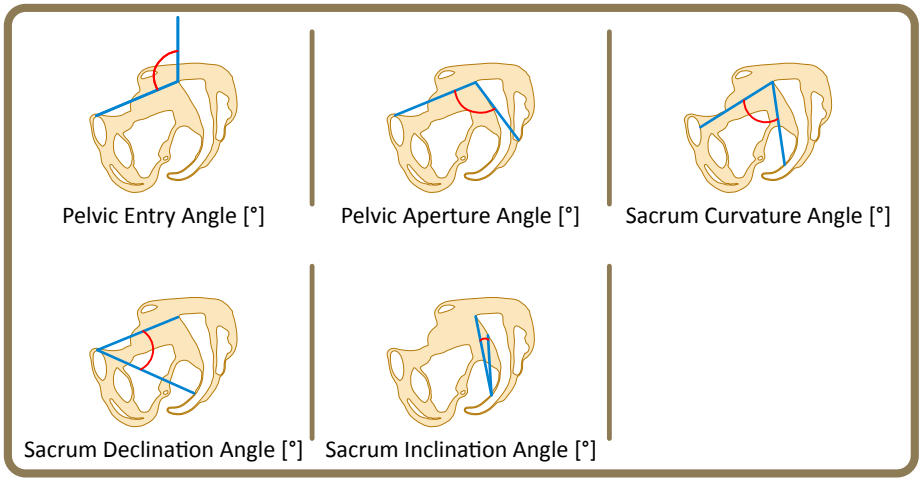

Figure A.2: A list of pelvimetric angular measurements used in Anapelvis.

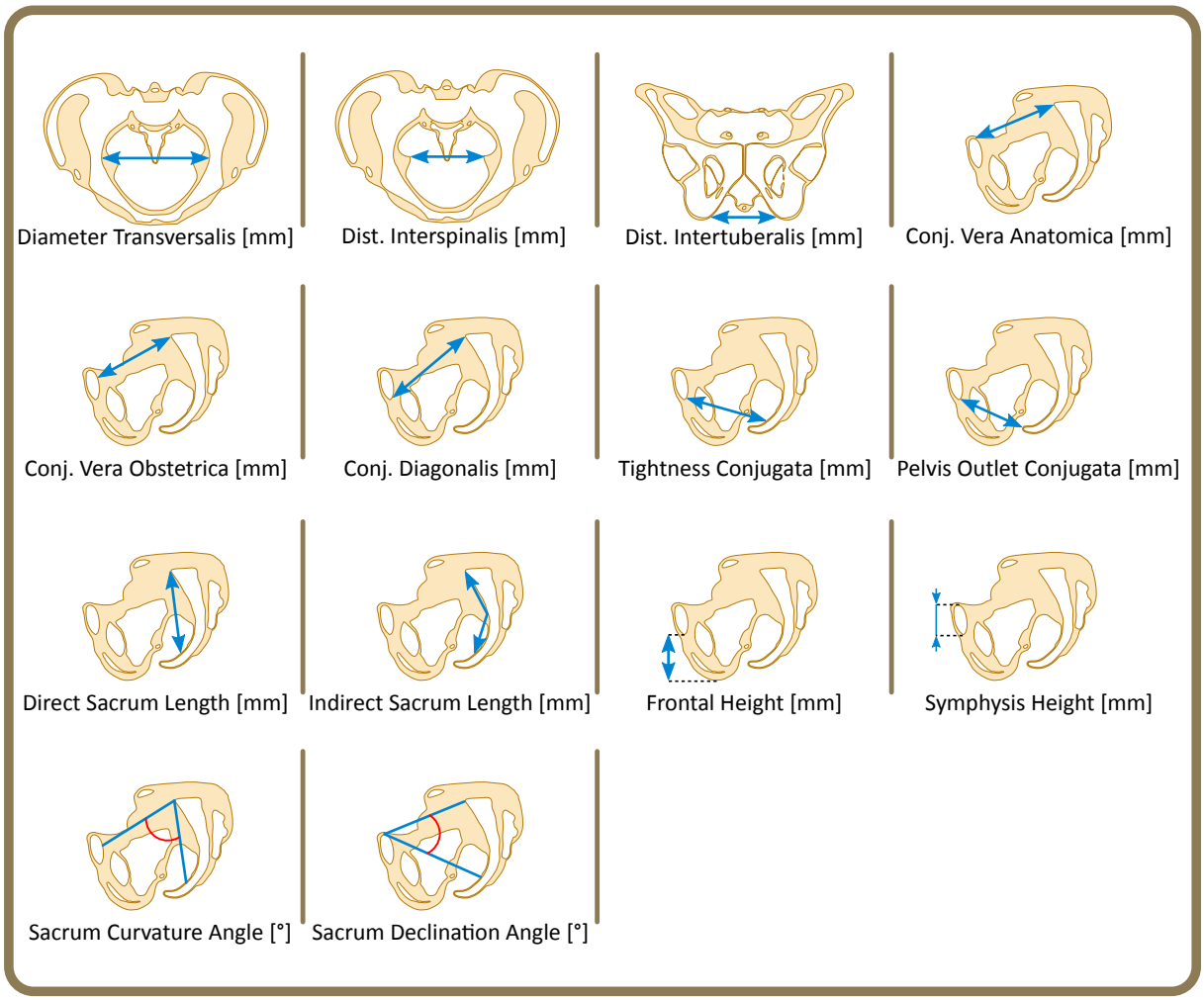

Figure A.3: A list of the 14 pelvimetric standard measurements used in this thesis.

Appendix B

Simulation Results

Total Patients		526	Female	206	Male	320
	Deform <= [mm]	Patients	Female	Female [%]	Male	Male [%]
	0	25	24	11,65	1	0,31
	1	44	43	20,87	1	0,31
	2	55	54	26,21	1	0,31
	3	75	73	35,44	2	0,63
	4	94	89	43,20	5	1,56
	5	115	105	50,97	10	3,13
	6	138	124	60,19	14	4,38
	7	153	136	66,02	17	5,31
	8	176	154	74,76	22	6,88
	9	196	162	78,64	34	10,63
	10	210	172	83,50	38	11,88
	11	228	178	86,41	50	15,63
	12	250	185	89,81	65	20,31
	13	269	190	92,23	79	24,69
	14	287	193	93,69	94	29,38
C	15	311	194	94,17	117	36,56
	16	333	196	95,15	137	42,81
	17	360	200	97,09	160	50,00
	18	377	201	97,57	175	54,69
	19	392	202	98,06	189	59,06
	20	416	205	99,51	210	65,63
	25	482	205	99,51	276	86,25
	30	515	206	100,00	308	96,25
D	> 30	12	0	100,00	12	100,00

Table B.1: An overview over the simulated head deformations using the standard 35cm baby model.

Appendix C

Pelvimetric Statistics

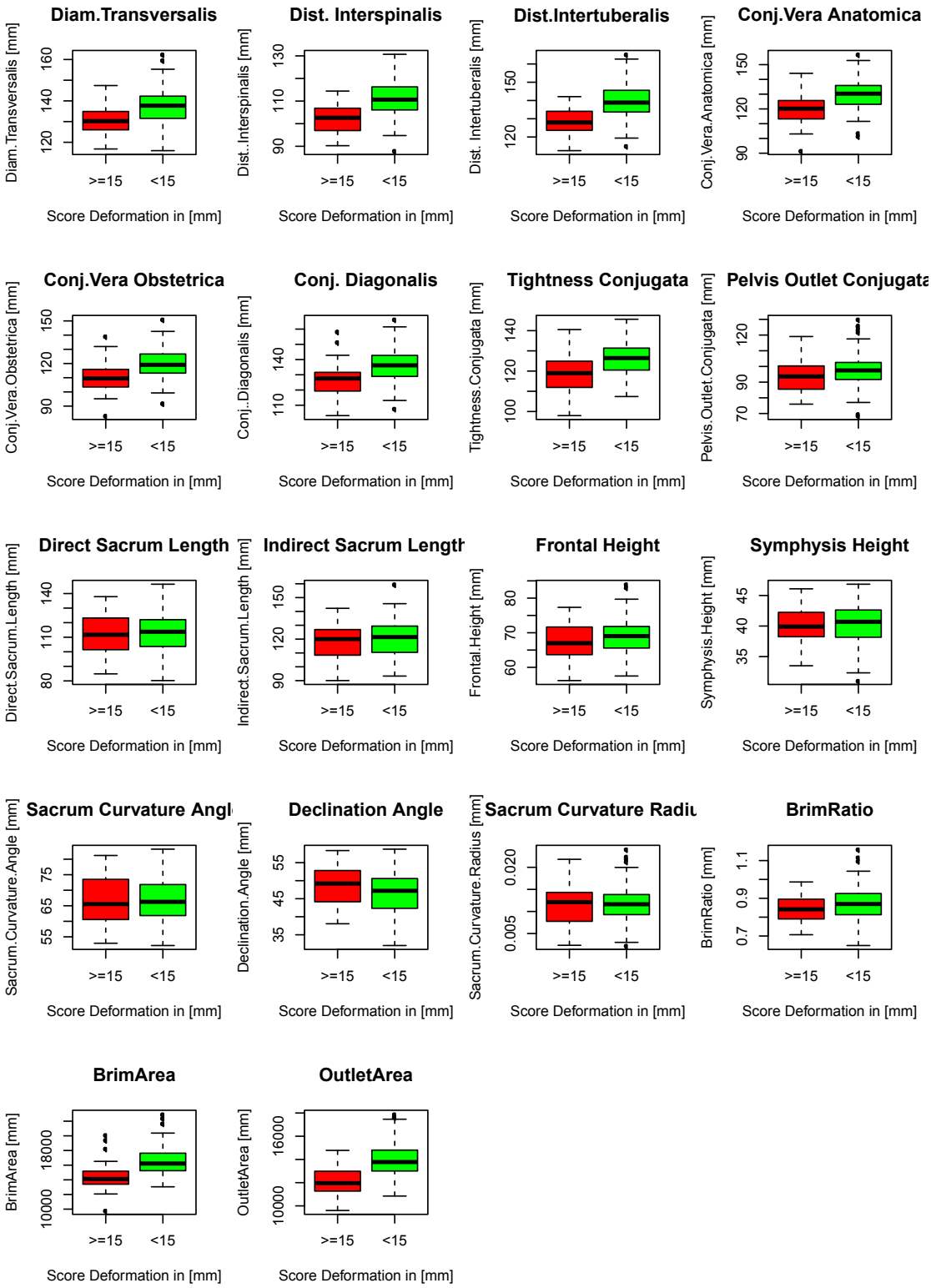

Figure C.1: Box Plot for all of the 14 standard pelvimetric measurements.

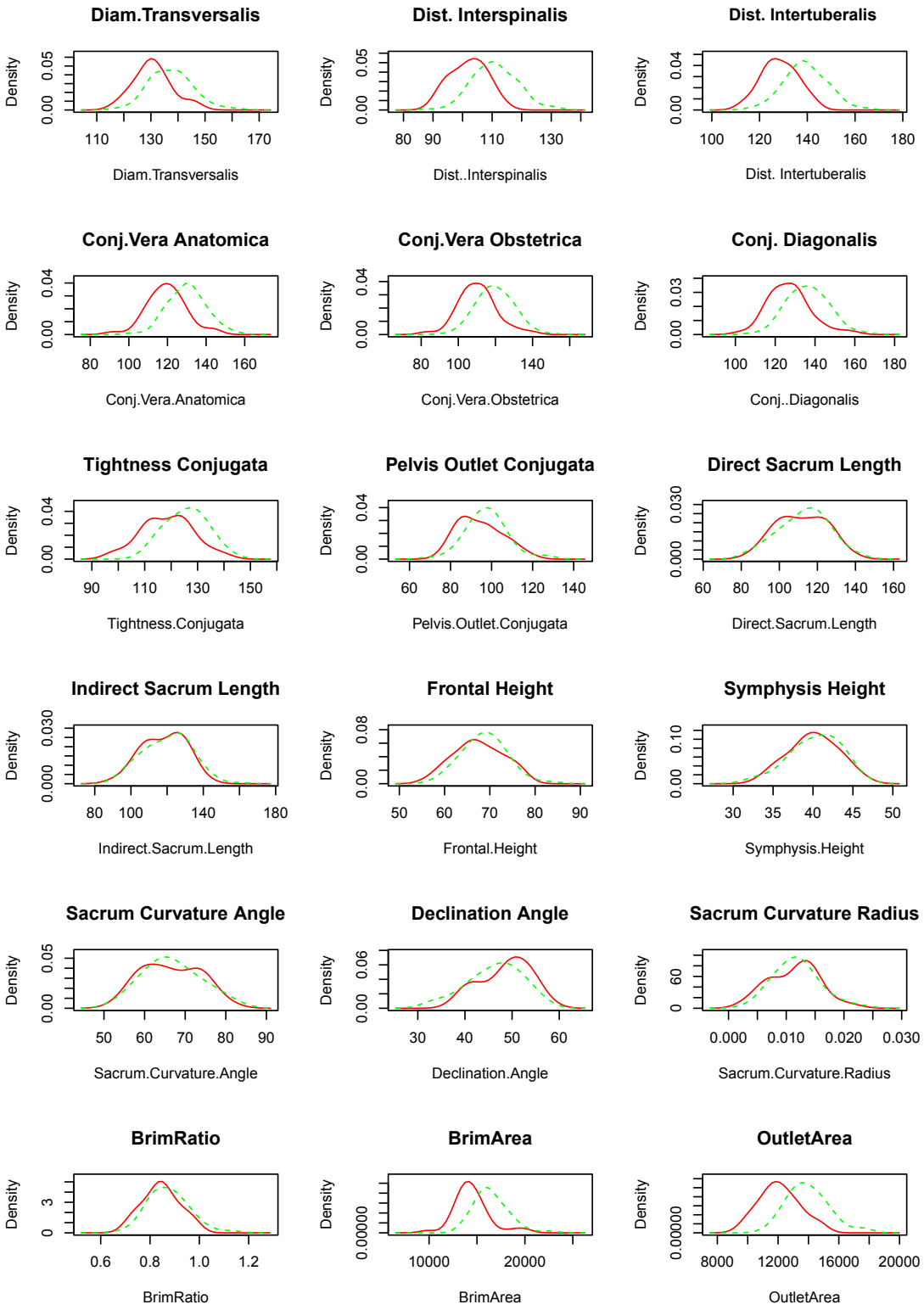

Figure C.2: Density Plot for all of the 14 standard pelvimetric measurements.

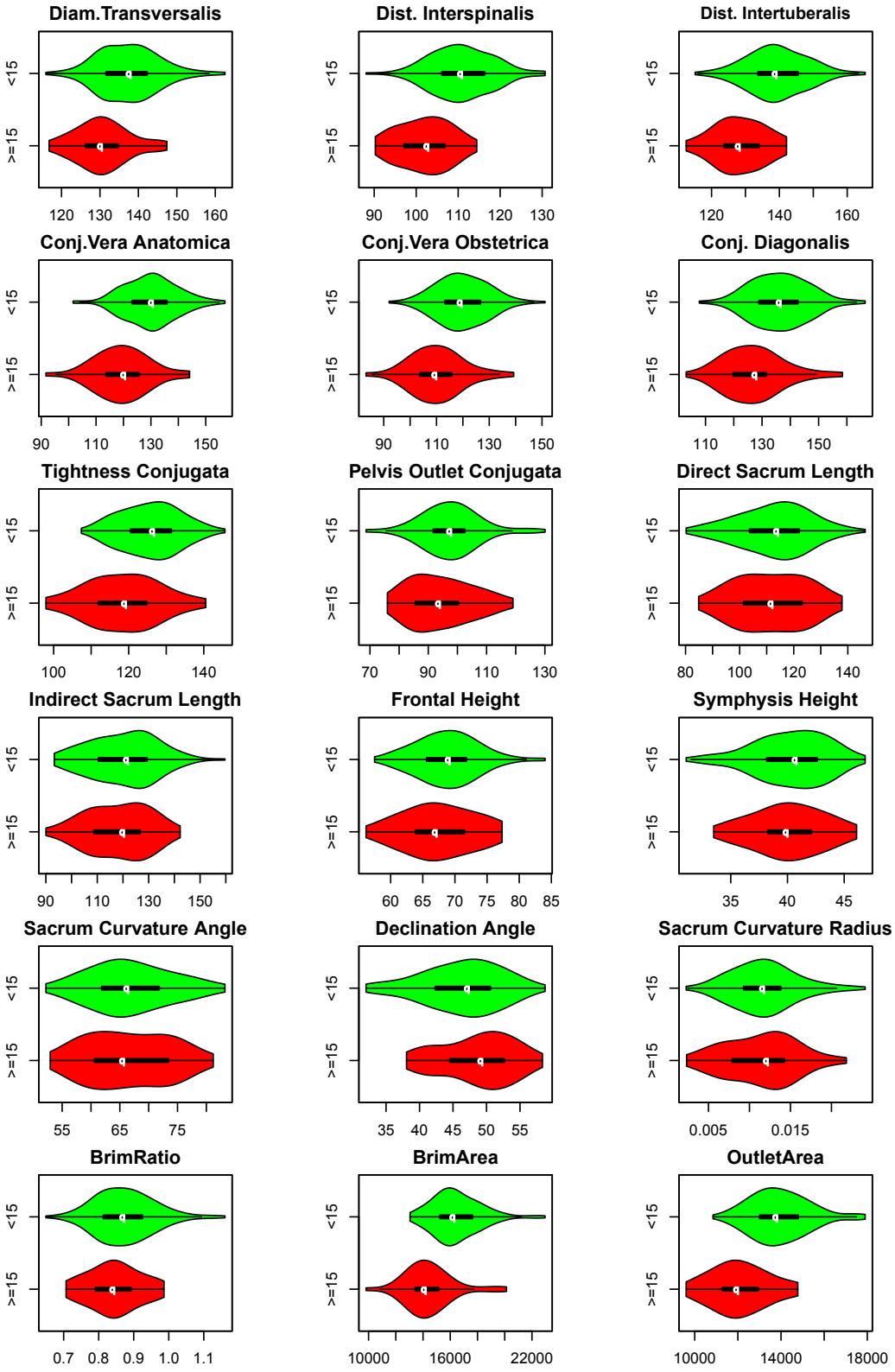

Figure C.3: Violin Plot for all of the 14 standard pelvimetric measurements.

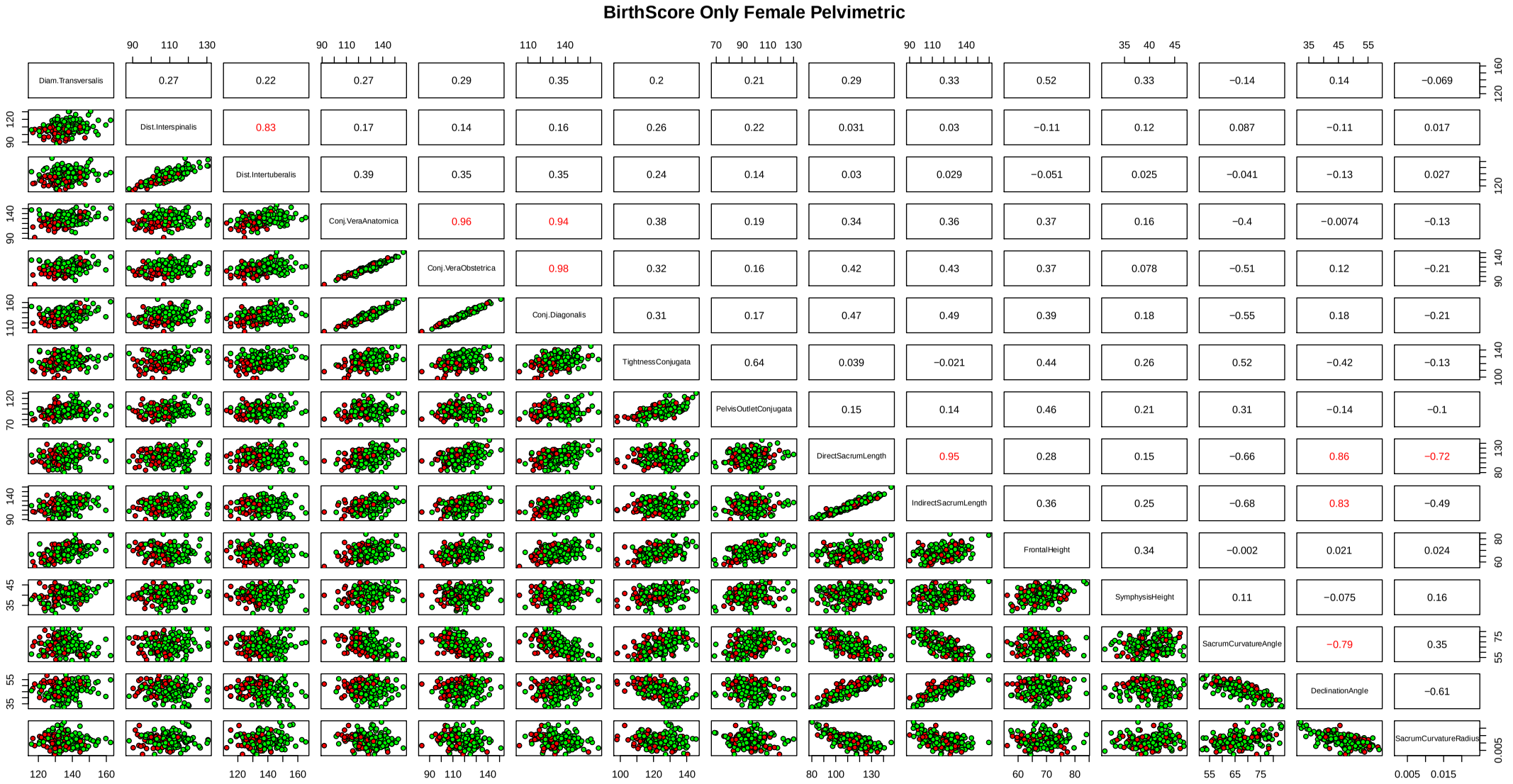

Figure C.4: Scatter Plot for all of the 14 standard pelvimetric measurements and “Sacrum Curvature Radius”.

Bibliography

[BA02] J. A. Bærentzen and H. Aanæs, *Computing discrete signed distance fields from triangle meshes*, Tech. report, Informatics and Mathematical Modelling, Technical University of Denmark, DTU, Richard Petersens Plads, Building 321, DK-2800 Kgs. Lyngby, 2002.

[Bis06] Christopher M. Bishop, *Pattern Recognition and Machine Learning (Information Science and Statistics)*, Springer-Verlag New York, Inc., 2006.

[BV04] C. S. Blackadar and A. J. Viera, *A retrospective review of performance and utility of routine clinical pelvimetry*, Fam Med **36** (2004), no. 7, 505–507.

[CLB+09] F. Cunningham, K. Leveno, S. Bloom, J. Hauth, D. Rouse, and C. Spong, *Williams Obstetrics: 23rd Edition: 23rd Edition*, McGraw-Hill's AccessMedicine, McGraw-Hill Education, 2009.

[CST00] N. Cristianini and J. Shawe-Taylor, *An Introduction to Support Vector Machines and Other Kernel-based Learning Methods*, Cambridge University Press, 2000.

[CT04] T.F. Cootes and C.J. Taylor, *Statistical Models of Appearance for Computer Vision*, 2004.

[Deu10] Deutscher Hebammenverband (Hrsg.)HV, *Das Neugeborene in der Hebammenpraxis*, Hippokrates, 2010.

[DMSB99] Mathieu Desbrun, Mark Meyer, Peter Schröder, and Alan H. Barr, *Implicit Fairing of Irregular Meshes Using Diffusion and Curvature Flow*, Proceedings of the 26th Annual Conference on Computer Graphics and Interactive Techniques (New York, NY, USA), SIGGRAPH '99, ACM Press/Addison-Wesley Publishing Co., 1999, pp. 317–324.

[Faw06] Tom Fawcett, *An introduction to ROC analysis*, Pattern Recognition Letters **27** (2006), no. 8, 861 – 874, ROC Analysis in Pattern Recognition.

[FND+98] J. E. Ferguson, Y. G. Newberry, G. A. Deangelis, J. J. Finnerty, S. Agarwal, and E. Turkheimer, *The fetal-pelvic index has minimal utility in predicting fetal-pelvic disproportion.*, American Journal of Obstetrics & Gynecology **179** (1998), no. 5, 1186.

[GH97] Michael Garland and Paul S. Heckbert, *Surface Simplification Using Quadric Error Metrics*, Proceedings of the 24th Annual Conference on Computer Graphics and Interactive Techniques (New York, NY, USA), SIGGRAPH '97, ACM Press/Addison-Wesley Publishing Co., 1997, pp. 209–216.

[GHL04] Sylvestre Gallot, Dominique Hulin, and Jacques Lafontaine, *Riemannian Geometry (Universitext)*, Springer, 2004.

[GSR+10] H. Gottschling, M. Schröder, N. Reimers, F. Fischer, A. Homeier, and R. Burgkart, *A System for Performing Automated Measurements on Large Bone Databases*, World Congress on Medical Physics and Biomedical Engineering, September 7 - 12, 2009, Munich, Germany (Olaf Dössel and WolfgangC. Schlegel, eds.), IFMBE Proceedings, vol. 25/4, Springer Berlin Heidelberg, 2010, pp. 910–913 (English).

[HD07] L. HOYTE and M. S. DAMASER, *Magnetic Resonance-Based Female Pelvic Anatomy as Relevant for Maternal Childbirth Injury Simulations*, Annals of the New York Academy of Sciences **1101** (2007), no. 1, 361–376.

[HDW+08] L. Hoyte, M. S. Damaser, S. K. Warfield, G. Chukkapalli, A. Majumdar, D. J. Choi, A. Trivedi, and P. Krysl, *Quantity and distribution of levator ani stretch during simulated vaginal childbirth*, Am. J. Obstet. Gynecol. **199** (2008), no. 2, 1–5.

[Hop99] Hugues Hoppe, *New Quadric Metric for Simplifying Meshes with Appearance Attributes*, Proceedings of the 10th IEEE Visualization 1999 Conference (VIS '99) (Washington, DC, USA), VISUALIZATION '99, IEEE Computer Society, 1999.

[HPM06] Xiaolei Huang, Nikos Paragios, and Dimitris N. Metaxas, *Shape Registration in Implicit Spaces Using Information Theory and Free Form Deformations*, IEEE Trans. Pattern Anal. Mach. Intell. **28** (2006), no. 8, 1303–1318.

[HTF09] Trevor Hastie, Robert Tibshirani, and Jerome Friedman, *The Elements of Statistical Learning (Springer Series in Statistics)*, Springer-Verlag New York, Inc., 2009.

[JvdHdB03] Štěpán Janda, Frans C.T van der Helm, and Sjoerd B de Blok, *Measuring morphological parameters of the pelvic floor for finite element modelling purposes*, Journal of Biomechanics **36** (2003), no. 6, 749–757.

[KS98] R. Kimmel and J. A. Sethian, *Computing geodesic paths on manifolds*, Proceedings of the National Academy of Sciences **95** (1998), no. 15, 8431–8435.

[KSHZ04] Alexandros Karatzoglou, Alex Smola, Kurt Hornik, and Achim Zeileis, *Kernlab - An S4 package for Kernel methods in R*, J. Stat. Softw (2004), 1–20.

[KSL+10] U. Korhonen, R. Solja, J. Laitinen, S. Heinonen, and P. Taipale, *MR pelvimetry measurements, analysis of inter- and intra-observer variation*, European Journal of Radiology **75** (2010), no. 2, e56–e61.

[KTH13] Ulla Korhonen, Pekka Taipale, and Seppo Heinonen, *Assessment of Bony Pelvis and Vaginally Assisted Deliveries*, ISRN Obstetrics and Gynecology **2013** (2013), 1–5.

[Lin07] Andreas Lindenberg, *Statistik macchiato : Cartoon-Statistikkurs für Schüler und Studenten*, Pearson Studium, München Boston u.a, 2007.

[LJW+10] Miriam S. Lenhard, Thorsten R.C. Johnson, Sabine Weckbach, Konstantin Nikolaou, Klaus Friese, and Uwe Hasbargen, *Pelvimetry revisited: Analyzing cephalopelvic disproportion*, European Journal of Radiology **74** (2010), no. 3, e107–e111.

[MPP+07] J. A. Martins, M. P. Pato, E. B. Pires, R. M. Jorge, M. Parente, and T. Mascarenhas, *Finite element studies of the deformation of the pelvic floor*, Ann. N. Y. Acad. Sci. **1101** (2007), 316–334.

[MWW02] Martin Meininger, Thomas Werner, and Arthur Wischnik, *Dreidimensionale Simulation und Visualisierung des individuellen menschlichen Geburtsvorganges*, Bildverarbeitung für die Medizin 2002 (Monika Meiler, Dietmar Saupe, Frithjof Kruggel, Heinz Handels, and ThomasM. Lehmann, eds.), Informatik aktuell, Springer Berlin Heidelberg, 2002, pp. 157–159 (German).

[PBM01] Albrecht Pfleiderer, Meinert Breckwoldt, and Gerhard Martius, *Gynäkologie und Geburtshilfe. Sicher durch Studium und Praxis.*, Thieme, Stuttgart, 2001.

[PNJM+10] M. P. Parente, R. M. Natal Jorge, T. Mascarenhas, A. A. Fernandes, and A. L. Silva-Filho, *Computational modeling approach to study the effects of fetal head flexion during vaginal delivery*, Am. J. Obstet. Gynecol. **203** (2010), no. 3, 1–6.

[Pow11] David Martin Ward Powers, *Evaluation: from precision, recall and F-measure to ROC, informedness, markedness and correlation*, International Journal of Machine Learning Technology **2** (2011), no. 1, 37–63.

[RDPB+83] J. E. Rossouw, J. P. Du Plessis, A. J. Benade, P. C. Jordaan, J. P. Kotze, P. L. Jooste, and J. J. Ferreira, *Coronary risk factor screening in three rural communities. The CORIS baseline study*, S. Afr. Med. J. **64** (1983), no. 12, 430–436.

[RSH+99] D. Rueckert, L.I. Sonoda, C. Hayes, D.L.G. Hill, M.O. Leach, and D.J. Hawkes, *Nonrigid registration using free-form deformations: application to breast MR images*, Medical Imaging, IEEE Transactions on **18** (1999), no. 8, 712–721.

[Rus04] Szymon Rusinkiewicz, *Estimating Curvatures and Their Derivatives on Triangle Meshes*, Symposium on 3D Data Processing, Visualization, and Transmission, September 2004.

[SG02] Vitaly Surazhsky and Craig Gotsman, *High Quality Compatible Triangulations*, PROCEEDINGS OF 11TH INTERNATIONAL MESHING ROUNDTABLE, 2002, pp. 183–192.

[SGGM06] Avneesh Sud, Naga Govindaraju, Russell Gayle, and Dinesh Manocha, *Interactive 3D Distance Field Computation Using Linear Factorization*, Proceedings of the 2006 Symposium on Interactive 3D Graphics and Games (New York, NY, USA), I3D '06, ACM, 2006, pp. 117–124.

[SGR+14] Manuel Schröder, Heiko Gottschling, Nils Reimers, Matthias Hauschild, and Rainer Burgkart, *Automated Morphometric Analysis of the Femur on Large Anatomical Databases with Highly Accurate Correspondence Detection*, Open Medicine Journal **1** (2014), no. 1, 15–22.

[SHH+13] Timm Surup, Anna Hänler, Annika Homeier, Andreas Petersik, Geert von Oldenburg, and Rainer Burgkart, *Verfahren zur Referenzmodellerstellung für die Evaluierung CT-basierter Segmentierung des Kortikalis-Spongiosa-Überganges im Femur.*, Bildverarbeitung für die Medizin, 2013, pp. 259–264.

[SHS10] Henning Schneider, Peter-Wolf Husslein, and Karl-Theo M. Schneider, *Die Geburtshilfe (German Edition)*, Springer, 2010.

[SRN+03] Martin A. Styner, Kumar T. Rajamani, Lutz-Peter Nolte, Gabriel Zsemlye, Gábor Székely, Christopher J. Taylor, and Rhodri H. Davies, *Evaluation of 3D Correspondence Methods for Model Building*, Information Processing in Medical Imaging (Chris Taylor and J.Alison Noble, eds.), Lecture Notes in Computer Science, vol. 2732, Springer Berlin Heidelberg, 2003, pp. 63–75 (English).

[SSS09] M. Schünke, E. Schulte, and U. Schumacher, *Prometheus - Lernatlas der Anatomie: Innere Organe ; 118 Tabellen*, Prometheus, Thieme, 2009.

[VPBM01] Alex Vlachos, Jörg Peters, Chas Boyd, and Jason L. Mitchell, *Curved PN Triangles*, In Symposium on Interactive 3D Graphics, 2001, pp. 159–166.

[WNC05] Jigang Wang, Predrag Neskovic, and Leon N Cooper, *Training data selection for support vector machines*, ICNC 2005. LNCS, Springer, 2005, pp. 554–564.

[XZY10] Song-Gang Xu, Yun-Xiang Zhang, and Jun-Hai Yong, *A Fast Sweeping Method for Computing Geodesics on Triangular Manifolds*, IEEE Transactions on Pattern Analysis and Machine Intelligence **32** (2010), no. 2, 231–241.